CSDL-T-1309

A NOVEL PRECISION VOLTAGE REFERENCE USING A MICROMECHANICAL RESONATOR

by
George N. Schwartz

June 1998

Master of Science Thesis
Massachusetts Institute of Technology

DRAPER
LABORATORY

REPORT DOCUMENTATION PAGE

1. AGENCY USE ONLY *(Leave blank)*	2. REPORT DATE	3. REPORT TYPE AND DATES COVERED
	14.Oct.98	THESIS

4. TITLE AND SUBTITLE
A NOVEL PRECISION VOLTAGE REFERENCE USING A
MICROMECHANICAL RESONATOR

5. FUNDING NUMBERS

6. AUTHOR(S)
2D LT SCHWARTZ GEORGE N

7. PERFORMING ORGANIZATION NAME(S) AND ADDRESS(ES)
MASSACHUSETTS INSTITUTE OF TECHNOLOGY

8. PERFORMING ORGANIZATION REPORT NUMBER

9. SPONSORING/MONITORING AGENCY NAME(S) AND ADDRESS(ES)
THE DEPARTMENT OF THE AIR FORCE
AFIT/CIA, BLDG 125
2950 P STREET
WPAFB OH 45433

10. SPONSORING/MONITORING AGENCY REPORT NUMBER

98-100

11. SUPPLEMENTARY NOTES

12a. DISTRIBUTION AVAILABILITY STATEMENT
Unlimited distribution
In Accordance With AFI 35-205/AFIT Sup 1

12b. DISTRIBUTION CODE

13. ABSTRACT *(Maximum 200 words)*

14. SUBJECT TERMS			15. NUMBER OF PAGES
			16. PRICE CODE

17. SECURITY CLASSIFICATION OF REPORT	18. SECURITY CLASSIFICATION OF THIS PAGE	19. SECURITY CLASSIFICATION OF ABSTRACT	20. LIMITATION OF ABSTRACT

A NOVEL PRECISION VOLTAGE REFERENCE USING A MICROMECHANICAL RESONATOR

by

George N. Schwartz

B.S. Applied Physics
United States Air Force Academy, 1996

SUBMITTED TO THE DEPARTMENT OF ELECTRICAL ENGINEERING AND COMPUTER SCIENCE IN PARTIAL FULFILLMENT OF THE REQUIREMENTS FOR THE DEGREE OF

MASTER OF SCIENCE IN ELECTRICAL ENGINEERING

at the

MASSACHUSETTS INSTITUTE OF TECHNOLOGY

June 1998
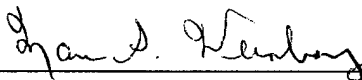
Signature of Author: _____
Department of Electrical Engineering and Computer Science

Approved by: _____
Dr. Marc S. Weinberg
Technical Supervisor, Draper Laboratory

Certified by: _____
Professor J.K. Roberge
Thesis Advisor, MIT

Accepted by: _____
Professor Arthur C. Smith
Chairman, Department Committee on Graduate Students

A NOVEL PRECISION VOLTAGE REFERENCE USING A MICROMECHANICAL RESONATOR

by

George N. Schwartz

Submitted to the Department of Electrical Engineering and Computer Science
on May 8, 1998 in Partial Fulfillment of the
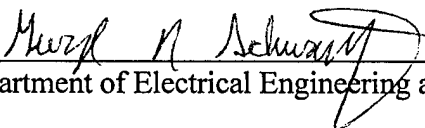Requirements of the Degree of Master of Science in
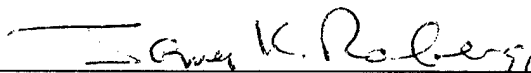Electrical Engineering

ABSTRACT

This thesis describes the analysis and design of a precision voltage reference (PVR) based upon a micromechanical resonator. The precision voltage reference consists of two closed loop controllers and a nonlinear resonator. The oscillator loop maintains oscillations in the resonator. The phase locked loop is a frequency control loop that locks the resonator frequency to an external frequency.

The micromechanical device consists of a pair of resonators that are electrostatically driven and sensed in their out-of-plane vibrational resonance mode. The oscillating proof masses move on flexure beams and the resonator is configured for use as a voltage controlled oscillator within the phase locked loop. The first order stiffness coefficient has an electrostatic component that reduces the frequency of oscillation with increasing bias voltage applied to the resonator. The resonator's frequency sensitivity to voltage is realized by the first order, bias voltage dependent stiffness coefficient. The input bias voltage to the voltage controlled oscillator is the precision voltage reference.

A prototype PVR device was constructed and the PVR operation confirmed. Results between a first order design analysis, advanced modeling, and the prototype are in good agreement. The error model indicates the baseline design for the micromechanical PVR achieves a total voltage stability below 0.4 parts per million (ppm) with temperature control of 0.1°C.

Thesis Supervisor: Professor J.K. Roberge
                      Department of Electrical Engineering
                      Massachusetts Institute of Technology

This thesis was prepared at The Charles Stark Draper Laboratory, Inc., under Contract 15830.

Publication of this thesis does not constitute approval by Draper of the findings or conclusions contained herein. It is published for the exchange and stimulation of ideas.

Permission is hereby granted by the author to the Massachusetts Institute of Technology to reproduce any or all of this thesis.

George N. Schwartz

ACKNOWLEDGMENTS

I would like to thank a number of people who provided assistance with my research at Draper Labs. In general, I received guidance from numerous individuals while completing my thesis and would like to extend my gratitude to all the people at Draper Labs who were willing to help with the project.

First, I would like to thank my technical advisors, Marc Weinberg and Jim Roberge. Marc's advice and extraordinary knowledge of micromechanical dynamics and control design provided an invaluable resource. I would like to thank Professor Roberge for the guidance he offered throughout the project and his careful attention to detail. I thank both of them for providing rapid feedback on problems with the project. Their assistance made the prototype possible.

Thanks are also extended to Jim Campbell, who provided the assistance needed to obtain the sealed resonator units for the PVR and obtain the testing equipment. I managed to destroy five of the six original units and finish my research with a single working device.

A special thanks to Trent Alpers, who built the hardware and spent a great deal of time working out many of the testing problems. We worked through an initial breadboard stage stalled by numerous problems before building the final design. His help was truly immense and I am especially grateful.

I would also like to thank Rich Elliot, Tony Kourepenis, Paul Ward and all the people down in testing. I know how busy all of you were and am grateful for the advice on the design as well as the allocation of testing equipment for the project.
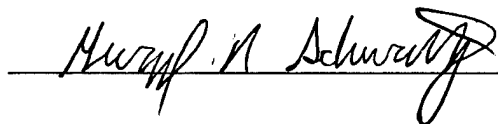
Of course, I would like to thank Erika for her support and patience throughout the thesis. You have always been wonderful and understanding. You were there to help with advice, listen to

problems, and make me take a break when I really needed one. I look forward to all the time we have together.

Finally, I would like to thank my family for their continued support. My parents, Nancy and Keith, continue to be an inspiration and provide a wonderful sense of humor in my life. Charity, Tony, Austin, Taylor, Brian, Melissa, Hilary, and Bill continue to make me laugh and remember what really matters in my life.

TABLE OF CONTENTS

LIST OF FIGURES

9

LIST OF TABLES

INTRODUCTION

1. Objective

The objective of this research is to design, fabricate, and test a Precision Voltage Reference device. The precision voltage is based on the frequency standard of a micromachined resonator. The PVR consists of two closed loop controllers which interface to the plant or micromechanical resonator. The first is a simple oscillator loop, similar to a relay controller, designed to maintain oscillations in the resonator. The second is a phase locked loop (PLL), or frequency control loop, which locks the resonator frequency to a external oscillator. In this loop, the resonator functions as a voltage controlled oscillator (VCO) which signifies that the output frequency is a function of the input bias voltage. The PVR works on the principle that the frequency of the micromechanical resonator is highly stable for various external parameter variations. Given the stability of the oscillator frequency, the bias voltage will also be very stable. This bias voltage is the precision voltage reference that is the objective of this thesis.

1.1 Microelectromechanical Devices

The resonant plant for the PVR is a micromechanical gyroscope configured to operate as a pair of parallel plate oscillators. The field of microelectromechanics (MEMs) is growing at an enormous rate. A study performed by Systems Planning Corporation projects that the market for MEMs devices will expand to $14 billion dollars by the year 2000 from an estimated $700 million in 1990 [13].

Micromechanics is fascinating in part because of the small size achieved in the processing laboratory. Although MEMs does not usually require dimensions as small as those used in integrated circuit processing, it does utilize similar technology. In fact, the two technologies share

many interesting similarities and the development of micromechanical technology parallels some of the developments in silicon processing.

The primary stimulus for the explosion of silicon processing and the integrated circuit was the reduction in cost associated with the transistor. When the technology first emerged, the size reductions made the technology interesting; however, the cost reductions allowed the technology to proliferate. Integrated circuit processing allows batch fabrication where thousands of units are made at a time with no need for individual assembly. Consider that the cost of building a single transistor or a 100 million transistors on a single wafer is the same [13]. The economies of scale achieved in batch processing drove the price per transistor to nearly zero as the size of the individual transistor decreased.

The same advantages that exist in the integrated circuit field apply to MEMs: small size, enormous reductions in cost per device, numerous devices on a single chip with similar performance characteristics, and processing technology that is readily available. Additionally, MEMs offers a number of other unique advantages. The ability to integrate the processing technology for integrated circuits with MEMs processing results in even more cost reductions. A single packaged device would contain the micromachined sensor (transducer) and the electronics needed to process the sensor's signals. A single package reduces noise, parasitics, and failure often associated with the bond pads currently used to interface with the sensor [13]. Finally, elimination of several packages is attractive because the cost of the package is often a significant fraction of the total cost. Micromechanics clearly offers a unique combination of small size and weight with high performance.

The micromechanical device used in the plant of the PVR is a pair of resonators. At the simplest level, the resonator is a typical high quality factor, second order system. The use of a micromechanical device as a resonator is only one of the diverse applications that already exist for micromechanical devices. Among the many other applications are inertial systems, digital displays, automobile safety systems such as airbag deployment, ink jet heads, biomedical instrumentation,

13

chemical analysis, and micro-optics. As the market expands, new applications of the technology will certainly develop.

Historically, the Charles Stark Draper Laboratory contributed to the field of guidance, navigation, and control systems. The Draper micromechanical sensors group has had success in building a tuning fork gyroscope (TFG) and a silicon oscillating accelerometer (SOA). The use of the Draper/Boeing tuning fork gyroscope provides a unique opportunity for quick realization of the PVR. This thesis configures the TFG in order to incorporate it as the PVR resonator. This thesis will also suggest enhancements to the mechanical design that will optimize performance of the PVR. A new mechanical design and fabrication of the PVR-specific resonator is not accomplished here.

1.2 Fabrication of the Draper/Boeing Tuning Fork Gyroscope

The Draper/Boeing TFG structure is shown in the SEM photo in Figure 1.1. The basic structure consists of two proof masses attached to the glass substrate with a folded beam geometry. The outer and inner comb structures are fixed. The TFG also has electrodes under the proof masses. The structures are labeled in Figure 1.2. Draper uses an innovative dissolved wafer process to fabricate its micromechanical instruments with silicon parts on a glass substrate. The dissolved wafer process is a simple, high yield process that uses only three masking steps.
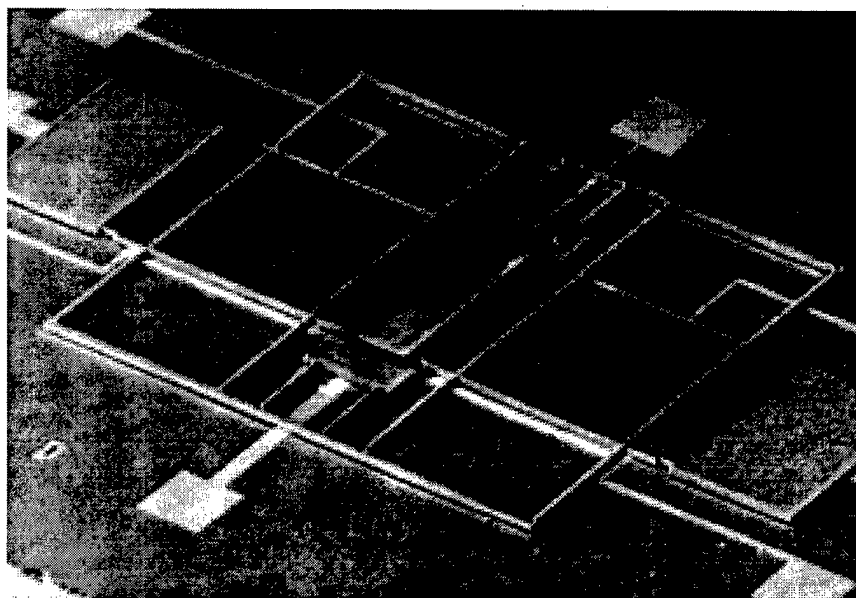
Figure 1.1. SEM of Draper/Boeing Tuning Fork Gyroscope

First, recesses are formed in the silicon to define the gap between the proof mass and the bottom electrode and create the anchors to the glass substrate. This is accomplished by patterning an oxide using conventional photolithography, etching in KOH, and stripping the oxide. Next, the silicon is boron doped to define the proof mass thickness. After the doping, the comb patterns are defined using a photolithography pattern definition and reactive-ion-etching. This completes the silicon process. The glass process begins with the third and final mask for the recess and metal deposition pattern. The wafers are then anodically bonded together. Finally, EDP etching dissolves the undoped silicon structure.

1.3 Motivation for the Micromechanical PVR

Draper Laboratories is well known for the design of precise inertial navigation systems (INS). The lack of a suitable radiation-hard PVR for accelerometer references affected the design of these inertial navigation systems. The creation of a suitable PVR will dramatically alter the accelerometer and system design. Major size and cost reductions will result from such a change. At Draper Laboratories, advances in micromechanical technology resulted in the development of the micromechanical TFG and SOA introduced above. As many of the costly, complex, and bulky

accelerometers and gyroscopes are converted to MEMs technology, a PVR built with this technology will allow simple integration.

The proposed PVR utilizes a micromachined silicon-based tuning fork along with the appropriate closed loop electronics. This configuration offers a unique advantages over semiconductor PVRs: semiconductor PVRs are available with the desired thermal stability; however, they are not radiation-hard. A PVR based on a mechanical resonator should satisfy this requirement. The effect of radiation on silicon mechanical parts is not part of this thesis. Current semiconductor PVRs that require special doping profiles do not promise the low cost and size of a micromechanical PVR.

Finally, the use of a micromechanical silicon tuning fork provides some unique advantages over the traditional quartz tuning forks used in watches, clocks, and computers. The micromechanical resonator achieves a magnitude of 0.5 ppm/°C frequency sensitivity to thermal variations by building the silicon tuning forks on a glass substrate with the dissolved wafer process and proper flexure design. Another advantage of silicon tuning forks is the abundance of companies working with silicon. Finally, the different etching processes for quartz and silicon cause the silicon tuning forks to be smaller (0.3-2 mm) than the quartz (3-5 mm) which allows the silicon to be less expensive. All of the advantages for the micromechanical resonator-based PVR promise to make it an important building block for other micromechanical systems.

1.4 The Precision Voltage Reference

Draper Laboratories manufactures thermally insensitive resonators with micromachined silicon on a glass substrate. The Draper/Boeing tuning fork gyroscope is shown in Figure 1.2 (side view) and in Figure 1.3 (top view). The gyroscope is electrostatically driven along the X-axis (drive axis) while the input angular rate, shown in Figure 1.2, is sensed from the resulting coriolis force along the Y-axis (sense axis). In the tuning fork mode, the two proof masses move out of phase in both the X and Y axes providing an increased scale factor and reducing common mode

errors. A pair of micromechanical resonators exists on both the sense and the drive axes of the TFG.

The PVR uses a single pair of resonators and can be developed using either the sense or the drive axis of the TFG. In the proposed PVR, the sense axis is integrated into a system that creates an inexpensive, interrupt-resistant, precision voltage reference. The PVR utilizes only the Y-axis and the positive direction in y is defined to be upwards in Figure 1.2. The outer drive combs are not used in this extension of the TFG and set to ground potential in order to minimize coupling from the Y-axis to the X-axis. Similarly, the inner comb is placed at ground. The only structures used in the PVR are the vertical parallel plate capacitors formed with the proof mass and the bottom set of electrodes and are outlined with boxes in Figure 1.2.
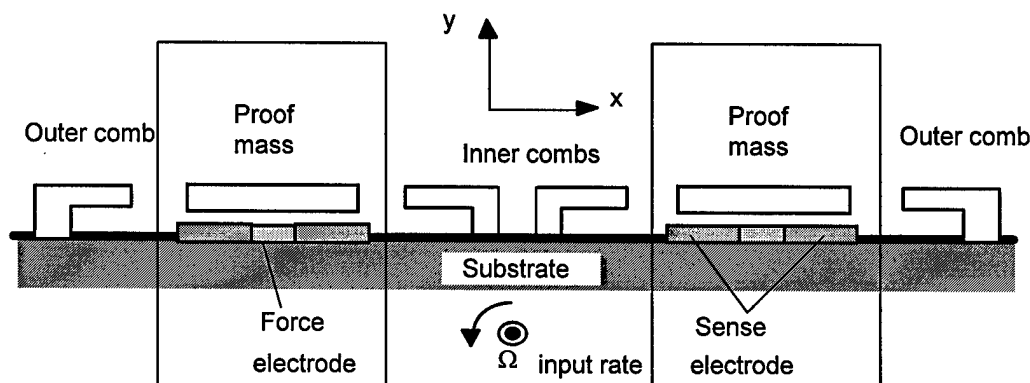
Figure 1.2. End View of Draper/Boeing Tuning Fork Gyroscope

For the PVR, the Y-axis oscillation is excited by electrostatically driving the proof masses out of phase. The forcing and sensing functions are based on the voltages applied to the stationary electrodes and capacitor changes as the proof masses move normal to the bottom electrodes.

17

sense
electrode

drive beam

torsion beam

proof

mass

proof

mass

anchor

fixed comb

base beam
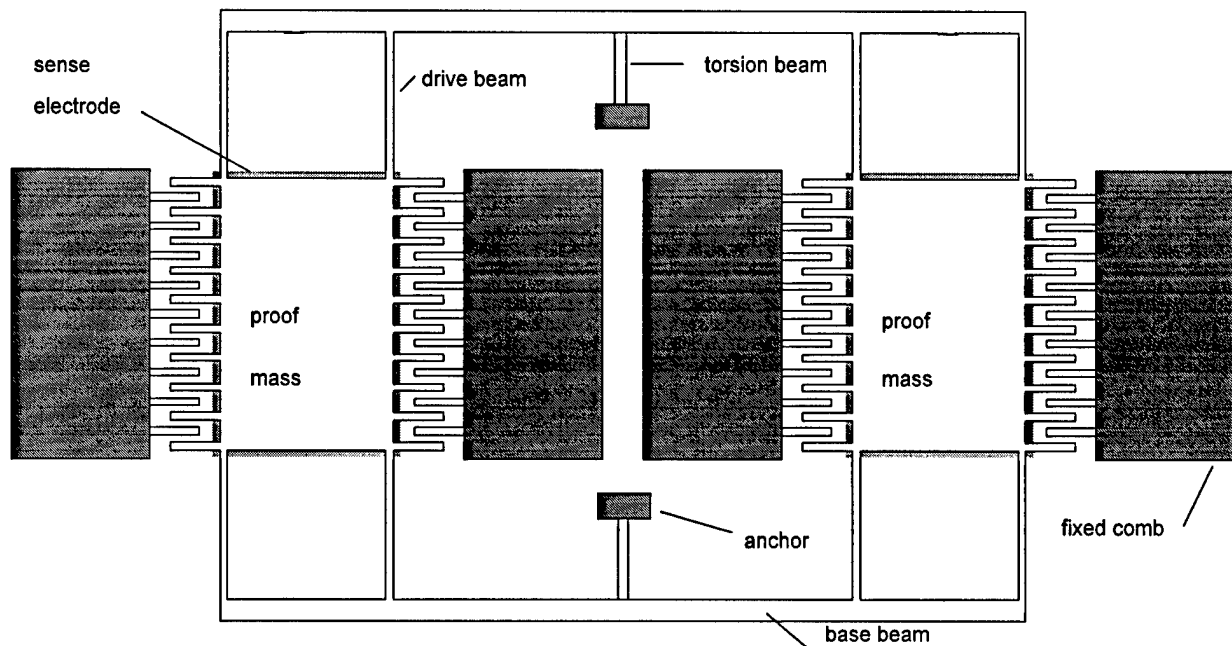
Figure 1.3. Top view of Draper/Boeing Tuning Fork Gyroscope

When a bias voltage is applied to the force and sense electrodes, the force on the proof mass results in a negative spring term proportional to the bias voltage squared. The effect of the bias voltage on the average resonant frequency is shown in Figure 1.4. The average resonant frequency of both proof masses are equal. However, the proof masses are moving out of phase and the resonant frequency of each will deviate slightly from the average frequency. These deviations in frequency are out of phase with respect to one another. The deviations are kept small, on the order of 1e-10, in this application by exciting small amplitude oscillations. The resonant frequency of the resonator decreases as the bias voltage is increased until the electrostatic spring overcomes the mechanical spring and the proof mass snaps down to the bottom electrode. Since the spring term is proportional to the squared voltage, the graph is symmetric around the Y-axis.

The resonator is used as a voltage controlled oscillator where the frequency of the output is dependent on the input bias voltage. The electrostatic characteristic in Figure 1.4 illustrates the highly nonlinear electrostatic characteristic of this micromechanical VCO. The bias voltage on the plates is the PVR voltage and is labeled appropriately in Figure 1.4.

18
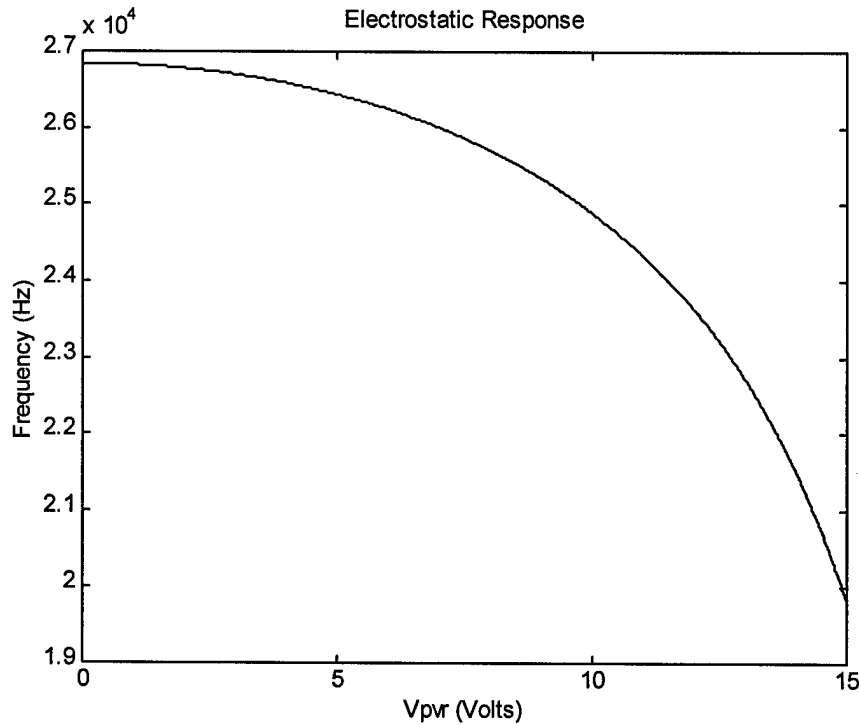
Figure 1.4. Electrostatic Response

Operation at a high bias voltage offers several advantages for the PVR. Most importantly, this increases the resonator voltage stability by reducing the voltage sensitivity to changes in the oscillation frequency. As seen in Figure 1.4, a deviation in resonant frequency results in a smaller change in PVR voltage on the right side of the electrostatic characteristic. The frequency changes resulting from instabilities in external parameters, such as temperature, will have a minimal effect on the voltage stability at high bias voltages. Unfortunately, a high bias voltage means that the possibility of snapdown is increased. Typical operating voltages for the PVR will be around 15 V.

A simplified block diagram of the PVR is shown in Figure 1.5. The outer loop is the phase locked loop which adjusts the bias voltage until the frequency of the resonator and reference frequency are locked. As mentioned, the VCO is the micromechanical resonator. The bias voltage is applied to the sense electrode, shown in Figure 1.2, which alters the eigenfrequency of the resonator. The proof masses are read differentially because they are moving out of phase. The

19

changing capacitance and the bias voltage result in an output voltage that is proportional to the position of the proof masses. The frequency of this signal is locked to a reference and the control voltage at the output of this loop is the precision voltage reference that is applied as the bias voltage to the sense electrode.
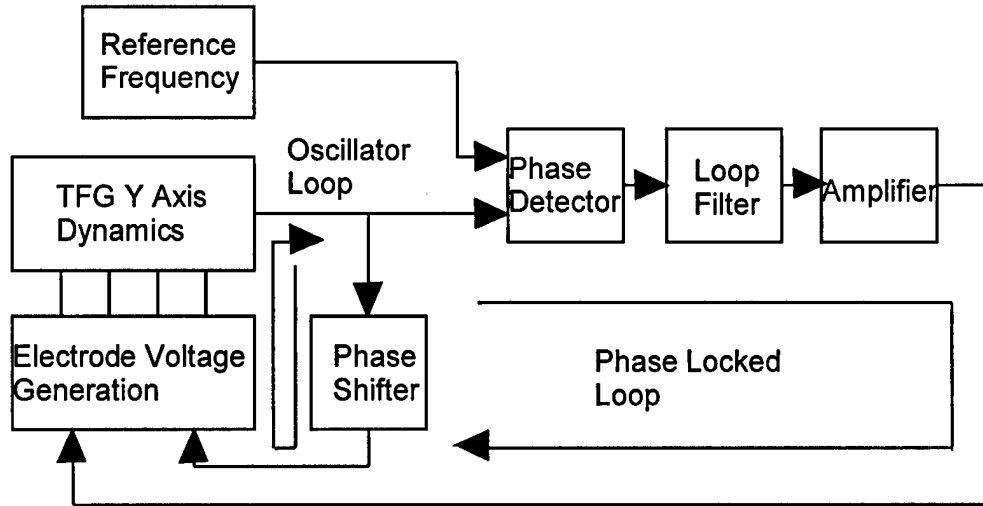
Figure 1.5. Simplified Block Diagram of PVR

The inner loop, or oscillation loop, generates the periodic part of the drive voltage using the output of the VCO. This periodic signal is referred to as the probe voltage. The smaller force electrodes have a voltage that consists of a bias voltage identical to the bias voltage of the sense electrode plus the probe voltage at the eigenfrequency of the resonator. The oscillator loop maintains oscillations in the resonator.

1.5 Overview of Thesis

In the following chapters, the fundamental theory of micromechanical resonators is presented for a single resonator and expanded for the differential pair used in the PVR. The model for the loop dynamics is presented in state space form and the stability of the oscillator loop is examined. The closed loop model simulations are presented and compared with the first order

design calculations. Next, the system requirements are examined and an error model is presented. Finally, the hardware is analyzed with the test results of the PVR device.

1.5.1 Micromechanical Resonator Model

In chapter 2, the fundamental micromechanical resonator model is developed. The two most important concepts for microelectromechanical resonators are mass-spring-damper second order systems, and capacitor electrostatics [8]. The mechanical model of the resonator is presented and the nonlinear effects are examined because of the significant role in the closed loop behavior and frequency stability of the resonator.

The fundamental electrostatic relationships for the resonator are developed. The forcing and sensing models are also presented with a brief preview of the loop electronics used in the sensing model.

1.5.2 Closed Loop Models

In chapter 3, the block diagram is presented and examined in depth. The closed loop models for the oscillator loop and the phase locked loop are developed. The transfer functions of the loop components are presented along with the state space models used for the numerical simulations.

The closed loop stability of the oscillator loop is also examined after linearization of the oscillator loop model. The self excitation (oscillator) loop is linearized using describing functions for the sinusoidal response of a hard limiter and cubic which permits writing a linearized state space model of the resonator. The linearized state space model is used to demonstrate the stability criterion for the oscillation loop which is based entirely on the cubic spring and indicates instability for soft springs above a threshold value.

1.5.3 Baseline Design and Simulation Results

In chapter 4, the first-order design study is presented along with two distinct designs. The baseline design is an optimized design based on changes to the mechanical design of the resonator.

21

The prototype design incorporates the TFG vertical axis resonator. The simulations of the oscillator loop and phase locked loop, which utilize the state space models developed in the previous chapter, are presented. The phase locked loop simulations provide insight into the acquisition and locking behavior of the PLL with a nonlinear VCO. The oscillator loop is used to examine the start-up transient of the resonator. The simulation is also extended to confirm the theoretical oscillator loop stability criterion and quantify the effects of perturbations in the device parameters presented in chapter 5.

1.5.4 *System Requirement and Error Model*

In chapter 5, the implications of the PVR model are examined in detail. The frequency stability, in parts per million (ppm), of the resonator for the desired voltage stability of 0.4 ppm is presented. Following this, the frequency stability of the resonator is examined with regard to perturbations in the amplitude of oscillation, temperature, package pressure, probe voltages, contact potential, feedthrough and radiation. The prototype design is unable to meet the voltage stability requirement of 0.4 ppm without an automatic gain control loop (AGC) while the optimal design satisfies the stability requirement without an AGC.

1.5.5 *Hardware and Test Results*

In chapter 6, the full two proof mass block diagram is presented. The PLL is simplified and linearized to perform a classical control system design. This design is used to determine component level parameter values. The complete PVR component level schematic is presented and limitations in the prototype are examined. Additionally, the test results on the fully functioning prototype are presented.

1.5.6 *Conclusions and Future Work*

Finally, in chapter 7, conclusions for this thesis and recommendations for later work are given. The next major step would be the design and implementation of an amplitude control loop which would enhance performance of the PVR. Additionally, the simulation of a full PVR device,

including both control loops and the resonator dynamics, would be useful to examine the full start-up transient.

MICROMECHANICAL RESONATOR MODEL

2. Overview

The development of the micromechanical resonator model uses many disciplines: dynamics, electrostatics, electronics, fluid dynamics, and many other diverse fields. A micromechanical resonator's dynamics are typically those of a second order mass-spring-damper system. The damping is dependent on the pressure in the container of the enclosed device. The quality factor measured for the parallel plate resonator is consistently around 20,000. In micromechanical devices, capacitive sensors are typically used for detection and comb capacitors are used for forcing because they provide a position independent force. In this application, the capacitive sensor is used for both detection and forcing. The goal of this chapter is to develop a complete model of the resonator, describe how electrostatics are used for forcing and sensing, and explain many of the first order effects of the resonator using simplifications to the complete model.

2.1 Electrostatic Forcing of Micromechanical Resonators

Micromechanical resonators rely heavily on electrostatic forces generated across a capacitor. In this device, the force electrode is used for both forcing and sensing and the sense electrode is used exclusively for sensing the motion. Although using two plates provides some advantages, there are some important limitations when performing both these functions on the same axis. The single axis forcing and sensing couple these mechanisms and the voltages applied to the force plate will affect the sensed motion while the voltage applied to the sense plate will affect the forcing of the resonator. The drive resonators on Draper's TFG was designed to take advantage of the position independent forcing afforded by the comb capacitors and separate axis sensing with the

parallel plate capacitors. The single axis, dual parallel plate resonator extension for the PVR is the most important limitation in the design.

Figure 1.2 shows the two parallel plate capacitors formed from the sense and force electrodes on the bottom and the proof mass on the top. Figure 1.3 shows the top view of the device. In this figure, the motion is perpendicular to the plane of the page. As stated previously, the outer and inner combs are set to ground and not used in this application.

Before proceeding with the analysis of the actual forces on the proof masses, a brief review of some pertinent electrostatics will be presented. The potential energy between two conductors is given by,

$$PE = \frac{1}{2}CV^2 \tag{2.1.1}$$

where,

V = the voltage between the conductors, and

C = the capacitance between the conductors.

The force between the two conductors is the gradient of the potential energy. In this case, the voltages applied to the electrodes are independent of position. The proof mass is at a potential of zero. The electrostatic force on the proof mass (rotor) by the voltage applied to the stationary electrode (stator) is

$$F_e = \nabla PE = \frac{1}{2}\frac{\partial C}{\partial y}V^2 \tag{2.1.2}$$

It is clear from this equation that the vertical force is proportional to the square of the voltage. This has some important implications for choosing the forcing voltage. Most importantly, the square of the voltage must have a component at the fundamental resonant frequency of the oscillator.

Additionally, the partial derivative of the capacitance will be dependent on the geometry of the capacitors. In this application, the parallel plate resonator creates a nonlinearity in the forcing function.

2.1.1 Electrostatic Forcing of the Resonator

The capacitance for two parallel plates with a stationary bottom electrode and dynamic proof mass on top is given by,

$$C = \gamma \frac{\varepsilon_0 A}{Y_0 + y}$$

(2.1.3)

where,

γ = the fringing coefficient,

A = the total plate area,

Y_0 = the nominal gap distance, and

ε_0 = permittivity of free space, and

y = the vertical displacement of the proof mass.

The nominal gap distance is the distance separating the parallel plates with the bottom electrodes and is a function of the bias voltages applied to the bottom electrodes. In terms of strict definitions, the constant displacement from a DC force is contained in the y term; however, it is often useful to group this constant displacement with the Y_0 term and make it a function of the DC voltage applied to the electrodes. The area of the plates, A, becomes important in this problem because the bottom electrode is divided into two separate plates. The outer plate, composing 90% of the electrode's total area is referred to the sense area, A_s. The inner plate which is 10% of the total area is referred to as the force plate, A_f. These two electrodes are shown in Figure 1.2.

26

Finally the electrostatic force on the proof mass, due to the voltages applied to both the sense and force electrodes, is given by,

$$F_e = -\gamma \frac{1}{2} \frac{\varepsilon_0 (A_t V_t^2 + A_s V_s^2)}{(Y_0 + y)^2} \qquad (2.1.4)$$

where,

V_t = force electrode voltage, and

V_s = sense plate voltage.

The capacitance due to the force plate and the sense plate have been treated as if they were in parallel. The single fringing coefficient is used for the total capacitance.

The forcing function is highly nonlinear with respect to position. In an ideal situation, the proof mass oscillation amplitude will be small compared to the nominal gap distance. A small amplitude model will be developed along with a large amplitude model in Equation 2.1.4 in order to accommodate both cases. The small amplitude model makes it simpler to examine many features of the oscillator and permits a linear state space representation of the resonator.

The effects of the nonlinear forcing function are evident if the electrostatic force is expanded using a Taylor series approximation. If the oscillations are small, $y/Y_0 \ll 1$, and the electrostatic force becomes,

$$F_e = -\gamma \frac{\varepsilon_0 (A_t V_t^2 + A_s V_s^2)}{2Y_0^2} \left[1 - 2\frac{y}{Y_0} + 3\left(\frac{y}{Y_0}\right)^2 - 4\left(\frac{y}{Y_0}\right)^3 + \dots \right] \qquad (2.1.5)$$

The electrostatic force now contains position dependent terms which can be written as electrical spring terms. There is also a position-independent force term. The electrical spring stiffness values and vertical force terms are given by,

27

$$k_{ye} = -\gamma \frac{\varepsilon_0 (A_t V_t^2 + A_s V_s^2)}{Y_0^3} \qquad k_{y2e} = \gamma \frac{3}{2} \frac{\varepsilon_0 (A_t V_t^2 + A_s V_s^2)}{Y_0^4} \qquad (2.1.6)$$

$$k_{y3e} = -\gamma \frac{2\varepsilon_0 (A_t V_t^2 + A_s V_s^2)}{Y_0^5} \qquad F_y = -\gamma \frac{1}{2} \frac{\varepsilon_0 (A_t V_t^2 + A_s V_s^2)}{Y_0^2} \qquad (2.1.7)$$

This completes the modeling of the electrostatic force. Equation 2.1.4 will be used for large amplitudes while Equation 2.1.5 will be used for small amplitude oscillations of the resonator.

2.1.2 Electrode Voltages

As stated earlier, the choice of the drive voltages is paramount to constructing an effective device. The primary limitation is single axis sensing and forcing. In order to force the oscillator, a periodic component is required, while sensing requires a constant voltage. In this case, the voltages applied to the sense and force plates are given by,

$$\begin{aligned} V_{1t} &= V_a + V_b csq(\omega t) & V_{1s} &= V_c \\ V_{2t} &= -V_a + V_b csq(\omega t) & V_{2s} &= -V_c \end{aligned} \qquad (2.1.5)$$

where,

$csq(\omega t)$ = a square wave in phase with cosine at the frequency ω, and

$V_a = V_c = V_{pvr}$ the precision voltage reference or bias voltage, and

V_b = the probe voltage.

The notation for the bias voltages is used to provide a general model that allows separate definition of these voltages. The negative signs associated with the DC voltages result in forcing the two parallel plates out of phase. Additionally, they allow the position of both proof masses to be read differentially, increasing the scale factor at the output. The choice for the drive voltages here is dictated by simplicity and ease of implementation. It does not offer an elegant solution to feedthrough. Feedthrough describes the current from the electrode to the proof mass caused by

28

high frequency voltage and a constant steady state capacitance. The feedthrough signal is in quadrature to the sensed signal and results in errors in the position sensing.

The biasing is accomplished in a number of ways. The sense bias voltage, V_c, can be applied to the sense plate and a signal from among the following can be applied to the much smaller force plate, force bias plus a drive voltage at the eigenfrequency, at half resonance, or at two dual frequencies. These last two options are designed specifically to eliminate the effects of feedthrough by placing the voltage off resonance and allowing the oscillator to attenuate the feedthrough term. The squared voltage still produces a force at the resonance of the oscillator. The half-frequency drive does offer some unique advantages such as higher drive voltages and elimination of the feedthrough. The first option, drive voltage at the eigenfrequency, is used in the PVR. The force bias is identical to the sense bias and is defined as the precision voltage reference.

2.2 Lumped Parameter Model and Non-dimensionalization

The basic dynamic model for a single element (single proof mass) micromechanical resonator with two degrees of freedom is a coupled pair of second-order, nonlinear, differential equations [8]. This includes one equation for each degree of freedom. The model for the PVR uses a single degree of freedom, corresponding to the Y axis, as shown in Figure 1.2. Furthermore, the PVR utilizes two coupled proof masses. The out-of-phase mode is the only mode excited of the two normal modes of the resonator system. In out-of-phase forcing the coupling stiffness drops out of the equations of motion. Therefore, the lumped model equations are written in terms of one proof mass. The full set of equations are only written where necessary for clarity.

The equations for a single mass 1-D lumped parameter model can be derived using Lagrange's equations using a single generalized coordinate [8]. The following equation for the vertical displacement of a single proof mass results from writing the total potential energy of the system in terms of linear, quadratic, and cubic mechanical springs.

$$m\ddot{y} + b_y \dot{y} + k_{ym}y + k_{y2m}y^2 + k_{y3m}y^3 = F_e \qquad (2.2.1)$$

29

where,

m = mass of the proof mass, and

b_y = the damping coefficient, and

F_e = the electrostatic force on the proof mass

$k_{ym} \ k_{y2m} \ k_{y3y}$ = the linear, quadratic, and cubic mechanical stiffness

The lumped parameter model produces three mechanical spring terms. The subscripts on the spring constants indicate that these are along the y axis, the order of the constant, and that each one is a mechanical spring term. As shown previously, the nonlinearity in the electrostatic forcing function, F_e, results in electrical spring terms with linear, quadratic, and cubic stiffness coefficients.

The higher order mechanical spring terms are now discarded. The drive axis of the TFG has a position independent forcing function and contains no electrostatic spring terms. The testing results on this axis indicate that the quadratic and cubic electrical spring terms will dominate the higher order mechanical spring terms [17]. The linear mechanical spring term is maintained in the model. Equation 2.2.1 can be rewritten,

$$m\ddot{y} + b_y \dot{y} + k_{ym} y = F_e \qquad (2.2.2)$$

which is a classic mass-spring-damper system as shown in Figure 2.1. However, this model does possess the nonlinearity contained within the forcing function.
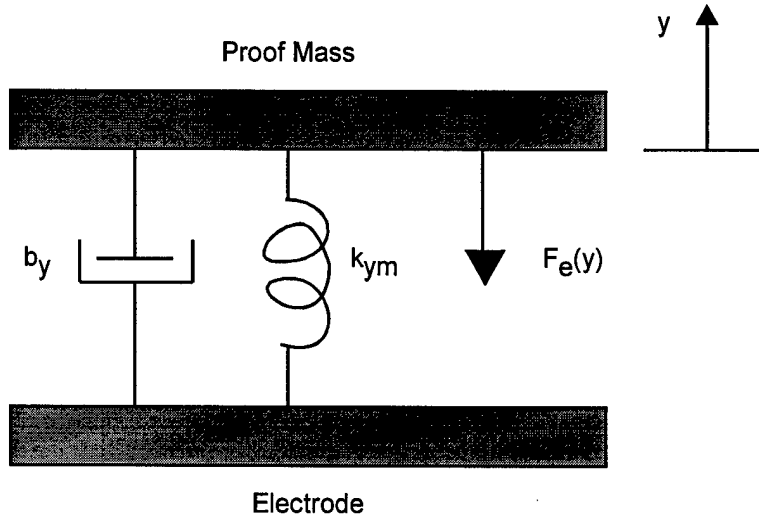
Figure 2.1. Typical Mass Spring Damper System

The coupled model is presented in Figure 2.2 where the model only contains the elastic restoring forces. This model validates throwing out the coupling term for the out-of-phase mode. The equations of motion are written assuming that a finite mass m_3 exists at the coupling point. This can be set to zero later.

$$m_1 \ddot{y}_1 = k_{ym1}(y_1 - y_3)$$
$$m_2 \ddot{y}_2 = k_{ym2}(y_2 - y_3) \qquad (2.2.2a)$$
$$m_3 \ddot{y}_1 = k_{ym3}y_3 - k_{ym1}(y_1 - y_3) - k_{ym2}(y_2 - y_3)$$

In a the symmetrical resonator, the first two stiffness terms are equal. The out-of-phase mode if described by the normal coordinate x_1-x_2. A single differential equation is obtained by subtracting the second equation from the first.

$$m_1\left(\ddot{y}_1 - \ddot{y}_2\right) = k_{ym}\left(y_1 - y_2\right) \qquad (2.2.2.b)$$

31

The coupling is eliminated if the common mode is not excited. The coupling stiffness term is discarded from the equations of motion and Equation 2.2.2 is used.
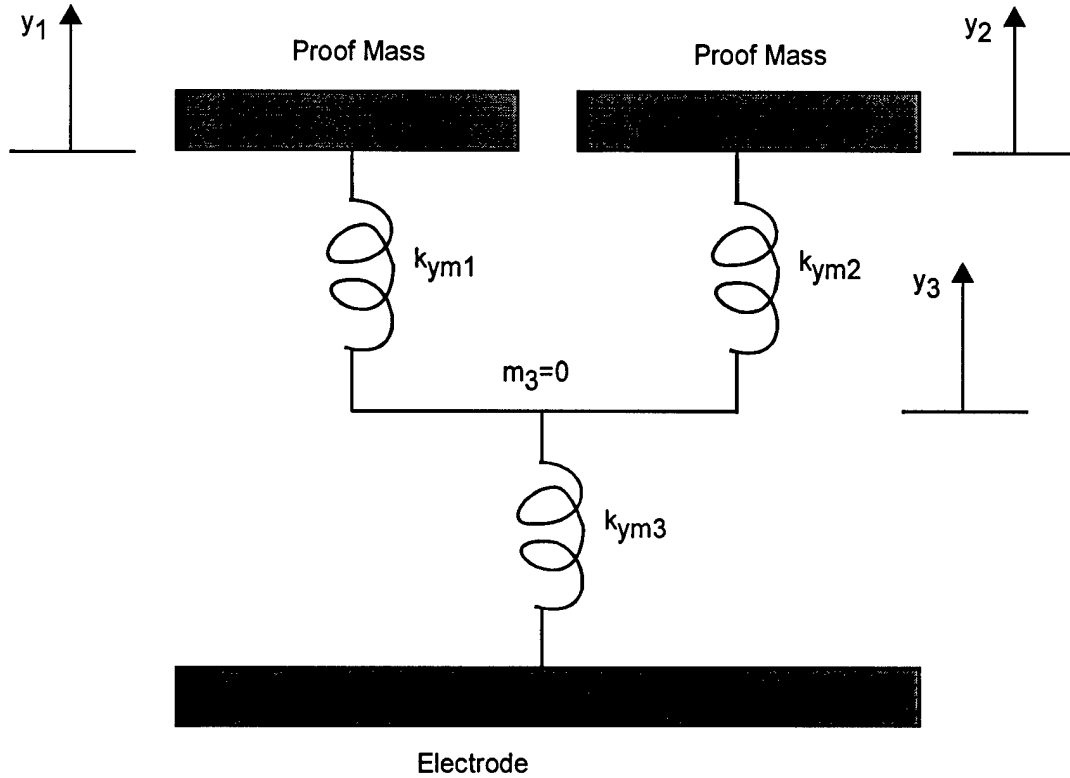
Figure 2.2. Coupled Proof Mass Model

The development of the small amplitude model is the simplest way to proceed. Equation 2.1.5 is substituted in Equation 2.2.2 and Equation 2.1.6 is used to write the stiffness coefficients. This produces the following equation.

$$m\ddot{y} + b_y \dot{y} + k_y y + k_{y2e} y^2 + k_{y3e} y^3 = F_y \qquad (2.2.3)$$

where,

$k_y = k_{ym} + k_{ye}$ net linear stiffness, and

F_y = position-independent vertical force on the proof mass.

Equation 2.2.3 is useful to obtain nondimensionalization coefficients. Nondimensionalizing the equations makes many of the following graphs easier to interpret and the equations universal to similar resonator systems. Finally, this makes the numerical analysis more accurate with step sizes and displacements close to unity. The nondimensional time and displacement is given by,

$$\tau = \omega_n t = \sqrt{\frac{k_y}{m}} t \qquad (2.2.4)$$

$$\tilde{y} = \frac{y}{y_0} \qquad (2.2.5)$$

where,

ω_n is the nominal natural frequency of the y-axis, and

y_0 is the nominal steady state oscillation amplitude.

Both of these nominal terms are artificial constructs. They are first order, linear estimations of the values which provide an approximate order of magnitude for nondimensionalization of the full differential equations.

Both of the approximations are considered accurate under most operating conditions. The linear stiffness in Equation 2.2.5 contains both the linear mechanical and electrical stiffness. The nominal oscillation frequency written in Equation 2.2.5 is only an approximation assuming small damping and no nonlinear spring terms. The quality factor of the vertical axis is exceptionally high making the damping very small and the first assumption valid. The nonlinearity imposed by the cubic electrical spring term, examined in section 2.3.2, is found to produce a small shift of the frequency of oscillation.

33

Substituting the nondimensional temporal and spatial relationships into Equation 2.2.3 and using Equation 2.1.7 for the electrostatic force, the following equation results after some rearranging.

$$\ddot{\tilde{y}} + \frac{1}{Q}\dot{\tilde{y}} + \tilde{y} + \tilde{k}_{y2}\tilde{y}^2 + \tilde{k}_{y3}\tilde{y}^3 = \tilde{F}_y \qquad (2.2.6)$$

where,

$$\tilde{k}_{y2} = \frac{k_{y2}y_0}{k_y} \qquad \tilde{k}_{y3} = \frac{k_{y3}y_0^2}{k_y} \qquad \tilde{F}_y = \frac{F_y}{k_y y_0} \qquad (2.2.7)$$

This simplification to the nondimensionalized full model derived in Equation 2.2.3 provides the means to conveniently examine two important parallel plate resonator effects: snapdown and spring softening.

Before these two topics are addressed, the large amplitude model is nondimensionalized. Substituting the nondimensional parameters into Equation 2.2.2, the following equation results.

$$\ddot{\tilde{y}} + \frac{1}{Q}\dot{\tilde{y}} + \frac{k_{ym}}{k_y}\tilde{y} = -\frac{1}{2}\gamma\varepsilon_0 \frac{(A_t V_t^2 + A_s V_s^2)}{(Y_0 + y_0\tilde{y})^2}\frac{1}{k_y y_0} \qquad (2.2.8)$$

where,

$$Q = \frac{m\omega_n}{b_y} = \text{Quality factor of the resonator} \qquad . \qquad (2.2.9)$$

Equation 2.2.8 describes the motion of a single proof mass under the electrostatic forces caused by the voltages on both the force and sense plates. It is used when the amplitude is large in comparison to the nominal gap distance. Equation 2.2.6 is used for small amplitude operation. Both equations are in the form of a general second order system; however, the electrostatic stiffness

34

coefficients have some interesting effects on the dynamics. Two important effects are snapdown and spring softening associated with the cubic nonlinearity.

2.2.1 Snapdown

The linear electrostatic spring is given by,

$$k_y = [k_{ym} - \gamma \frac{\varepsilon_0 (A_t V_t^2 + A_s V_s^2)}{Y_0^3}] \qquad (2.2.9)$$

This spring term is the defining equation for the electrostatic characteristic shown in Figure 1.4 that illustrates the transfer characteristic for the VCO. The first order electrostatic spring term gives the sense axis some interesting dynamics. The average frequency of the resonator proof masses can be approximated by discarding the time dependent terms in Equation 2.2.9. The bias voltages for the force and sense plates are equal (V_{pvr}), and these terms dominate any time dependent component of the squared voltages in Equation 2.2.9. The linear stiffness becomes,

$$k_y = [k_{ym} - \gamma \frac{\varepsilon_0 A V_{pvr}^2}{Y_0^3}] \qquad (2.2.10)$$

Using typical parameters for the resonators, this analytical model is presented along with the experimental data in Figure 2.3. The experimental plot closely approximates the predicted behavior. Although the system resembles a simple quadratic as in Equation 2.2.10, the magnitude of Y_0 decreases as the voltage is increased, causing the electrostatic characteristic to bend more sharply.

35
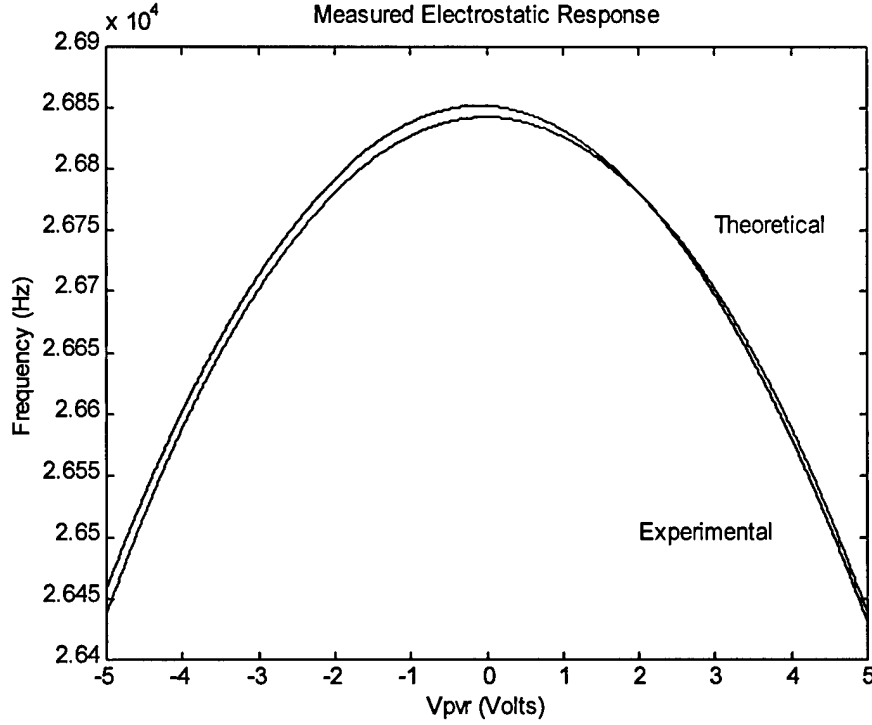
Figure 2.3. Theoretical and Measured Electrostatic Characteristic

As the bias voltage is increased, the linear electrostatic spring will eventually overcome the mechanical one and the proof mass will snap down to contact the electrode. As the bias voltage is increased, the expansion in Equation 2.1.5 for the electrostatic force will not be valid. Therefore, the full equation for the net stiffness is used. For the following estimates of the snapdown voltage, a steady state condition is assumed where the position of the proof mass is static. The net stiffness is then given by,

$$k_n = -\frac{\partial \sum F}{\partial y} = k_{ym} - \frac{\gamma \varepsilon_0 (A_t V_t^2 + A_s V_s^2)}{(Y_0 + y)^3} \qquad (2.2.11)$$

The snapdown voltage occurs when the electrostatic stiffness equals the mechanical stiffness or simply when the net stiffness approaches zero. Setting the net stiffness to zero produces the following estimate for the snapdown voltage.

36

$$V_{snap} = \sqrt{\frac{k_{ym}(Y_0 + y)^3}{\gamma \varepsilon_0 A}} \qquad (2.2.12)$$

As snapdown occurs, the net force will also approach zero. Equating the electrostatic force in Equation 2.1.5 and the force due to the linear mechanical stiffness, and substituting the expression for k_{ym} from Equation 2.2.11 gives the necessary displacement for snapdown to occur at

$$y = -\frac{Y_0}{3} \qquad (2.2.13)$$

This means that once the gap decreases by a third due to the DC forces , the proof mass will snap down to contact the bottom electrodes. Substituting this value into the estimate for the snapdown voltage.

$$V_{snap} = \sqrt{\frac{k_{ym}(\frac{2}{3}Y_0)^3}{\gamma \varepsilon_0 A}} \qquad (2.2.14)$$

The electrostatic characteristic can be extended to the snapdown voltage as shown in Figure 2.4. Typical values for the snapdown voltage are 17 V.
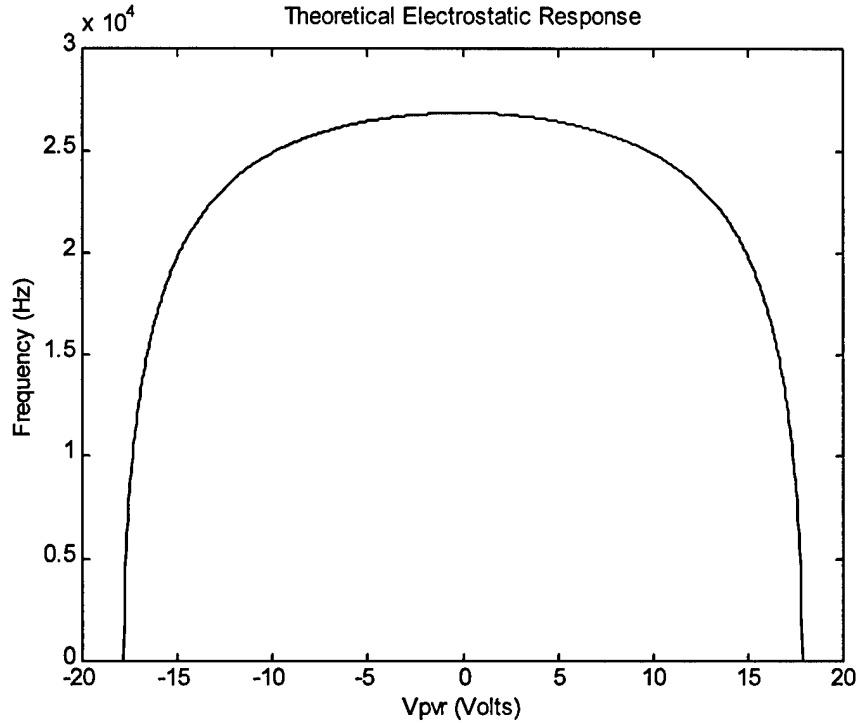
Figure 2.4. Snapdown Voltage in Electrostatic Response

Operation of the resonator pair near the snapdown voltage poses a potential problem for the device. When the proof mass snaps down to contact the bottom electrode, it may stick and prevent further operation of the resonator.

2.2.2 Electrostatic Spring Softening and the Duffing Equation

The third order spring term also has some significant effects on the dynamics of the proof mass. It is useful to examine the full equation of motion in 2.2.6. In this analysis, it is assumed that the resonator is driven open loop and thus the forcing function is independent of the output. The equation is classified as a second order nonlinear, damped, forced differential equation. It is also nonstationary because the frequency of the forcing function is changing in time and in closed loop operation, the amplitude will also be initially changing in time. Finally, it is parametrically excited

38

because the stiffness coefficients are functions of time and the forcing function is multi-valued in frequency. A number of important simplifications will be made to assist in solving this equation.

First, the second order spring term will be dropped completely. Ideally, the effects of the second order spring term from both proof masses are canceled due to the operation of the two plates out of phase and the differential position pick-off. The time dependence in the stiffness coefficients is small (1e-10) so these terms will be considered time independent. Finally, the forcing function is considered single-valued; all subharmonic and superharmonic terms will produce a small output because of the exceptionally high Q of the device. The result of these simplifications is the classic Duffing Equation.

The general Duffing equation can be solved using a variety perturbation methods. These methods lend themselves to the solutions of nonstationary systems when the amplitude and frequency are changing slowly in time [10]. Lindstedt's method is used here and produces identical results of the describing functions used in the linearized state space model [8,10].

The general nondimensionalized, damped, forced Duffing equation can be written, using Equation 2.2.6,

$$\ddot{y} + \delta \dot{y} + y + \lambda y^3 = \kappa \cos(\omega t) \tag{2.2.15}$$

where the vertical force in Equation 2.2.6 has been approximated with the time dependent part, using the forcing voltages given in Equation 2.1.5 and substituting these into the vertical force expression in Equation 2.1.7. The DC force causes a constant displacement absorbed in the nominal gap distance, Y_0. The correspondence between the device parameters and the general Duffing equation can be written by comparing Equation 2.2.6 with Equation 2.2.15.

$$\lambda = \tilde{k}_{y3} \qquad \delta = \frac{1}{Q} \qquad \kappa = -\frac{1}{2} \frac{\gamma \varepsilon_0 A_t V_a V_b}{Y_0^2} \frac{1}{k_y y_0} \tag{2.2.16}$$

First, the parameters are defined as a function of e, so that as e goes to zero, the system reduces to an unforced, undamped, linear oscillator. This sets up the problem as a perturbation applied to a highly damped, weakly nonlinear equation with small input forces.

$$
\begin{aligned}
y &= y_0 + \varepsilon y_1 \\
\omega &= \omega_0 + \varepsilon \omega_1 \\
\lambda &= \varepsilon \lambda_1 \\
\delta &= \varepsilon \delta_1 \\
\kappa &= \varepsilon \kappa_1
\end{aligned}
\tag{2.2.17}
$$

where $\omega_0 = 1$ according to the nondimensionalization and unfortunately the y_0 is unrelated to the normalization factor introduced in 2.2.5 Substituting these expressions into Equation 2.2.16, defining $\tau = \omega(\varepsilon)t$, and equating the ε_0 and ε_1 coefficients,

$$
\begin{aligned}
\ddot{y}_0 + y_0 &= 0 \\
\ddot{y}_1 + y_1 &= -2\omega_1 \ddot{y}_0 - \delta_1 \dot{y}_0 - \lambda_1 y_0^3 + \kappa_1 \cos(\tau)
\end{aligned}
\tag{2.2.18}
$$

These two equations are solved sequentially. The solution to the first is given by,

$$
y_0 = \tilde{A}\cos(\tau - \phi)
\tag{2.2.19}
$$

Substituting this solution into the second equation and using several trigonometric identities, leads to the differential equation for x_1,

$$
\ddot{y}_1 + y_1 = \left[-2\omega_1 \tilde{A} - \frac{3}{4}\lambda_1 \tilde{A}^3 + \kappa_1 \cos(\phi) \right]\cos(\tau - \phi) +
$$
$$
\left[\delta_1 \tilde{A} - \kappa_1 \sin(\phi) \right]\sin(\tau - \phi) - \frac{1}{4}\lambda_1 \tilde{A}^3 \cos(3(\tau - \phi))
\tag{2.2.20}
$$

Now, the secular terms are eliminated by setting the terms in brackets to zero. This insures the expansion is periodic. The solutions to the resulting two equations produce the amplitude and

40

phase dependence in terms of frequency in Equation 2.2.19. The frequency response equation for Duffing's equation is given by,

$$\omega = 1 - \frac{3}{8}\lambda\tilde{A}^2 \pm \sqrt{\frac{\kappa^2}{4\tilde{A}^2} - \frac{\delta^2}{4}}$$

(2.2.21)

and the phase characteristic can be written,

$$\phi = \pm\tan^{-1}\left(\frac{\delta}{\sqrt{\frac{\kappa^2}{\tilde{A}^2} - \delta^2}}\right)$$

(2.2.22)

where,

$$\tilde{A} = A/A_p = \text{the normalized amplitude}$$

The locus of points described by the frequency and phase equations represent the singular points for the system.

The phase characteristic offers a convenient way to solve for the peak oscillation amplitude which can be used for the normalization factor in Equation 2.2.6. At resonance, the phase will be at -90° for a second order system and the normalized amplitude will equal unity. The normalized amplitude is given by $\tilde{A} = \kappa/\delta$. Solving for the real amplitude which corresponds to the normalization factor and putting the expression in terms of the y axis parameters, the peak amplitude of the displacement is given by,

$$A_p = -\frac{\gamma\varepsilon_0 A_t V_a V_b}{Y_0^2}\frac{1}{k_y}\frac{m\omega_n}{b_y}$$

(2.2.19)

For proper normalization, this is used throughout the simulations for y_0. Analogous to the temporal normalization, this is an estimate derived from Lindstedt's technique. The phase and frequency response equations are plotted in Figures 2.4-2.7 for a variety of parameters listed in Table 2.1.

In Figure 2.5 and Figure 2.6, the cubic spring term λ is set to an arbitrary negative (spring softening) and positive (spring hardening) term demonstrating the effects of spring softening and hardening. The other parameters match the dynamic parameters of the resonator with V_{pvr} =15 V and V_b = 1 mV. The magnitude response of the soft spring bends to the left while that of the hard spring bends to the right. The response for a linear spring is also shown and matches the expected result for a general second order system. The low damping of the system is evident in the very narrow peak and large slope in the phase characteristic.

In Figure 2.7 and Figure 2.8, the value of the cubic spring coefficient for resonators is substituted to demonstrate that the cubic spring term effects are small but indeed exist. The bias and drive voltages are V_{pvr} =15 V and V_b = 1 mV. All of the parameters used in Figures 2.4-2.7 listed below in Table 2.1.

Table 2.1. Non-dimensional Parameters for the Duffing Equation Simulation

	Linear	Soft	Hard	Resonator
λ	0	-0.01	0.01	-5.9e-4
δ	5.91e-5	5.91e-5	5.91e-5	5.91e-5
κ	-5.91e-5	-5.91e-5	-5.91e-5	-5.91e-5

The change in resonant frequency due to the cubic term is only 0.02% of the nominal value at the operating conditions simulated in Figure 2.7. This confirms the weak nonlinearity of the system assumed in the perturbation analysis.
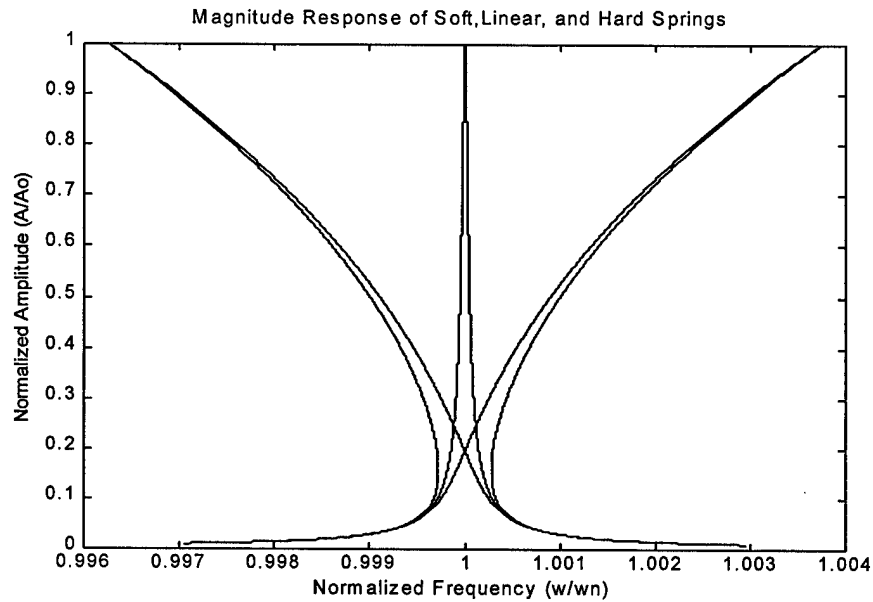
Figure 2.5. Magnitude Response of Three Spring Types
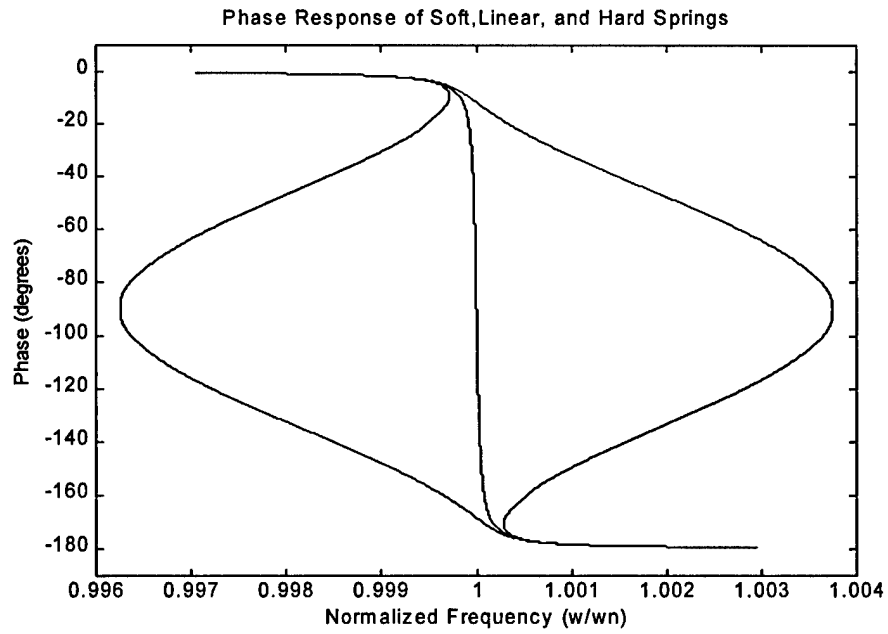
Figure 2.6. Phase Response of Three Spring Types
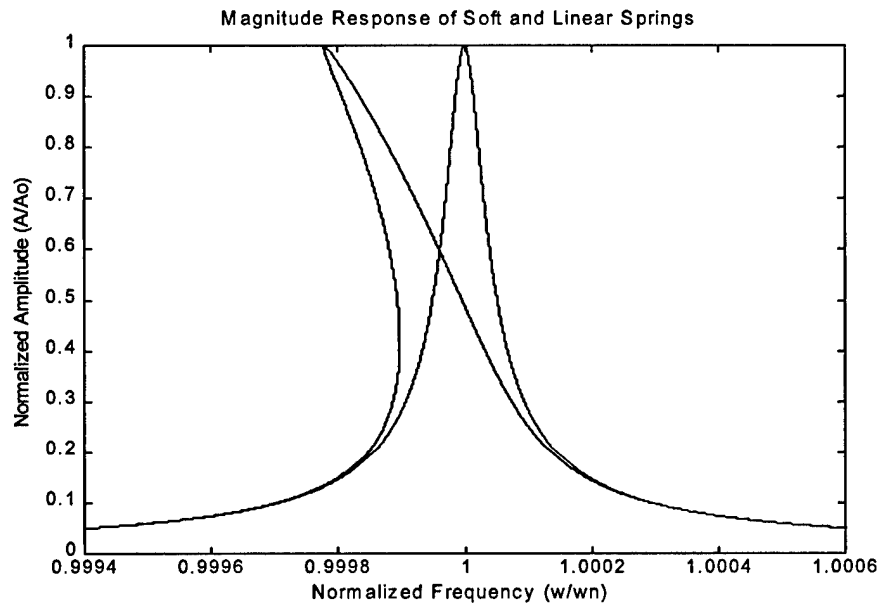
Figure 2.7. Amplitude Response of Parallel Plate Resonator

44

Phase Response of Soft and Linear Springs
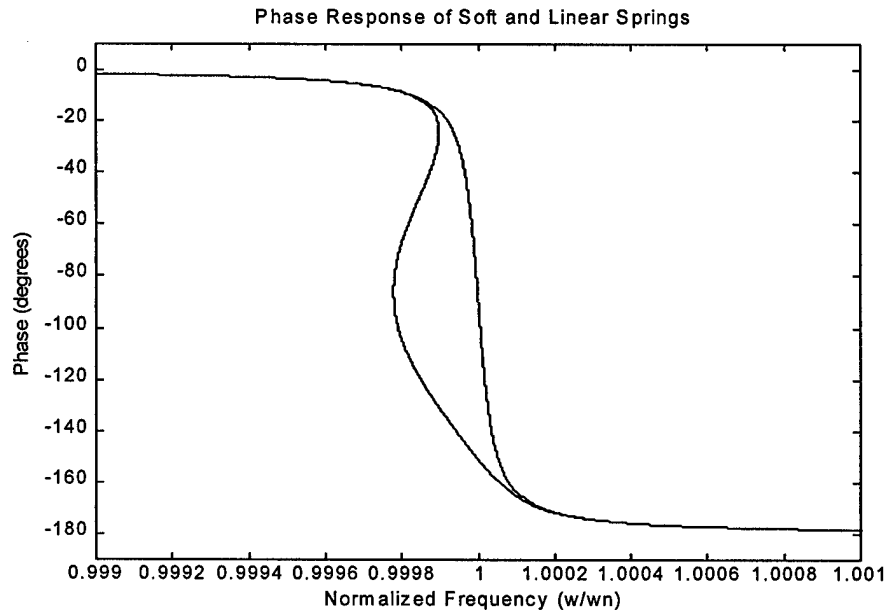
Figure 2.8. Phase Response of Parallel Plate Resonator

When the oscillator is driven open loop, it will be driven at a specified input frequency. This frequency along with the initial conditions will determine the amplitude and phase of the oscillations. The stability of the steady state points(i.e. singular) can be determined with a phase plane plot.

When the loop is closed, the forcing function becomes a signal proportional to the velocity of the proof mass. Similar to other self-excited systems, the oscillator will settle onto a limit cycle, assuming that it exists. This is examined in detail in the following chapter. Since the phase characteristic is monotonic, there can be only one position where the phase matches what is needed to close the loop. In this case, the device will be operating at 90°.

2.3 Output Sensing

In order to properly bridge the gap between the micromechanical motion of the oscillator and a block diagram description of the device, the sensing of the motion must be examined. The

sensing of motion in micromechanical devices is done in a similar way to the electrostatic forcing. In this respect, using the unique properties of the capacitor is fundamental to designing the detector.

The proof mass motion is measured by connected both of the moving proof masses, to an integrator as shown in Figure 2.9, where the force and sense plates for each proof mass have been separated and depicted as capacitors in parallel. This setup is essentially a charge amplifier and the operation is best understood in the simplest form. In the ideal situation, a constant voltage is applied to the sense plate beneath the proof mass. The oscillations of the proof mass and the subsequent variable capacitance cause a sinusoidal varying charge to be injected into the operational amplifier input. This is finally integrated to produce a signal proportional to the proof mass position.

The preamplifier is shown in Figure 2.9. The motion of the second proof mass is out of phase with the first and designated with the variable capacitance in the opposite direction. The voltages and corresponding capacitance are labeled according to proof mass and electrode type(force or sense). The pre-amp is a low pass filter with a pole frequency much less than the eigenfrequency of the resonator. The contact potential voltage is modeled with the common voltage source across the four capacitors. The noise is modeled with the voltage source at the negative input terminal to the op-amp and the stray capacitance is modeled at the positive terminal. The noise at the pre-amp is the dominant noise in the closed loop.
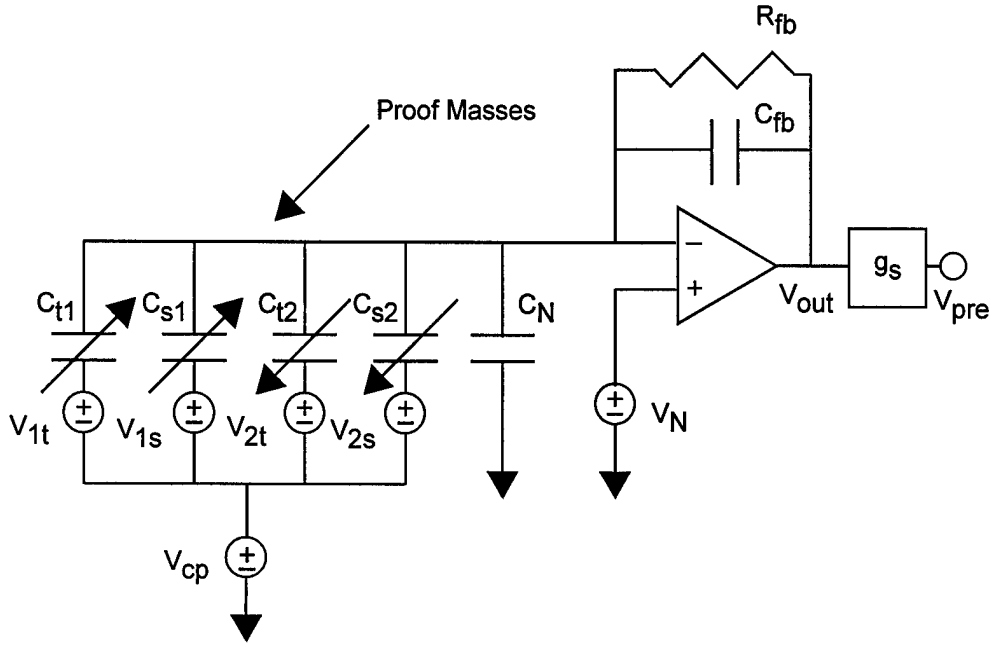
Figure 2.9. Complete Preamplifier Model

Writing Kirchhoff's current law at the negative input terminal of the op-amp gives the following equation,

$$-s(V_N - V_{1s})C_{1s} - s(V_N - V_{1t})C_{1t} - s(V_N - V_{2s})C_{2s} -$$

$$s(V_N - V_{2t})C_{2t} - sV_N C_N = C_{fb}(s + \frac{1}{R_{fb}C_{fb}})(V_N - V_{out}) \qquad (2.4.1)$$

where,

V_{cp} = the voltage due to the contact potential between the silicon structure and gold alloy anchors.

Substituting the following expression for the state variable

$$x^* = V_{out} - V_N(1 + \frac{C_N}{C_{fb}}) \qquad (2.4.2)$$

47

Equation 2.4.1 can now be rewritten,

$$\dot{x^*} = -\omega_{fb}(x^* + V_N \frac{C_N}{C_{fb}}) +$$

$$\frac{1}{C_{fb}}[s(V_N - V_{1s})C_{1s} + s(V_N - V_{1t})C_{1t}] +$$ (2.4.3)

$$\frac{1}{C_{fb}}[s(V_N - V_{2s})C_{2s} + s(V_N - V_{2t})C_{2t}]$$

Simplifying this expression is difficult due to the time dependence of both V_{1t} and V_{2t}, and C_{1t} and C_{2t} in the last two quantities. However, a simpler form is derived by taking the derivative of the four terms. Now, a nonlinear state evolution equation in terms of y_1, y_2, and x^* is achieved. This equation can also be nondimensionalized as before.

$$\dot{x^*} = -\tilde{\omega}_{fb}(x^* + V_N \frac{C_N}{C_{fb}}) - \dot{V}_{1t}\frac{C_{1t}}{C_{fb}} - \dot{V}_{2t}\frac{C_{2t}}{C_{fb}} +$$

$$\frac{y_0}{C_{fb}}[(V_N - V_{s1})\frac{\partial C_{1s}}{\partial y_1} + (V_N - V_{1t})\frac{\partial C_{1t}}{\partial y_1}]\dot{\tilde{y}}_1 +$$ (2.4.4)

$$\frac{y_0}{C_{fb}}[(V_N - V_{2s})\frac{\partial C_{2s}}{\partial y_2} + (V_N - V_{2t})\frac{\partial C_{2t}}{\partial y_2}]\dot{\tilde{y}}_2$$

where,

$\omega_{fb} = \omega_{fb}/\omega_n$ = the normalized pole frequency for the charge amplifier

Finally, the transfer function from V_{out} to V_{pre} must be determined in terms of the designated state variables. The component between these two points includes a high pass filter , eliminating any unwanted DC components of the output, and provides a high frequency gain of R_g/R_b. The transfer function is given in nondimensional units by,

$$V_{pre} = -\frac{R_g}{R_b}\frac{\tilde{s}}{\tilde{s} + \tilde{w}_b}V_{out}$$ (2.4.5)

where,

$\tilde{w}_b$ = the normalized pole frequency of the high-pass filter

This can be simplified by recognizing that the $\tilde{w}_b \ll 1$ so at the sense axis resonant frequency, the voltage at the output of the pre-amp is simply a scaled inverted replica of the output voltage. The state equations are given by the state evolution equation for this stage as presented in Equation 2.4.4 and the output equation,

$$V_{pre} = -\frac{R_g}{R_b}(x^* + V_N(1+\frac{C_N}{C_{fb}}))$$
(2.4.6)

2.3.1 Simplified Pre-Amplifier Model

Simplifying the model permits a quick analysis of several important issues. First, it clearly shows that the signal at the output of the pre-amplifier is composed of four terms: signal, feedthrough, error, and a constant term. This leads to a description of feedthrough and an order of magnitude calculation in order to understand its effect on the output. Finally, the output voltage of the pre-amp is proportional to the position of first proof mass. This fact is verified using a simplified analysis that deals with the issue of unmatched capacitor area. The noise sources are discarded here.

For the left sense plate capacitor, C_{1s}, the voltage will produce a charge Q_s one the electrode. Assuming that the resistance in the feedback path is large, the charge residing at the output node of the operational amplifier will be $-Q_s$. The voltage at the output of the operational amplifier, due to all four capacitors, is given by,

$$V_{out} = \frac{-Q_{1s}}{C_{fb}} + \frac{-Q_{2s}}{C_{fb}} + \frac{-Q_{1t}}{C_{fb}} + \frac{-Q_{2t}}{C_{fb}}$$
(2.4.7)

The total charge can be represented as the summation of the individual charges.

49

$$Q_T = Q_{1t} + Q_{2t} + Q_{1s} + Q_{2s} = (\alpha_1 C_{s0} + \Delta C_{1s}(t))V_{1s} + (C_{s0} + \Delta C_{2s}(t))V_{2s} + (\alpha_2 C_{t0} + \Delta C_{1t}(t))V_{1t}(t) + (C_{t0} + \Delta C_{2t}(t))V_{2t}(t)$$

(2.4.8)

where the time dependent capacitance has been expressed to first order and the mismatch in sense area capacitance has been expressed with the α_1 term. Since the force plates are much smaller, they have been assumed to be equal. The electrode voltage terms in Equation 2.1.4 are rewritten,

$$V_{1s} = \alpha_3 V_c \qquad V_{1t} = \alpha_4 V_a + \alpha_5 V_b csq(\omega t)$$
$$V_{2s} = -V_c \qquad V_{2t} = -V_a + V_b csq(\omega t)$$

(2.4.9)

where α_2, α_3, and α_4 are introduced into the electronics to provide three degrees of freedom. In general these terms will be used to null the capacitance area mismatch for the sense plates.

Now, the vertical forces on each plate, in the simplified model, are written explicitly in Equation 2.1.9 and are proportional to the voltage squared on each plate. Thus, the force on each proof mass goes as,

$$F_1 \propto -A_t[(\alpha_4 V_a)^2 + (\alpha_5 V_b)^2 + 2\alpha_4\alpha_5 V_a V_b csq(\omega t)] - A_s(\alpha_3 V_c)^2$$
$$F_2 \propto -[V_a^2 + V_b^2 - 2V_a V_b csq(\omega t)] - A_s V_c^2$$

(2.4.10)

In a second order oscillator, the motion is known to lag the force by 90° and the changing capacitance is 180° out of phase with the motion. Thus, the delta capacitance terms can be written as

$$\Delta C_{1s} = \delta_{cs}\alpha_6 \sin(\omega t) \qquad \Delta C_{1t} = \delta_{ct}\alpha_7 \sin(\omega t)$$
$$\Delta C_{2s} = -\delta_{cs} \sin(\omega t) \qquad \Delta C_{2t} = -\delta_{ct} \sin(\omega t)$$

(2.4.11)

Figure 2.10 and Figure 2.11 have been constructed to show the basic first harmonic signal relationships for the bias and drive voltages of $V_{pvr}=15V$ and $V_b=1mV$. It is clear that the force on plate 1 is in phase with a negative cosine. The position lags the force by 90° at resonance and the capacitance is 180° out of phase with the position.
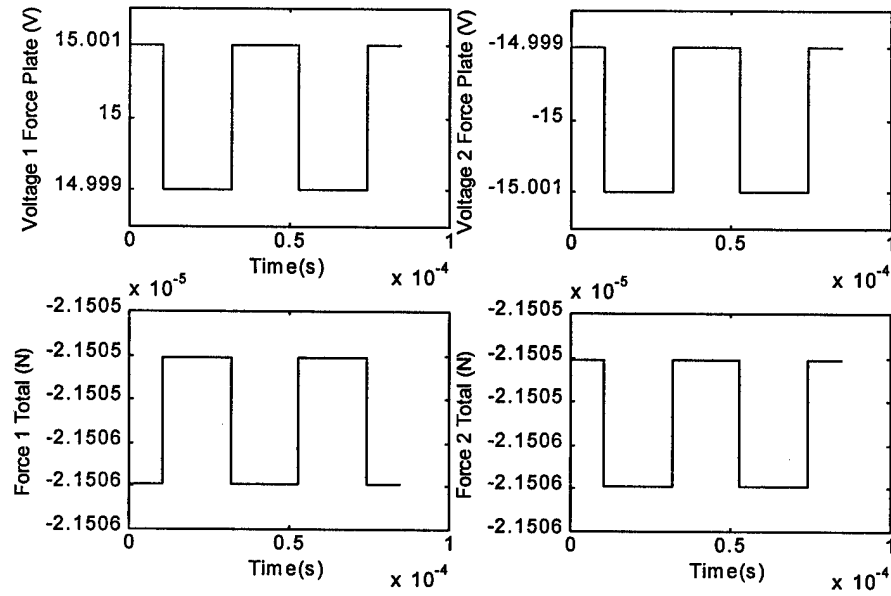
Figure 2.10. Basic Linear Signal Relationships
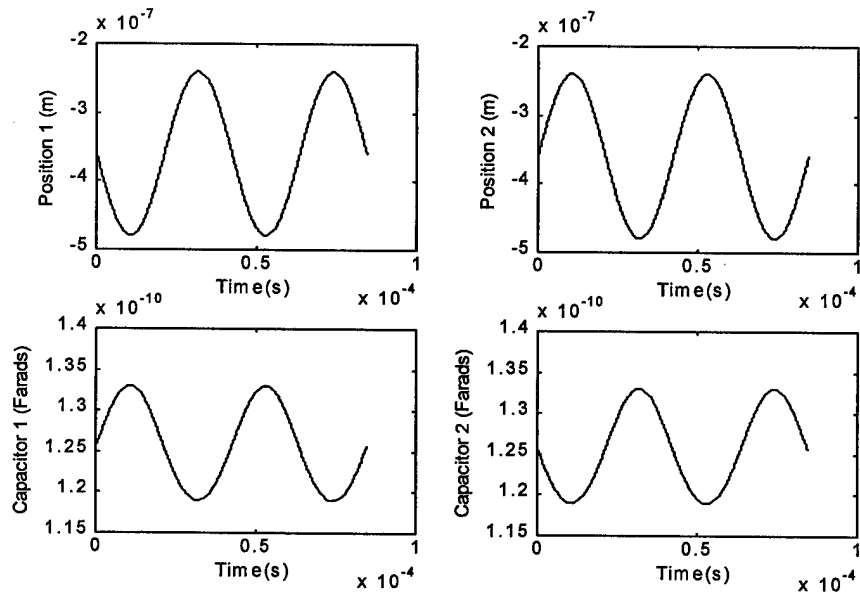
Figure 2.11. Basic Linear Signal Relationships

Substituting Equations 2.4.9 and 2.4.11 into 2.4.8 gives an expression for the total charge on the proof mass. The expression contains four terms. The first and third terms are the DC components,

the second and fifth are the desired signal terms, the fourth is the feedthrough term, and the last is the error term which is a higher harmonic.

$$Q_T = (\alpha_1\alpha_3 - 1)C_{s0}V_c + (\alpha_3 + \frac{1}{\alpha_6})\Delta C_{1s}V_c + (\alpha_2\alpha_4 - 1)C_{t0}V_a +$$

$$(\alpha_2\alpha_5 + 1)C_{t0}V_b csq(\omega t) + (\alpha_4 + \frac{1}{\alpha_7})\Delta C_{1t}V_a + (\alpha_5 - \frac{1}{\alpha_7})\Delta C_{1t}V_b csq(\omega t)$$

(2.4.12)

Using the two degrees of freedom in the electronics design, it is possible to null out the DC terms and the error term. If the plates are perfectly matched, these two terms will not exist. This leaves the feedthrough term as the only undesired term.

The biasing could also be accomplished by putting the same bias on each plate and drive signals 180° out of phase. The motion of the proof masses is still out of phase because this method nulls the signal and feedthrough term. The disadvantage of this method is that the measured term becomes the error term and comes out at twice the resonant frequency with a small magnitude. The nulling circuits will not be discussed further at this time. For further analysis, it is assumed these are in place. This assumption is equivalent to assuming that the plates are matched.

Now, the output voltage will be further simplified to show the signal is in phase with the position of the first proof mass. Assuming that the term due to feedthrough is negligible and that the plates are perfectly matched, the output voltage is given by

$$V_{out} = -\frac{(2\Delta C_{1s}V_c + 2\Delta C_{1t}V_a)}{C_{fb}}$$

(2.4.13)

Now, the delta capacitance terms are calculated explicitly using an expansion. The equation for the capacitance for the sense plate is given by,

$$C_{1s} = \frac{\gamma\varepsilon_0 A_s}{Y_0 + y_1} = \frac{\gamma\varepsilon_0 A_s}{Y_0}(1 - \frac{y_1}{Y_0} + ...)$$

(2.4.14)

52

which can be written,

$$C_{1s} = C_{s0} + \Delta C_{1s} = \frac{\gamma \varepsilon_0 A_s}{Y_0} - \frac{\gamma \varepsilon_0 A_s}{Y_0^2} y_1 \qquad (2.4.15)$$

The capacitance term for the force plate can be written in the same manner. Substituting the value for the ΔC_{1s} and ΔC_{1t} into Equation 3.4.13 and letting both bias voltages equal the PVR voltage produces a simple expression for the output voltage.

$$V_{out} = \frac{2\gamma \varepsilon_0 A V_{PVR}}{Y_0^2 C_{fb}} y_1 \qquad (2.4.16)$$

Under ideal conditions, the voltage at the output of the pre-amp will be proportional to the position of the first proof mass.

2.4 Feedthrough

Now, it is shown that the feedthrough term will not destroy the signal term. In this case, the feedthrough term is a square wave while the signal term is sinusoidal. For simplicity, all α terms are set to unity which closely resembles the actual situation. Under these assumptions, the output voltage, V_{out}, is given by,

$$V_{out} = - \left[\frac{2\Delta C_{1s} V_c + 2 C_{t0} V_b csq(\omega t) + 2\Delta C_{1t} V_a}{C_{fb}} \right] \qquad (2.4.17)$$

which includes only the feedthrough and signal terms. First, the feedthrough term will be examined. The expressions for the delta capacitance and the DC capacitance terms were found in the previous section. Although the governing equations are nonlinear, it is possible to write the steady state solution for the first proof mass with a first order approximation in the form, $y = y_c - y_p \sin(\omega t)$. Grouping the DC displacement with Y_0, the capacitance terms are now written,

53

$$C_{s1} = C_0 + \Delta C_1 = \frac{\gamma \varepsilon_0 A_f}{(Y_0 + y_c)} + \frac{\gamma \varepsilon_0 A_f}{(Y_0 + y_c)^2} y_p \sin(\omega t) \qquad (2.4.18)$$

where the dependence on the bias voltage in Y_0 is now contained in y_c.

Now, the feedthrough term can be written,

$$Feedthrough = -2V_b \frac{\gamma \varepsilon_0 A_t}{(Y_0 + y_c)} \frac{1}{C_{fb}} csq(\omega t) \qquad (2.4.19)$$

The signal term is found in a similar manner. Using the expression for the delta capacitance term developed above, the signal term is expressed

$$Signal\_Term = -\frac{2}{C_{fb}} \frac{\gamma \varepsilon_0 (A_t V_a + A_s V_c)}{(Y_0 + y_c)^2} y_p \sin(\omega t) \qquad (2.4.20)$$

Both of these signals are shown in Figure 2.12 with the feedthrough term magnified by 10e3. The estimate used bias voltages of V_{pvr}=15V and V_b=1mV.

54
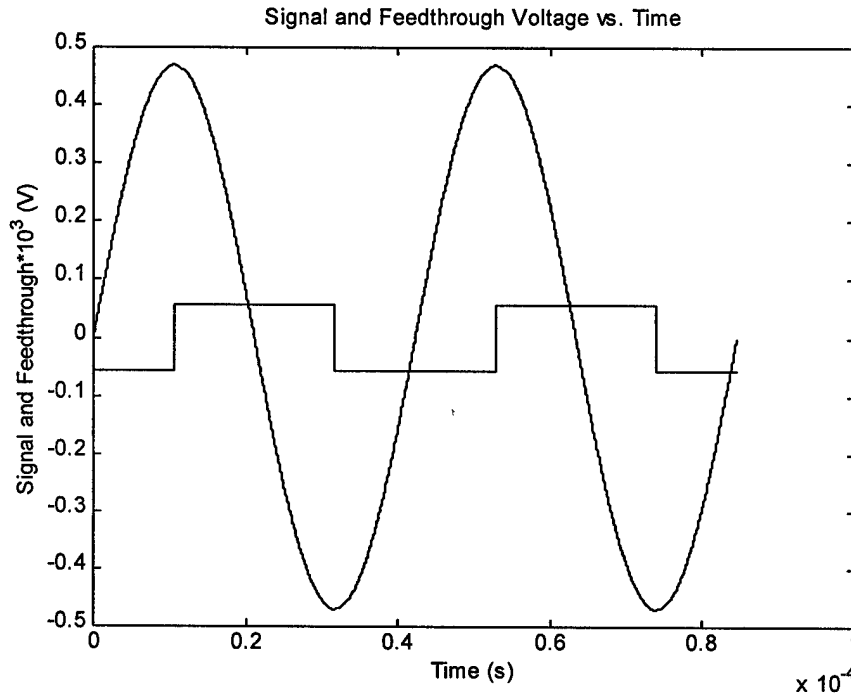
Figure 2.12. Signal and Feedthrough Waveforms

The signal to feedthrough ratio is approximately 8.4e3 V/V and in quadrature to the position signal so demodulation is capable of removing most of the feedthrough.

The demodulation will remove most of the feedthrough; however, the feedthrough term will shift the frequency of the resonator. For a first order estimate of the frequency shift, the resonator and preamplifier is modeled as a black box. The input is the probe voltage $V_b csq(\omega t)$ and the output is the preamplifier voltage. The model is shown below.
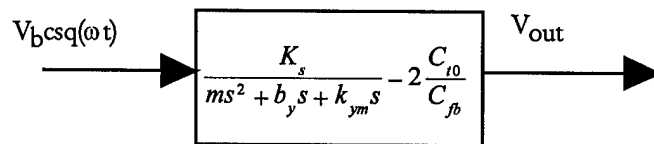
Figure 2.13. Feedthrough Model

55

where,

K_s = the oscillation amplitude to output voltage gain

The constant term in the transfer function represents the feedthrough term and other term is the resonator term without the cubic. First, assume the feedthrough term is eliminated. When the loop is closed, the resonator will operate at 90° of phase shift. The addition of the feedthrough term will change the phase characteristic and the frequency of the 90° phase will shift slightly. In high Q systems, the sharp phase transition causes the shift to be small. In this system, there was no frequency shift with a frequency resolution of 0.01 rad/s or .08ppm. The feedthrough does not significantly alter the resonant frequency and the quadrature signal can be eliminated using demodulation.

THE CLOSED LOOP MODEL

3. Overview of Closed Loop Controllers

The two controllers modeled in this section represent the second major subsystem for the PVR. A self excitation loop is presented that sustains vertical oscillations of the resonator. The phase locked loop is also presented and the frequency control of the device is examined. The components of both the oscillator loop and phase locked loop are presented along with their state space description. The stability of the oscillator loop depends entirely on the magnitude of the cubic nonlinearity. The stability analysis extends the analysis of the Duffing Equation in the previous chapter. The goal of this chapter is to explain the overall operation of the PVR from the block diagram, develop a state space model for the closed loops, and develop a stability criterion for the oscillator loop.

3.1 The Closed Loop Micromechanical Oscillator

The oscillator loop and phase locked loop are shown for a single resonator in Figure 3.1. The loop on the left, the oscillator loop, is a simple feedback loop that insures sustained oscillations are maintained in the plant. The loop on the right is the frequency control loop or phase locked loop which locks the resonator frequency to the reference frequency. Since there is no phase information carried from the frequency comparison to the PVR voltage, a minimal requirement is frequency lock. However, the phase lock provides for more robust frequency lock. Without the phase lock, several cycles will slip before the frequency changes and corrections are brought around the loop. The macro model of the voltage controlled oscillator(VCO) simplifies the dynamics of the micromechanical resonator discussed in the previous chapter.
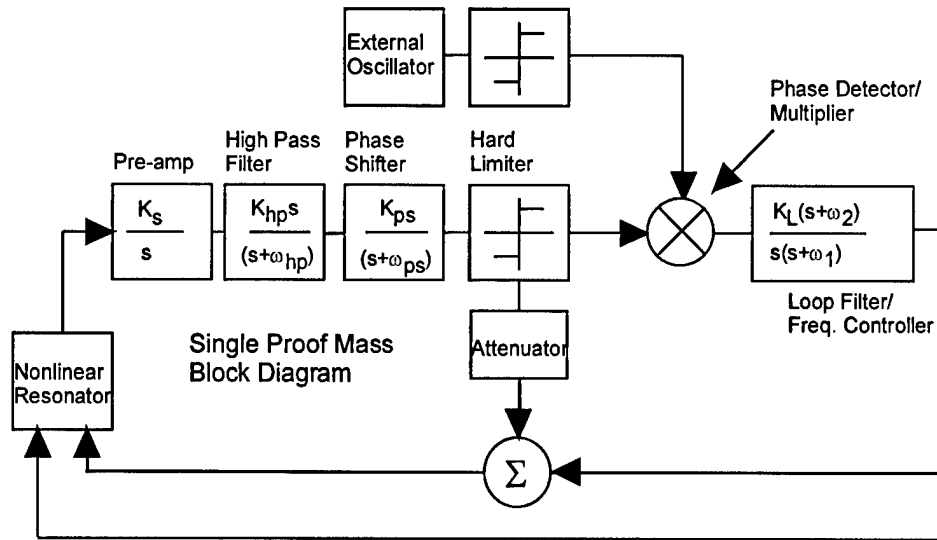
Figure 3.1. Single Proof Mass Block Diagram

The oscillator loop is shown in the left of Figure 3.1. The oscillator loop is very similar to a classic active filter tuned oscillator with filtering equivalent to a bandpass. The criteria for sustained oscillations include unity magnitude and zero phase of the loop gain [6].

The signal path through the block diagram begins with the injected current coming off the proof masses passing through the charge amplifier which acts as an integrator. The amplitude of the first harmonic of the output voltage from the integrator is proportional to the position of the proof mass. The signal is then high passed to eliminate any DC value. Next, the signal is phase shifted +90° by a low pass filter with a pole frequency much less than the eigenfrequency of the resonator. The first harmonic is essentially integrated and inverted in this stage. Finally, the sinusoid is hard limited and the resultant square wave passes through an attenuator to produce the small amplitude drive signal. If the frequency control loop is not closed, the square wave signal is added to an externally supplied positive and negative DC signal which substitutes for the PVR voltage. Finally, these signals are applied to the sense plate which results in a phase shift of -90° from the force to position transfer function. The output of the preamplifier is proportional to position and the -90° is from the input of the resonator to the output of the preamplifier. Thus, there is a total phase shift of 360° around the loop and high gain. The PVR voltage at the output of

58

the loop filter is summed with the signal out of phase with the force and applied to the force electrode. The PVR voltage is also applied to the sense electrode. The oscillation loop self excites the oscillator by applying a force that is in phase with the velocity of the proof mass and at the frequency of oscillation. In a more advanced device the magnitude of the sinusoid signal added to the PVR voltage will be adjusted in order to maintain amplitude control. The typical operating amplitude is 10% of the nominal gap distance. The amplitude control loop is not accomplished in this thesis.

The second loop is slightly more complicated. An external reference frequency is hard limited and compared with the hard limited frequency input from the oscillator. These signal are passed to a phase detector (PD) whose DC output is a voltage proportional to the difference in phase. The PD acts as a mixer or multiplier so additional high frequency components exist. These are attenuated by sending this signal through a loop filter which has a low pass characteristic before it is finally amplified and the appropriate precision voltage reference signal results. The PVR voltage is applied to the VCO which produces a signal whose frequency is a nonlinear function of the PVR voltage. The PLL adjusts the PVR voltage until the frequency of oscillation in the resonator matches that of the external reference.

In addition, the frequency control loop acts as an amplitude control loop if the pressure in the package does not change as discussed in following chapter. The PLL sets an upper bound on the amplitude because as the damping increases, the pressure increases, and the amplitude decreases. An increase of pressure due to leakage can only result in a lower amplitude.

3.2 Components of the Oscillator Loop

As indicated in section 3.1, the oscillator loop is shown in the left in Figure 3.1; it consists of the micromechanical resonator, the preamplifier, high pass filter, 90° phase shifter, hard limiter, and attenuator. Each of the components of the self exciting oscillator loop are examined in the state space form used to implement the numerical simulation of this loop. It is assumed throughout that a steady state oscillation or limit cycle does exist at the resonant frequency of the system.

3.2.1 State Space Model for the Resonator

The simulations require the use of a large and small amplitude model. The small amplitude model can be written in linear state space form while the large amplitude model cannot.

Simulation of the large amplitude model requires the use of the nondimensionalized dynamic equation for a single proof mass, Equation 2.2.4.

$$\ddot{\tilde{y}} + \frac{1}{Q}\dot{\tilde{y}} + \frac{k_{ym}}{k_y}\tilde{y} = -\frac{1}{2}\gamma\varepsilon_0 \frac{(A_t V_t^2 + A_s V_s^2)}{(Y_0 + y_0\tilde{y})^2}\frac{1}{k_y y_0} \tag{3.2.1}$$

This equation can be written in state space form as two first order differential equations.

$$\frac{d\dot{\tilde{y}}}{dt} = -\frac{1}{Q}\dot{\tilde{y}} - \frac{k_{ym}}{k_y}\tilde{y} - \frac{1}{2}\gamma\varepsilon_0 \frac{(A_t V_t^2 + A_s V_s^2)}{(Y_0 + y_0\tilde{y})^2}\frac{1}{k_y y_0} \tag{3.2.2}$$

$$\frac{d\tilde{y}}{dt} = \dot{\tilde{y}} \tag{3.2.3}$$

where,

$$x_1 = y \qquad x_2 = y' \tag{3.2.4}$$

are used as the state variables. Using x_1 and x_2 as state variables, these two equations are used to simulate the dynamics of the proof mass.

The nonlinear differential equations for the resonator can be written in linear state space form using the small amplitude model for the resonator dynamics shown in Equation 2.2.6. The nonlinear stiffness terms are linearized with the use of describing functions. The describing function is defined as the ratio of the amplitude of the first harmonic component of the output and input signals. In general, this expression is a function of the amplitude and frequency of the input signal. The describing function used in this thesis corresponds to sinusoidal input signals.

60

The cubic describing function is easily obtained by expanding a cubed sinusoid, substituting basic trigonometric relationships, and examining the amplitude of the resulting fundamental harmonic. The output of a simple cubic function is,

$$y = \widetilde{k}_{3y} x^3 \qquad (3.2.5)$$

Now, assume the input sinusoidal function is normalized and given by,

$$x = \widetilde{A} \sin(\omega t) \qquad (3.2.6)$$

Inserting 3.2.6 into 3.2.5 and expanding the cubed sine term produces an expression that includes an output term at the fundamental resonant frequency. The ratio of the output amplitude of input amplitude is given by,

$$N_c(\widetilde{A}, \widetilde{\omega}) = \frac{3}{4} \widetilde{k}_{3y} \widetilde{A}^2 \qquad (3.2.7)$$

where the notation for the lumped parameter cubic term has been used. This linearization allows the normalized linear spatial frequency to be written,

$$\widetilde{k}_r = 1 + \frac{3}{4} \widetilde{k}_{3ye} \widetilde{A}^2 = 1 + \frac{3}{4} \frac{k_{3ye}}{k_y} A^2 \qquad (3.2.8)$$

The describing function for a quadratic term does not exist because it does not produce any terms at the fundamental harmonic. The symmetry of the oscillator should minimize the effects of the quadratic or in general, any even stiffness term. This was seen in the analysis in section 2.3.1 where the DC output signal was shown to be zero if the two proof masses were perfectly matched. Since the plates are moving out of phase, the current from one proof mass due to the quadratic term should be canceled by the other plate just as the DC component. For these reasons, the quadratic term is discarded in writing the state space model.

Finally, the linear state space model can be written for both proof masses. The left proof mass is labeled one, the right proof mass is labeled two and the state space variables for the second order system are the position and velocity of each proof mass. Given these assumptions, the linearized state evolution equation can be written

$$\frac{d}{dt}\begin{bmatrix} \tilde{y}_1 \\ \dot{\tilde{y}}_1 \end{bmatrix} = \begin{bmatrix} 0 & 1 \\ -(1+\frac{3}{4}\tilde{k}_{y3}\tilde{A}^2) & -\frac{1}{Q} \end{bmatrix}\begin{bmatrix} \tilde{y}_1 \\ \dot{\tilde{y}}_1 \end{bmatrix} + \begin{bmatrix} 0 \\ 1 \end{bmatrix}\begin{bmatrix} \tilde{F}_{y1} \end{bmatrix} \qquad (3.2.9)$$

This state space model of the proof mass dynamics is based upon small amplitude operation. If both resonators are considered to be perfectly matched, the injected current on each proof mass is the same and the single resonator model is used. The linearized state space model for both proof masses is easily written from Equation 3.2.9 assuming that only the out-of-phase mode is excited.

3.2.2 Preamplifier, Gain Stage, Phase Shifter, and Hard Limiter

The preamplifier was modeled in the previous chapter along with the high pass filter used as a gain stage with Equations 2.4.2, 2.4.4, and 2.4.6. The phase shifter can be modeled as a low pass filter with the break frequency much less than the eigenfrequency of the resonator. The transfer function for the stage is given by

$$T_{ps}(s) = \frac{K_{ps}}{s + \omega_{ps}} \qquad (3.2.10)$$

where,

K_{ps} = the DC gain of the filter (negative), and

ω_{ps} = the break frequency of the phase shifter.

This equation can be transformed into a differential equation and nondimensionalized:

$$\dot{V}_{ps} = V_{pre} \frac{K_{ps}}{\omega_n} - V_{ps}\tilde{\omega}_{ps} \qquad (3.2.11)$$

where,

$\tilde{\omega}_{ps} = \omega_{ps}/\omega_n = 0.01$ = normalized break frequency

V_{ps} = voltage at the output of the phase shifter

Placing the break frequency two decades before the eigenfrequency of the resonator, the phase of the low-pass filter will be approach 90° at the eigenfrequency. Proper design will insure the gain at the eigenfrequency is approximately unity.

The voltage at the output of the phase shifter is passed through a hard limiter. The hard limiter will contain some amount of hysteresis. This can be modeled with the following algorithm.

$$V_{hl} = \begin{cases} +1 & \text{if } V_{ps} > \delta \text{ and } V_{hl} = -1 \\ -1 & \text{if } V_{ps} < -\delta \text{ and } V_{hl} = 1 \end{cases} \qquad (3.2.12)$$

where,

$\delta = 0.003$ V = the hysteresis width of the relay

This completes the oscillator loop. The loop will sustain oscillation because there is a total of 360° around the loop. The resonator contributes -180° from the voltage to force function and another -90° from the force to position, or output voltage, function, the high-pass filter contributes another -180°, and the phase shifter contributes +90°. Steady state oscillations will result in this loop.

3.3 Components of the Phase Locked Loop

The frequency control loop in shown on the right side in Figure 3.1. The frequency control loop (PLL) contains the resonator, the phase detector, and loop filter. Under ideal assumptions, the

voltage that appears after the hard limiter will be a signal out of phase with the velocity of the first proof mass. This signal is compared with the external oscillator in the phase detector.

The operation of the phase detector can be modeled as a mixer or four quadrant multiplier. One typical analog multiplier which is useful in the simulations uses two sinusoidal inputs. Assume that the input sinusoids are given by the following two signals.

$$x_1(t) = A_1 \cos(\omega_1 t) \qquad x_2(t) = A_2 \cos(\omega_2 t + \phi_{err}) \qquad (3.3.1)$$

If the frequencies of both signals are equal and the second harmonic component is ignored due to filtering, the phase/voltage characteristic is given by

$$V_{pd} = \frac{\alpha A_1 A_2}{2} \cos(\phi_{err}) \qquad (3.3.2)$$

where α equals the gain of the phase detector. The linearized phase/voltage characteristic in the vicinity of $\pi/2$ is

$$V_{pd} = K_{D1}\phi_{err} = -\frac{\alpha A_1 A_2}{2}\phi_{err} \qquad (3.3.3)$$

In the phase detector used in the hardware, a digital phase detector is used which functions as an exclusive OR gate. Square waves are used as the input to this device with an upper and lower value of $-V_{ss}$ to V_{ss}. The voltage at the output of the phase detector is approximated with the following transfer characteristic.

$$V_{pd} = K_{D2}\phi_{err} = \frac{2V_{ss}}{\pi}\phi_{err} \qquad -\frac{\pi}{2} < \phi_{err} < \frac{\pi}{2} \qquad (3.3.4)$$

Both of these phase detectors lock with a steady state phase error of 90°.

The loop filter is a proportional plus integral controller with an additional low pass. The general form is shown in Figure 3.1. This equation is easily converted to state space form and expressed in the following state space equations.

$$
\begin{bmatrix} \dot{x}_1 \\ x_2 \end{bmatrix} = \begin{bmatrix} 0 & 0 \\ 1 & -\omega_1 \end{bmatrix} \begin{bmatrix} x_1 \\ x_2 \end{bmatrix} + \begin{bmatrix} K_L \omega_2 \\ K_L \end{bmatrix} u
$$
$$
y = \begin{bmatrix} 0 & 1 \end{bmatrix} \begin{bmatrix} x_1 \\ x_2 \end{bmatrix} + \begin{bmatrix} 0 \end{bmatrix} u
$$

(3.3.5)

where,

$$
x_1 = \frac{K_L \omega_2 V_{pd}}{s} = \text{arbitrary first state variable, and}
$$

x_2 = PVR voltage and output state, and

K_L = loop filter gain coefficient, and

$V_{pd} = u$ = phase error signal from the phase detector and input signal

This completes the PLL modeling. The loop filter was chosen because of the integrator in the forward path allows steady state errors to be integrated out. The lead and lag terms provide the necessary gain and phase margin. Additionally, the lag term provides attenuation to the periodic output of the phase detector that is at twice the eigenfrequency of the resonator. The PLL integrates the phase error to zero and forces the external oscillator and the micromechanical resonator to be identical in frequency. The operation of the PLL is addressed further in chapter 6 which discusses the hardware used to implement the controller.

3.4 Stability of the Oscillator Loop

Previous results with an oscillator loop for a single element micromechanical resonator indicated that the stability of the limit cycle is dependent upon the cubic nonlinearity; but was unconfirmed [8]. The existence of a limit cycle and stability criterion are confirmed here.

The Duffing Equation given in Equation 2.2.6 simplifies to a self excitation loop similar to a classic van der Pol Oscillator when the oscillator loop is closed [10]. A simplified model for the oscillator loop is shown in Figure 3.2 below.

The closed loop form of the Duffing Equation is,

$$\ddot{\tilde{x}} + (\frac{1}{Q} - \tilde{K}_f N_{HL})\dot{\tilde{x}} + (1 + N_{CS})\tilde{x} = 0 \qquad (3.4.1)$$

where,

N_{CS} = describing function for a cubic spring, and

N_{HL} = describing function for a hard limiter, and

$\tilde{K}_f$ = nondimensionalized forcing constant.
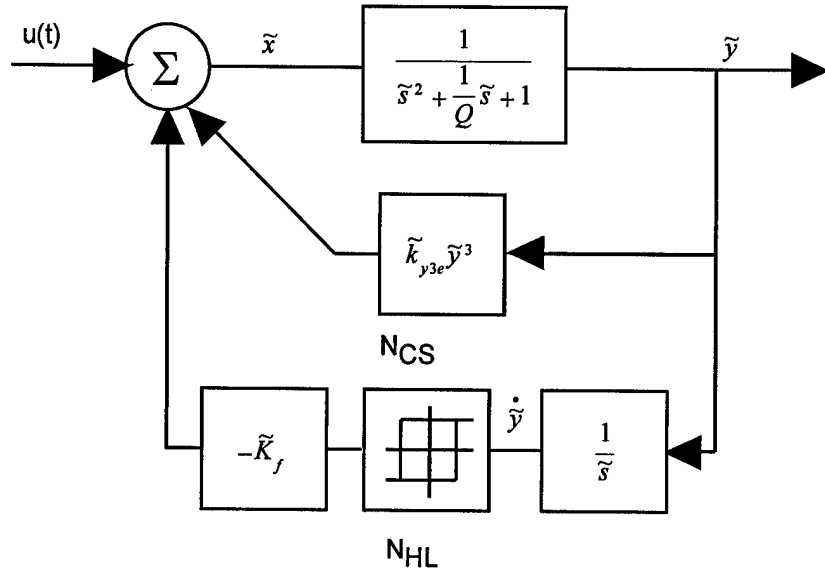
Figure 3.2. Simplified Oscillator Control Loop

The damping will be negative at small amplitudes and positive at large amplitudes due to the self excitation signal. Somewhere in between these extremes, there exists a point where the average damping over a cycle is zero and steady oscillations are maintained. The limit cycle occurs when the velocity coefficient goes to zero.

$$\frac{1}{Q} = \tilde{K}_f N_{HL} \tag{3.4.2}$$

The approach to the limit cycle from both extremes is shown dramatically in Figure 4.6 and Figure 4.8 which depict the full oscillator loop start-up transient. The simulations for the stability analysis performed here use an initial condition to place the resonator close to the limit cycle.

The derivation of the stability criterion for this limit cycle is performed by Kossuth [8]. Perturbations are applied to the amplitude and frequency in the characteristic equation for the closed loop. The stability criterion for the oscillator loop is derived using a Taylor expansion, assuming small k_{y3e} and large Q. The stability criterion is given by,

$$2 + \frac{15}{4}\tilde{k}_{y3} > 0 \tag{3.4.3}$$

which implies a stable system for $\tilde{k}_{y3} > -0.5333$. However, as $\tilde{k}_{y3}$ increases, the Taylor expansion used in the derivation no longer applies.

The results of simulations with the oscillator loop for the resonators confirm the stability criterion and agree well with the predicted results, given the breakdown of the approximation at large amplitudes. The simulations used the state space equations presented in section 3.2 for the oscillator with V_{pvr}=15V and V_b=1mV. All of the simulations used an initial position condition to place them close to steady state. Figure 3.3 shows the position signal for the $\tilde{k}_{y3}$ values listed below each subplot. These plots neglect the limit of snapdown in order to illustrate the approach to instability. The initial plot is the position with a normalized cubic stiffness of -0.0041. As the normalized cubic stiffness value becomes more negative, the frequency visibly decreases due to spring softening and the amplitude of oscillation increases dramatically.
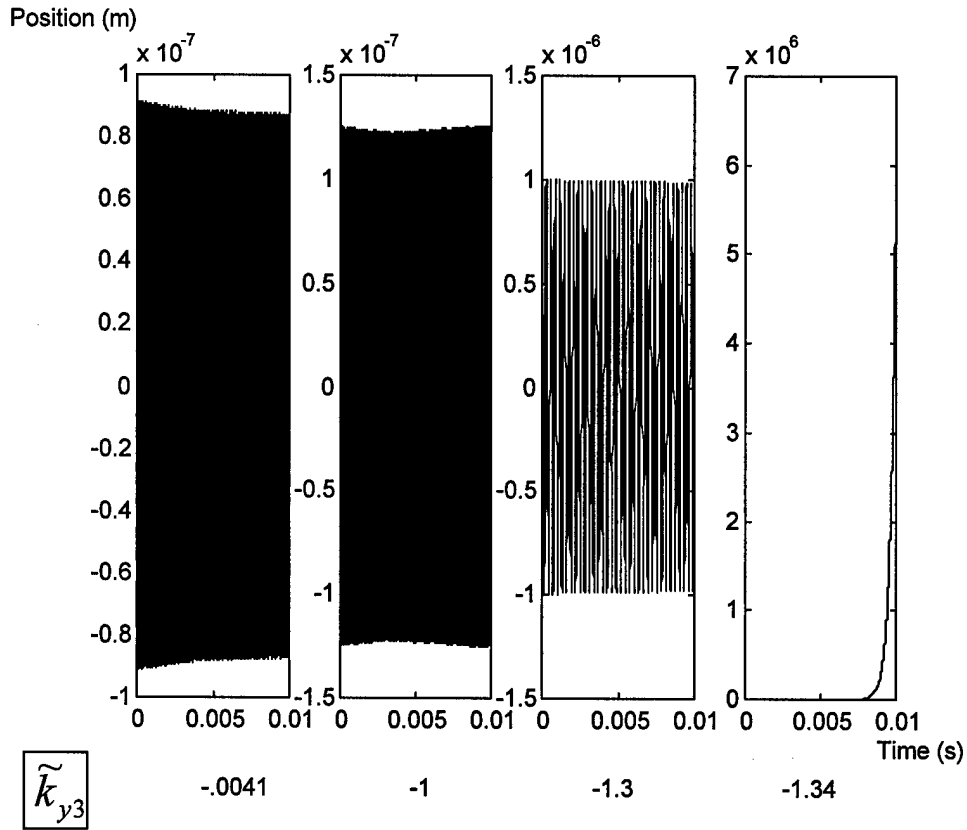
Figure 3.3. Position Signal for Various Cubic Nonlinearity Values

As the amplitude quickly rises, the Taylor expansion used to derive Equation 3.4.3 is no longer applicable. The simulations determined the stability point to be at $\tilde{k}_{y3}$ = -1.34 where the position diverges. Figure 3.4 displays the phase plane plots accompanying the position series plots.
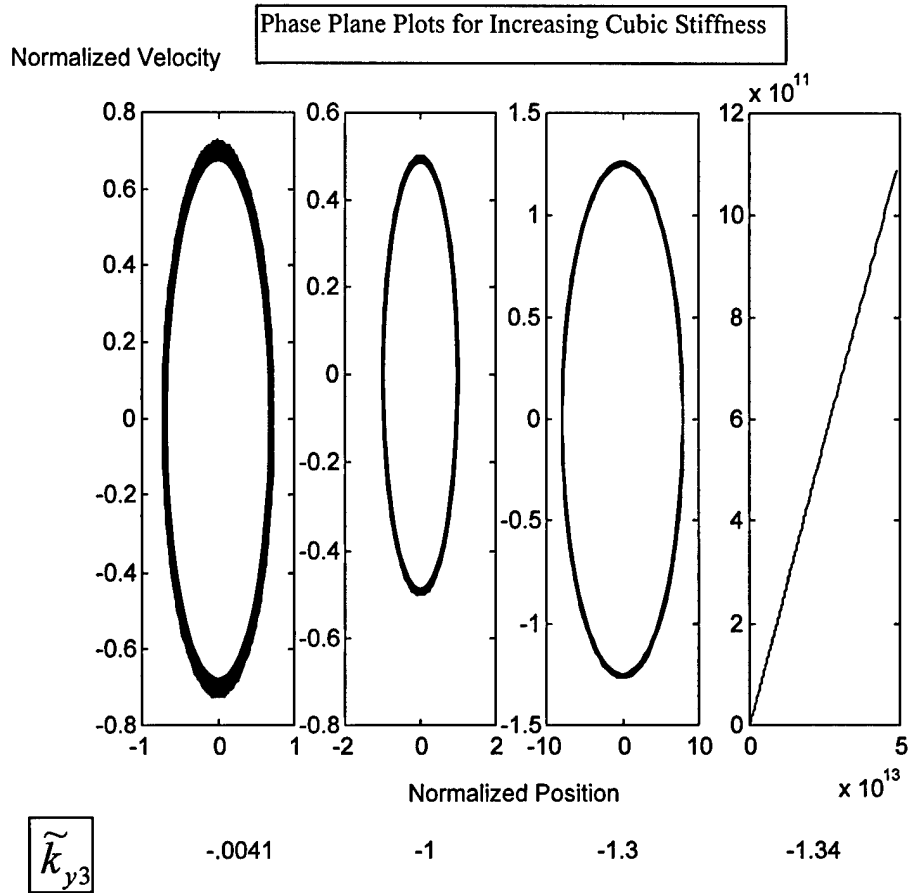
Figure 3.4. Phase Plane Plot of Nondimensional Position and Velocity

It is clear that a stable limit cycle exists for the first three while the fourth simulation diverges.

The unstable point does not pose a problem for the operation of the PVR. There are no realistic biasing conditions which would create a cubic nonlinearity value required for instability.

Chapter 4

BASELINE DESIGN AND MODEL SIMULATIONS

4. Overview

The first order design analysis and baseline design are presented in this chapter. The closed loop, nondimensionalized, one-dimensional, lumped parameter model was simulated using Matlab© with the files contained in Appendix B. The nonlinear, second-order equation was separated into two standard form first-order differential equations. The resonator was represented with the state space model in Equations 3.2.2 and 3.2.3. The preamplifier and gain stage were modeled using equations 2.4.4 and 2.4.6. The phase shifter model is shown in Equation 3.2.11 and the hard limiter in Equation 3.2.12. Finally, the phase detector was modeled with a sinusoidal detector as shown in Equation 3.3.2 and the loop filter state space model is given in Equation 3.3.5. Several cases were run to examine different aspects of the startup and steady-state behavior of the oscillator and PLL loop.

4.1 Hand Results and Baseline Design

The first order design analysis was conducted to determine the feasibility of the PVR. It was also used to create an optimized baseline design and a prototype design. The design analysis used first-order approximations for many steady state system characteristics such as output amplitude of the resonator and oscillation amplitude of the proof masses. The total design analysis is presented in Appendix A in the Excel© worksheet along with the formulas for all the approximations. Both the baseline and prototype design are presented in full. The items written with a star before the name are entered into the spreadsheet while the other parameters are calculated using first order approximations. The parameters of interest in both designs are presented in Table 4.1.

71

Table 4.1. Baseline and Prototype Design Parameters

	Prototype Design	Optimal Design
mass, m	2.73e-9 kg	3e-9 kg
zero bias gap, $Y_0(0)$	2.5e-6 m	2.5e-6 m
total area, A	1.35e-7 m²	1.6e-7 m²
quality factor, Q	19190	4500
zero bias resonant frequency, ω_0	26850 rad/s	26850 rad/s
PVR voltage, $V_{pvr} = V_a = V_c$	15 Volts	15 Volts
Probe voltage, V_b	1 mV	1 mV
Drive Amplitude	1.25e-7 m	1.16e-8 m

All simulations will use the prototype design.

4.2 Simulations

The following simulations looked at both the phase locked loop, the oscillator loop, and the full PVR model for the prototype design. The several cases used in each simulation confirmed the desired operation of the loop and helped to analyze the effects of perturbations in certain parameters. The following chapter introduces the perturbations analyses used to satisfy system requirements on the PVR.

72

4.2.1 Phase Locked Loop Simulations

The phase locked loop simulations of the resonators used the phase detector model, loop filter model, and a VCO with the transfer characteristic K_0/s , where the $1/s$ accounts for the integration from frequency to phase and K_0 is the frequency gain with units rad/sec/V. The transfer characteristic given above was used for the VCO in place of the full resonator equations, 3.2.2 and 3.2.3. The simplification was used in order to reduce the simulation time by eliminating the long time constant associated with the resonator.

The phase locked loop contains a nonlinear VCO given by the transfer characteristic shown in Figure 1.4. In the first group of simulations, a linear VCO was used while the second group of simulations used the full nonlinear VCO. In all simulations, it is assumed that the oscillator loop is closed and has locked onto the resonant frequency. All the initial states are set to a value of zero.

4.2.1.1 Linear Simulations

The linear VCO simulation used a value for K_0 such that for an input voltage equal to the desired PVR voltage, the output frequency is equal to the frequency obtained from the nonlinear VCO for that input voltage. This will simplify comparisons between the linear and nonlinear simulations. The acquisition of lock is a complicated process that depends on many parameters in the phase locked loop. This loop design will theoretically always acquire lock; however, there exists two distinct regimes for the phase locked loop. The definition of these two regimes is done with the loop bandwidth of the PLL. The initial difference in frequency will lie on one side or the other of this bandwidth. Both of these regimes are simulated in this section.

The first simulation uses a desired precision voltage of 5 V. This is accomplished by setting the external oscillation frequency to the frequency corresponding to the desired precision voltage according to Figure 1.4. The electrostatic characteristic shows the shift in frequency from zero bias to 5 V is approximately 330 Hz which is within the designed bandwidth of the closed loop described in chapter 6 and defines the first distinct region of acquisition. The acquisition of lock is shown in Figure 4.1, where the precision voltage rises quickly to 5 V. This signal is unfiltered and

contains a high frequency component at twice the resonant frequency from the phase detector since this device locks at 90° of phase difference.

Acqusition of Lock for Linear VCO

Desired Precision Voltage of 5 V
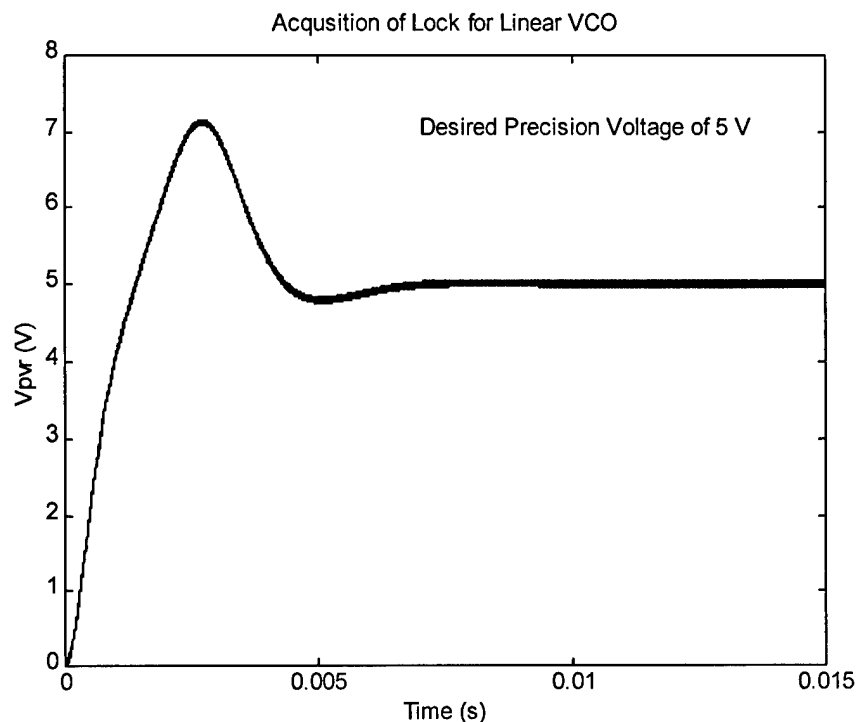
Figure 4.1. Acquisition of Lock for Linear VCO

In Figure 4.2, the desired precision voltage reference is 7 V and the difference in zero bias frequency to full bias (7 V) frequency is approximately 655 Hz and larger than the loop gain bandwidth of the PLL. The acquisition phase takes considerably longer in this case. The initial difference in frequencies at the phase detector is large and the output has large oscillations at the difference frequency. As the voltage oscillates, the VCO alternately moves closer and further from the reference frequency. When the VCO frequency moves towards the reference, the difference frequency decreases. This causes the voltage sinusoid to have an asymmetrical waveform with a larger amplitude as the VCO frequency moves toward the reference [6]. This results in a slight DC voltage that is integrated and ultimately drives the PLL into lock with the desired PVR voltage.
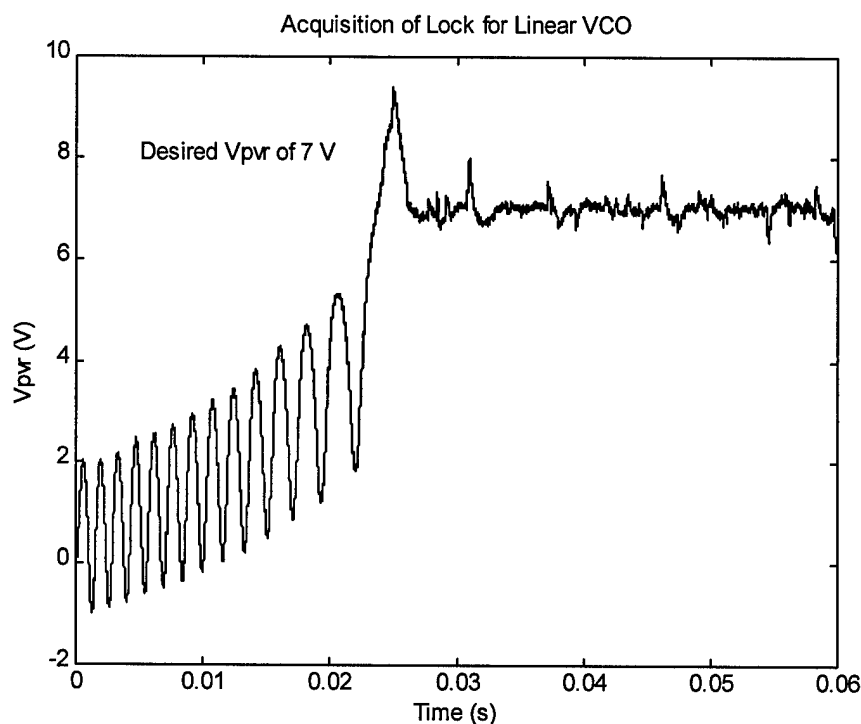
Figure 4.2. Acquisition of Lock for Linear VCO

4.2.1.2 Nonlinear Simulations

The nonlinear simulations were performed similarly to the linear simulations described above. The unique difference is the use of the nonlinear electrostatic characteristic of the resonators. This loop was optimally designed to operate at the final bias voltage on the electrostatic characteristic. The performance at low voltages is degraded according the low gain provided by the VCO. This was observed in the nonlinear simulations below by a substantial increase in the time to lock onto the reference frequency.

The first simulation is performed with a desired PVR voltage of 5 V and is presented in Figure 4.3.

75
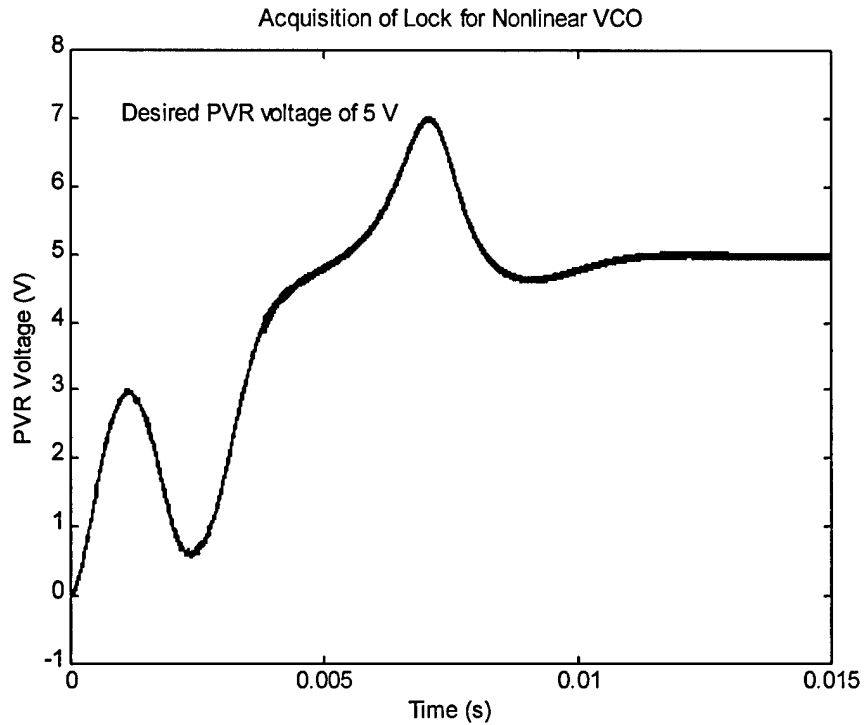
Figure 4.3. Acquisition of Lock for Nonlinear VCO

The low gain provided by the VCO at low bias voltages is lowering the bandwidth of the loop gain and causing the difference in frequency to appear larger initially. The acquisition time has approximately doubled from the linear case. As the voltage is further increased to 7 V, the time is again found to approximately double from the linear case.
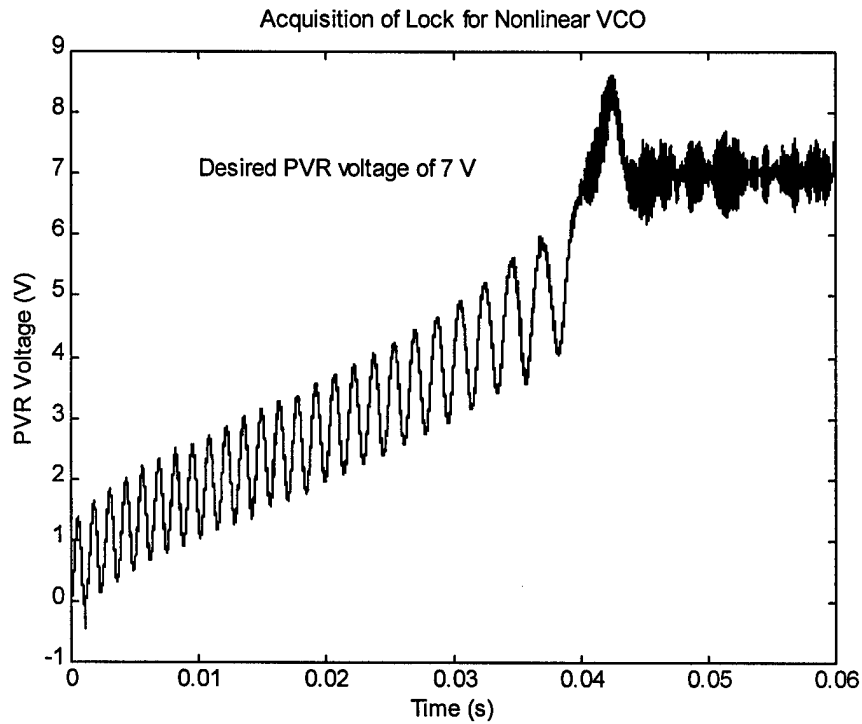
Figure 4.4. Acquisition of Lock for Nonlinear VCO

The many test cases for the linear and nonlinear VCO indicate that the nonlinear VCO associated with the resonator takes approximately twice as long to acquire lock compared to the linear case. In this application, acquisition speed is not a concern as long as it not more than a few seconds.

4.2.2 Oscillator Loop Simulations

The oscillator loop simulations contained the full dynamic model for the resonator, gain stage, low pass filter, hard limiter, and attenuator. The noise at the pre-amp was modeled with a single sided white noise power spectral density. All plots are aliased due to the high frequency and long time constants associated with the resonator. The first case set all initial conditions to zero and applied a 15 V bias for V_{pvr}. The position of the proof mass is shown below in Figure 4.5. In this start-up transient, the noise has little effect on the startup. The bias voltage causes an oscillation to

77

develop which effectively starts the resonator and brings it to steady state with the feedback network of the oscillator loop.
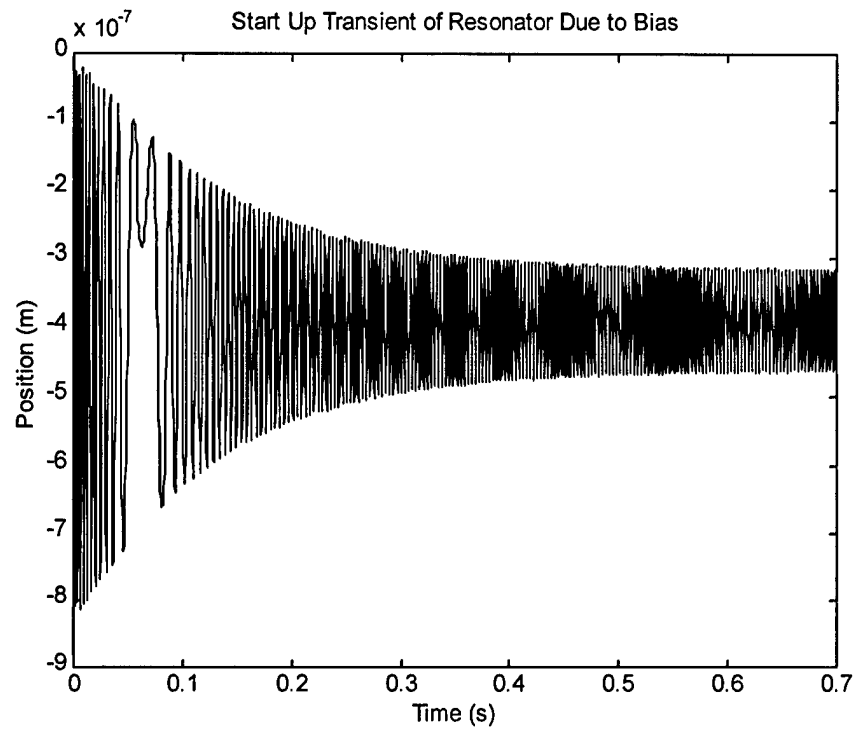
Figure 4.5. Aliased Start Up Transient of Resonator With Bias Applied

The phase plane is presented below and shows the oscillator progressing towards the limit cycle with positive damping.
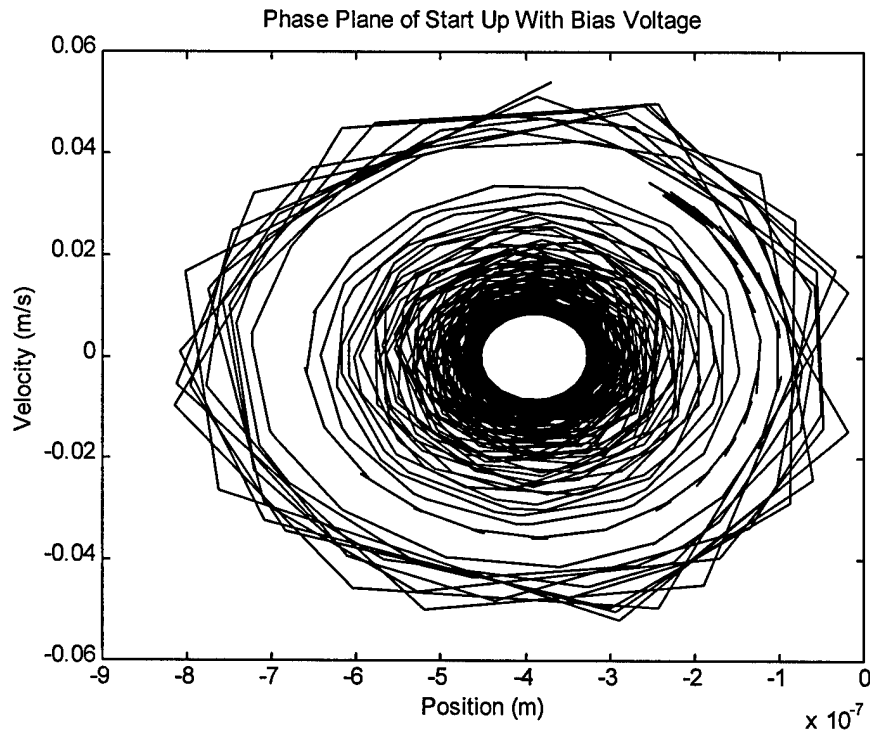
Figure 4.6. Phase Plane of Start of With Bias Voltage

In the second simulation, it is assumed that the bias voltage of 15 V has been applied and steady state has resulted with a constant displacement and zero velocity. The oscillator loop is then closed with only preamplifier noise to drive the loop.

x 10⁻⁸ Startup Transient of Oscillator Loop Due to Preamplifier Noise
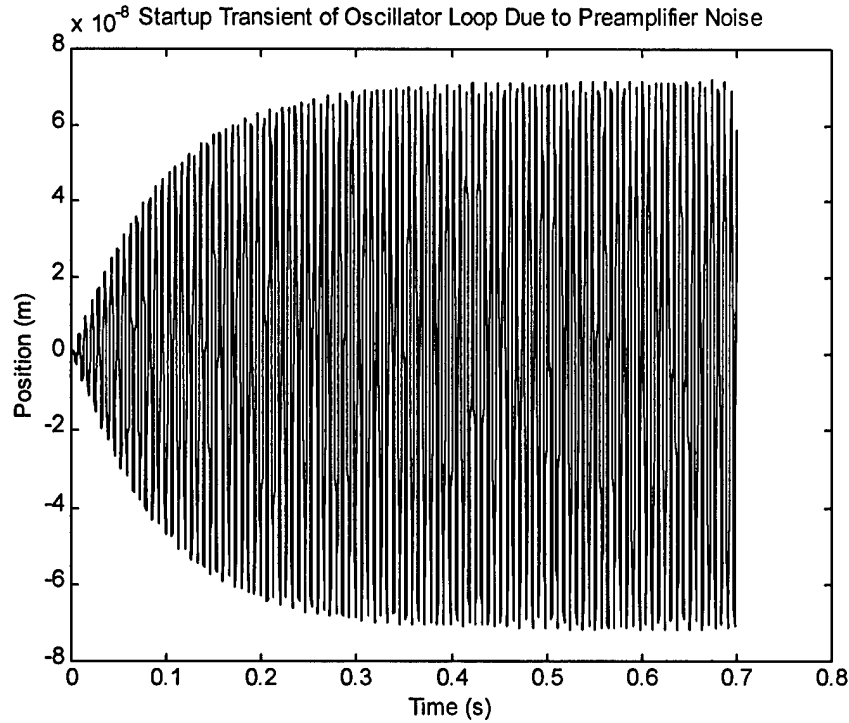
Figure 4.7. Aliased Startup Transient due to Preamplifier Noise

The signal path begins with the white noise at the preamplifier. This is amplified and put through the high pass and low pass filter. The signal is then applied to the hard limiter. The attenuated signal is placed on the force electrodes. The high Q, bandpass characteristic of the sense axis amplifies the frequency components at the eigenfrequency and the plates start to oscillate. The start up transient is a smooth transition to the full amplitude oscillation at the resonant frequency. The phase plane plot shows the approach to the limit cycle of the oscillator loop.
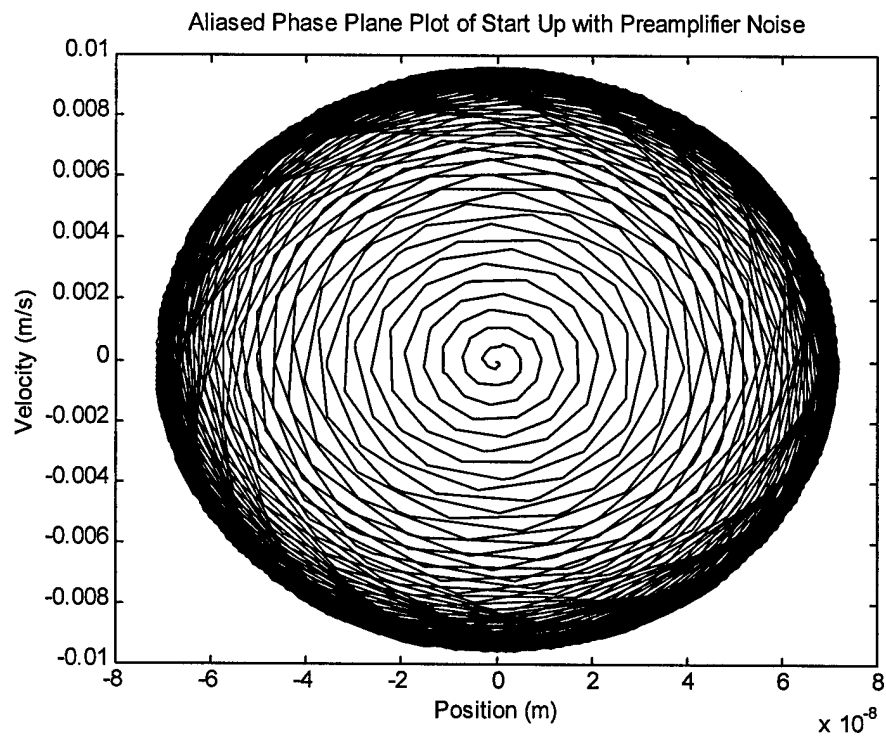
Figure 4.8. Phase Plane of Start-up Transient with Preamplifier Noise

81

Chapter 5

SYSTEM REQUIREMENTS

5. Overview

The extensive modeling developed for the PVR is used to construct an error model that demonstrates the viability of the PVR. The error model quantifies the effect of parameter perturbations on the voltage stability and provides the necessary criteria to develop a baseline design with optimal performance characteristics. The prototype design parameters are used throughout the analysis followed by the optimizations that produce the baseline design. The current prototype device cannot achieve 0.4 ppm voltage stability without an amplitude control loop because the pressure cannot be held to the stability requirements. The optimal design satisfies the requirement without the use of an AGC. The addition of an AGC would increase the performance of both designs well beyond the desired 0.4 ppm voltage stability. The goals of this chapter are to understand how the PVR model impacts the performance of the device, construct an error model, and develop the baseline design.

5.1 Voltage Stability

The single desired requirement for the PVR is a total voltage stability σ_V/V of 0.4 parts per million (ppm). The micromechanical resonator is utilized as a voltage controlled oscillator because its output frequency is dependent upon the input bias voltage. Due to this transfer characteristic, the voltage stability required for the PVR translates directly into a stability criterion for the oscillation frequency.

The oscillation frequency of the device is a function of a number of parameters including stiffness nonlinearity from the cubic electrical spring term, thermal variations, damping and pressure, contact potential, the time dependent probe voltages, and the feedthrough discussed in

section 2.4. Each of these quantities exerts an effect on the resonant frequency. Assuming the fluctuations in the individual measurements are uncorrelated, there will be no covariance terms and the total frequency variance will simply be the sum of the individual variance terms. The effects from each parameter will be examined in order to determine the overall effect on the frequency stability. The analysis uses differential notation($d\omega$) and statistical notation(σ_ω) interchangeably because some parameters are modeled as deterministic while others are modeled as random variables.

5.2 Frequency Stability

The required frequency stability to meet the 0.4 ppm voltage stability is an important parameter of device performance. The key to good voltage stability is operation on the steep slope of the electrostatic characteristic shown in Figure 2.4 where the frequency sensitivity to changes in the PVR voltage is large. Operating on this point of the transfer characteristic will allow greater frequency variations for a specified voltage stability criterion. Snapdown is possible as the bias voltage is increased. The device cannot operate too close to the snapdown voltage shown in Figure 2.4.

Consider the frequency stability that is required by the PVR for a desired voltage stability. In this application, the VCO is highly nonlinear with an analytical relationship relating the resonant frequency to the precision voltage reference applied to the VCO that is closely approximated with the following equation using Equation 2.2.10.

$$\omega_n = \sqrt{\frac{k_{ym} - \gamma \frac{\varepsilon_0 A}{Y_0^3} V_{pvr}^2}{m}} \qquad (5.2.1)$$

where,

ω_n = the nominal resonant frequency

83

k_{ym} = the y axis cubic mechanical stiffness,

m = mass of the proof mass

γ = fringing coefficient for the capacitance

Y_0 = nominal gap between the proof mass and bottom electrodes

k_y = linear spring term that includes mechanical and electrical parts

A = parallel plate area that the voltage V_{pvr} is applied

For the purposes of the error analysis throughout this chapter, the functions will be considered to be an exact representation of the behavior in order to propagate the errors. Using the error propagation equation, the relative uncertainty or stability in the oscillation frequency is given by

$$\frac{\sigma_\omega}{\omega} = \frac{\sigma_V}{V_{pvr}} \frac{V_{pvr}^2}{\omega^2} \left(\frac{\varepsilon_0 A}{m Y_0^3} \right) \qquad (5.2.2)$$

Assuming a constant voltage stability of 0.4 ppm is desired, the necessary angular frequency stability appears to rise according to the square of the PVR voltage. However, as the bias voltage is increased, the proof mass moves downward and the nominal gap is decreased. The figure below shows the relationship of the allowable frequency instability with increasing bias voltage given the 0.4 ppm voltage stability. As the PVR voltage is increased past 10 V, substantial gains in frequency stability are achieved.

Allowable σ_w/w (ppm)
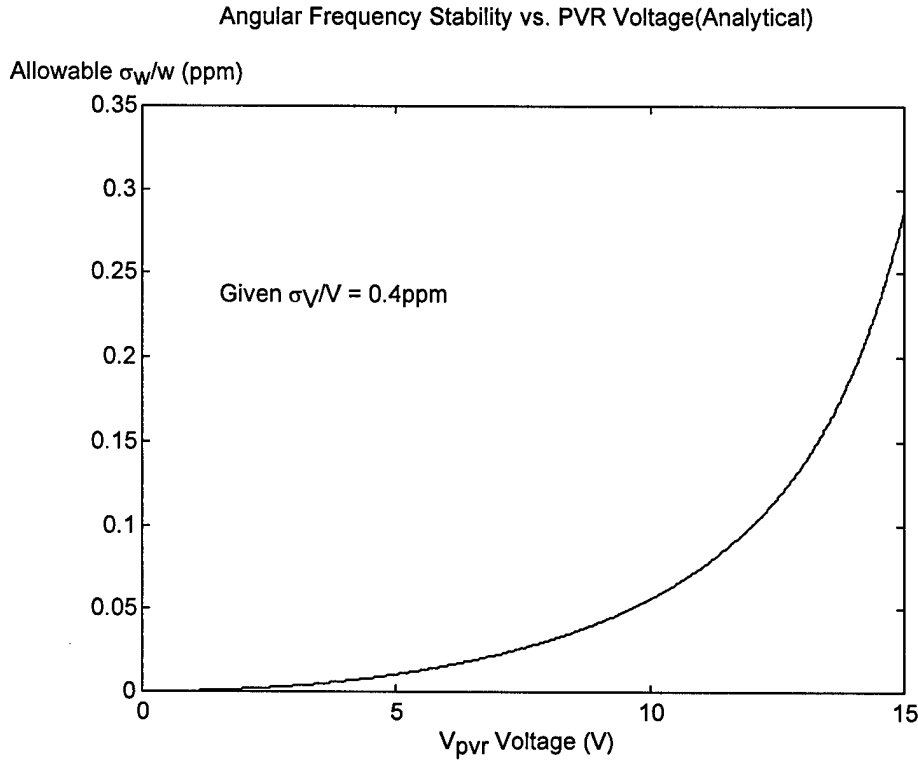
Figure 5.1. Angular Frequency Stability

Using the prototype design parameters with a PVR voltage of 15 V, the oscillation frequency is approximately 20 kHz compared to an oscillation frequency of 26.8 kHz with zero bias. The corresponding frequency stability is 0.29 ppm as shown in Figure 5.1.

The frequency stability can also be estimated from experimental data. The electrostatic data presented in Figure 2.3 only ranges from -5 V to +5 V. The decrease in nominal gap discussed above will cause the dispersion curve to bend downward more steeply as the voltage is increased. Therefore, the previous estimate is more accurate. This estimate is used to compare and confirm the previous estimate in the range of 5V. The data presented in the electrostatic characteristic in Figure 1.4 is fit with a second order polynomial of the form

$$\omega = c_0 + c_1 V_{pvr} + c_2 V_{pvr}^2 \qquad (5.2.3)$$

85

Again , the error in angular frequency due to the error in the PVR voltage is given by

$$\frac{\sigma_\omega}{\omega} = \frac{\sigma_V}{V}\frac{V}{\omega}(c_1 + 2c_2 V) \qquad (5.2.4)$$

Where the term in parenthesis is simply the slope of the electrostatic characteristic at the voltage reference. Using the parameters from the unit tested in Figure 1.4, and operating at the same point used above, the frequency stability is given by 0.13 ppm which agrees within an order of magnitude with the analytical results. Figure 5.2 shows the predicted frequency stability as a function PVR voltage from the test data. Within the range of 5 V, the stability agrees closely with the analytical model.
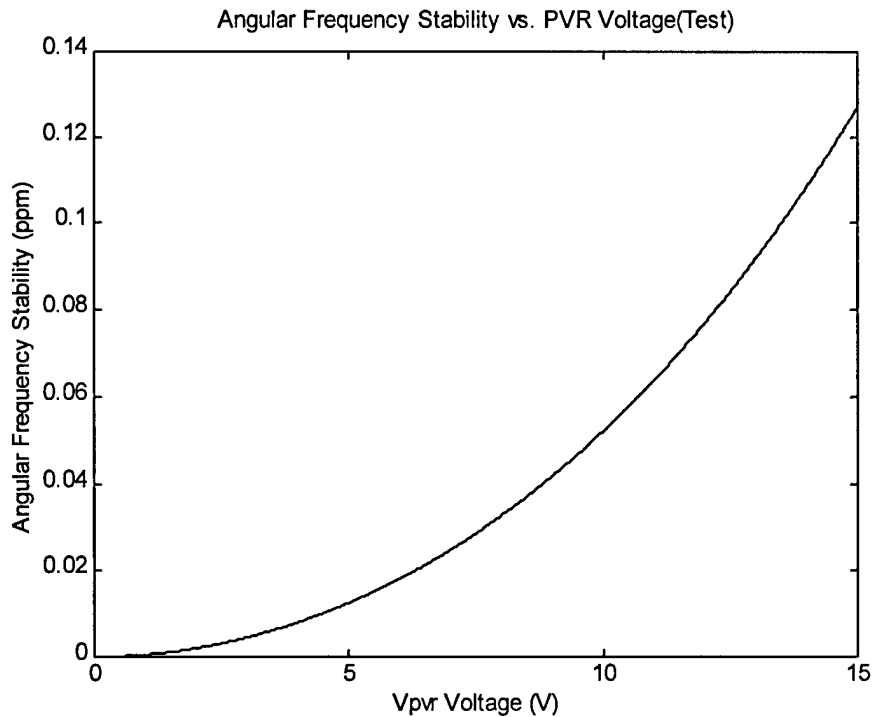
Figure 5.2. Angular Frequency Stability (Test Results)

5.3 Amplitude of Oscillation

The frequency stability translates into a required amplitude stability requirement. The electrostatic force produces a nonlinear cubic spring term. The cubic term is linearized using describing functions. The linearization demonstrates that this term causes the frequency to become dependent upon the amplitude of the oscillation. The frequency dependence is derived in the analysis of the Duffing Equation in Chapter 2 and the state space model of the resonator in Chapter 3. In Equation 3.2.4, the shift in nondimensional resonant frequency as a function of amplitude is shown to be

$$\tilde{\omega}_r = \sqrt{1 + \frac{3}{4}\frac{k_{y3e}}{k_y}A^2} \qquad (5.3.1)$$

where,

$\tilde{\omega}_r = \omega_r/\omega_n$ = nondimensional resonant frequency

k_{y3e} = the y axis cubic spring term due to the electrostatic force,

k_y = linear spring term that includes mechanical and electrical parts

A = steady state oscillation amplitude

The expression for the resonant frequency is normalized to the resonant frequency when the third order term is discarded, ω_n. The relative error or stability in the resonant frequency due to the relative error in amplitude is given by

$$\frac{\sigma_{\omega_r}}{\omega_r} = \frac{\sigma_A}{A}\frac{3k_{y3e}}{4k_y}A^2\frac{1}{\tilde{\omega}_r^2} \qquad (5.3.2)$$

87

The frequency sensitivity to variations in amplitude ($\dfrac{\dfrac{\sigma_{\omega_r}}{\omega_r}}{\dfrac{\sigma_A}{A}}$) is optimized by making the oscillation amplitude small with regard to the nominal gap distance. Additionally, the normalized resonant frequency on the right side in the above equation will approximately equal unity as the cubic nonlinearity only slightly shifts the frequency.

Assume the device is operated with the prototype design parameters. The nondimensional shift in resonant frequency due to the cubic term is 1.52e-3 as shown in Appendix A. The amplitude stability required to maintain the 0.3 ppm angular frequency stability is 98 ppm, representing a significant level of control. This requirement can be reduced several orders of magnitude by reducing the quality factor, reducing the sense plate area, decreasing the mass of the proof mass, or lowering the unbiased gap distance. The only method of decreasing the frequency sensitivity to amplitude variations without reducing the voltage stability is by increasing the pressure inside the sealed resonator or reducing the probe voltage.

5.3.1 Pressure and damping

The pressure in the sealed resonator packages is found to range between 1-5 mTorr [3]. In this regime, known as the molecular regime, the primary damping mechanism is the "independent collisions of non-interacting air molecules with the moving surface" [2] of the proof mass. The mechanical damping associated with the structure is negligible. In this region, the quality factor is inversely related to the pressure. Damping is also inversely related to the quality factor which means pressure and damping are linearly related in this regime.

The physical effects of a pressure change in the resonator package dictates how the frequency changes. As the seal degrades and pressure increases, the quality factor of the resonator will decrease. The decreased quality factor reduces the amplitude to force ratio. The two important cases are with and without an amplitude control loop.

Without an amplitude control loop, the oscillator will remain locked onto the resonant frequency with an increase in pressure; however the amplitude will decrease. If the change in amplitude does not meet the amplitude requirement in section 5.3 , the PVR loses its stability. The frequency sensitivity to amplitude variations is

$$\frac{\dfrac{\sigma_{\omega_r}}{\omega_r}}{\dfrac{\sigma_A}{A}} = \frac{3k_{y3e}}{4k_y} A^2 \frac{1}{\tilde{\omega}_r^2} \qquad (5.3.3)$$

The statistical descriptions are more appropriately described with differential changes. The frequency stability is rewritten using Equation 5.3.4 and explicitly includes the pressure change that causes the amplitude change.

$$\frac{d\omega_r}{\omega_r} = \left(\frac{3k_{y3e}}{4k_y} A^2 \frac{1}{\tilde{\omega}_r^2} \right) \frac{dA}{A} \frac{dP}{dQ} \frac{dQ}{dP} \qquad (5.3.4)$$

The most convenient way of simulating the frequency shift from a pressure change is using the appropriate quality factor shift. The amplitude and quality factor are known to be linearly related from Equation 2.2.19. This indicates that the relative shift in amplitude equals the relative shift in quality factor. The frequency sensitivity to changes in quality factor (pressure) is written in the following useful form

$$\frac{\dfrac{d\omega_r}{\omega_r}}{\dfrac{dQ}{Q}} = \left(\frac{3k_{y3e}}{4k_y} A^2 \frac{1}{\tilde{\omega}_r^2} \right) \qquad (5.3.5)$$

Thus, the frequency sensitivity to a quality factor shift is identical to that of amplitude variations. The relative uncertainty in the quality factor is equal to the negative relative uncertainty in the

pressure because these two quantities are inversely related. This indicates that the maximum allowed shift in pressure that will meet the frequency stability requirement is 98 ppm.

Simulations were constructed to confirm the accuracy given by the first order design study value of 98 ppm pressure stability. The long term magnitude of pressure leakage on the sealed resonator units is not known. For the simulations, the pressure and quality factor are allowed to change according to the values listed in Table 5.1.

Table 5.1. Frequency Sensitivity Due to Quality Factor Shift

Quality Factor Change	Baseline	1%	0.1%	0.01%
Resonant Frequency (rad/s)	133884.675	133876.272	133884.085	133884.729
Frequency Shift (ppm)	0	62.8	4.4	0.40

For the simulations in Table 5.1, the prototype design parameters were used. The zero bias quality factor and resonant frequency were 19190 and 26829 Hz respectively. The simulation uses the full differential equation describing the proof mass motion, the oscillator loop components, and includes an artificial phase locked loop with 3 state variables as a convenient method for measuring the frequency of the oscillator as the quality factor changed due to pressure reductions. The simulation set the initial position of the proof mass so the system reached steady state rapidly.

The results indicate that at the operating voltages chosen for the prototype design, it is necessary to hold the pressure in the package to at least 0.01% over the lifetime of the device. This matches the expected 98 ppm calculated for the amplitude stability and the first order design will be used for any further estimates. This requirement on the pressure is much too stringent for the

current packaging and dictates a design change to achieve the required frequency stability of 0.3 ppm.

The simplest design change requires the addition of an automatic gain control loop which adjusts the magnitude of the probe voltage. With an amplitude control loop, the AGC loop will adjust the magnitude of the square wave in order to maintain a constant amplitude. The effects of changing probe voltages are examined in the following section and found to have a negligible effect on the resonant frequency over any realistic range. The implementation of an AGC loop will certainly boost performance but was not designed in this thesis.

The next design option is to reduce the frequency sensitivity to amplitude variations, allowing larger changes in the amplitude and pressure. The physical adjustments that achieve this larger scale factor are described in section 5.3. These changes are made in the optimized baseline design.

5.3.2 Drive Voltages

The voltage applied to the force plates includes a bias identical to the bias applied to the sense plate and a probe voltage. The probe voltage is a square wave with a fixed magnitude. The effect of changes in the magnitude of the probe voltage are important as there will be considerable switching noise associated with these signals.

The first effect of changes in the probe voltage is the resultant DC bias from squaring the electrode voltage. The first order design calculations provide a convenient estimate of the impact. With the prototype design and 15 V applied to bias the force and sense electrodes, a 1 mV drive voltage moves the proof masses 10% of the nominal gap. The DC force and stiffness generated by the drive signal is found to be 1.5e-10 that of the bias signal as shown in Appendix A. This confirms that the probe voltages can change dramatically with no significant direct effect on the 0.4 ppm voltage stability.

The probe voltage also affects the oscillation frequency indirectly through the oscillation amplitude. The probe voltage is directly proportional to the amplitude of oscillation to first order. This indicates the probe voltage must be held to the same stability requirements as the amplitude. For the prototype design, the probe voltage stability must be 98 ppm. A simple voltage divider modeled with typical thermal noise will satisfy this stability requirement.

Consider a resistive divider with a 5 V_{pp} square wave at the input. This models the square wave at the output of the hard limiter in the oscillator loop. The root mean square value of the Gaussian thermal voltage noise for each resistor is given by V_{rms}.
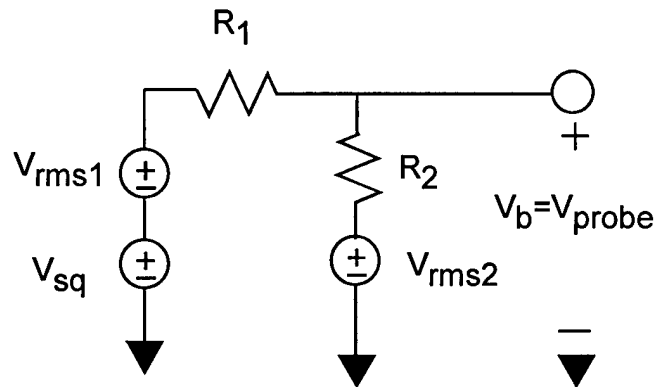
Figure 5.3. Voltage Divider for Probe Voltage

The thermal noise spectral density for R_1=2.5kΩ resistor is 40e-18 V^2/Hz. The bandwidth of the oscillator loop is approximately one decade greater than the resonant frequency or 250 kHz. Thus, the RMS voltage for R_1 is 3.16 uV. Both voltage sources are attenuated by the resistor pair so the voltage stability is 1.26 ppm which meets the required 98 ppm. For a probe voltage amplitude of 1mV, the RMS voltage for R_2=1Ω is 63nV which dominates the noise from R_1 and gives 63ppm stability.

5.4 Thermal Effects

Thermal effects are an important consideration in the design of any PVR and dictate the thermal control required for a device. In order to estimate the performance that is required from the

micromechanical resonator, typical quartz oscillators are examined first. When the quartz flexures are oriented with regard to the crystallographic axes, the linear thermal variation of the resonant frequency is zero and the frequency sensitivity is second order at -0.035 ppm/°C^2 where the minimum occurs near room temperature [16]. Assuming 10°C from the minimum, the linear sensitivity is -0.7 ppm/°C. The thermal stability of the silicon on glass resonators consist of two effects: mechanical changes in the structure and a contact potential at the bond points.

5.4.1 Mechanical Thermal Effects

By careful design, the frequency sensitivity to thermal variations is 0.5 ppm/°C. In separate references to thermal insensitive micromechanical resonators, ppm/°C sensitivity was achieved [7,11]. In order to achieve the required 0.3 ppm frequency stability, temperature control of 0.6°C is required. Temperature control of 0.01°C is achieved in current strategic systems at Draper Laboratories [17]. The thermal control needed for the thermally insensitive PVR is easily achieved.

5.4.2 Contact Potential

A contact potential results from the mismatch in work functions between two metals and results in one metal having a higher Fermi level. Consequently, the electrons from the metal with the higher Fermi level spill into the metal with a lower level until the filled energy levels in both are equal. The result is that one side becomes positively charged while the other becomes negatively charged and a potential difference of $(w_b-w_a)/e$ exists between the two metals, where e is the charge of a single electron. The terms w_a and w_b represent the work functions of both metals.

In the resonator model, the contact potential is modeled at the proof mass/substrate junction. The proof masses contact the substrate through a silicon/gold contact shown in Figure 1.3. The contact potential puts the proof masses at a non-zero potential and can be conveniently modeled an additional voltage source in series with the electrode voltages. A simplified model for the pre-amplifier that focuses on the contact potential is shown below.

93
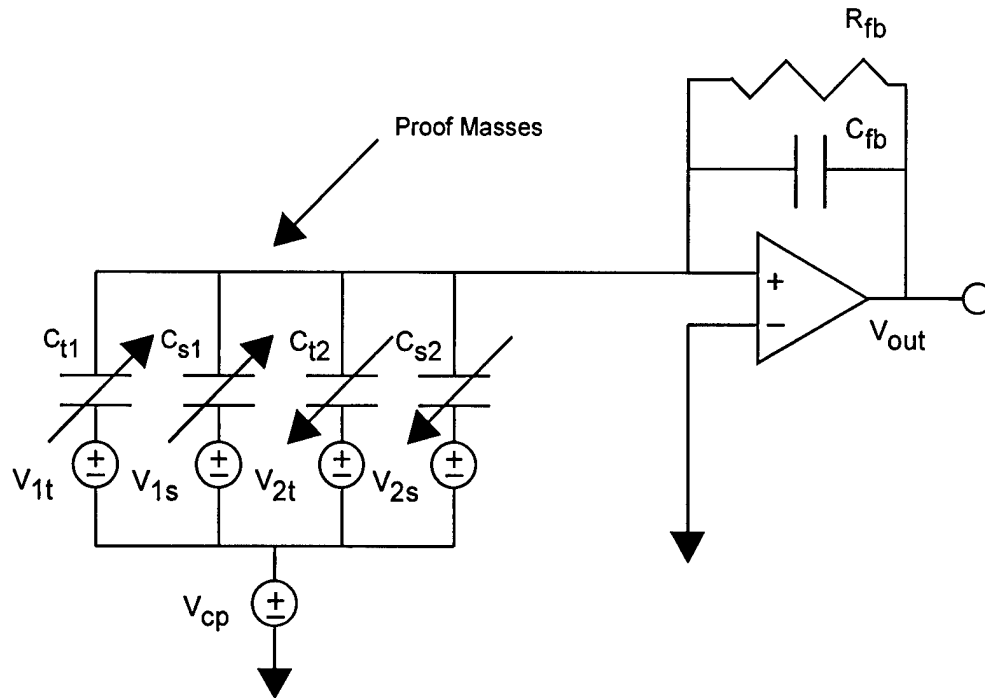
Figure 5.4. Contact Potential Model

The contact potential is measured in the range of -0.3 to 0.3 V with a temperature dependence of 1 mV/°C. The initial effect of the contact potential is the generation of a DC voltage term and error term as derived in Equation 2.4.12. The α terms could equally account for a bias voltage mismatch as well as the area mismatch. The electronics are designed to null the effect of this mismatch at the nominal operating temperature.

As the temperature changes, a problems exists because the electronics cannot be constantly tuned for a difference mismatch in bias voltage. The DC voltage term and higher harmonic error term should be filtered by the high and low pass at the output of the preamplifier. However, the frequency will shift. The change in temperature produces a change in the contact potential. On one plate, the voltage will increase while decreasing on the other due to the differential biasing. To first, order, the first-order net stiffness coefficients are proportional to the capacitance and the squared voltage.

$$k_{y1} \propto (V_{pvr} + \Delta V_{cp})^2 C_1$$
$$k_{y2} \propto (V_{pvr} - \Delta V_{cp})^2 C_2$$

(5.4.1)

The effect of the temperature shift will be a differential shift in the spring terms. This is how the contact potential is modeled in the analysis below.

The analysis of the contact potential indicates that a shift in frequency of 0.009 ppm results from using temperature control of 0.6°C. In the coupled model presented in Chapter 2, the out-of-phase mode frequency is unaffected by a differential shift in the stiffness coefficients so the frequency will not shift as the contact potential changes. This model is slightly altered to make an estimate of the frequency shift from the contact potential. A simple coupled oscillator model is shown in the figure below where the out-phase-mode is dependent on the coupling.
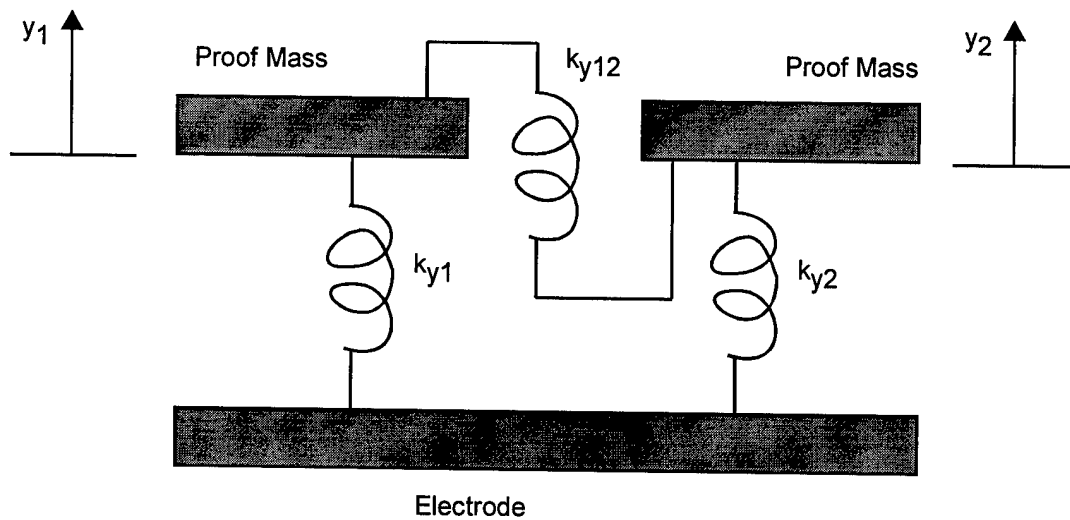
Figure 5.5. Coupled Oscillator Model for Contact Potential

The kinetic and potential energy for the system can be written

95

$$T = \frac{1}{2}m\dot{y}_1^2 + \frac{1}{2}m\dot{y}_2^2$$
$$U = \frac{1}{2}k_{y1}y_1^2 + \frac{1}{2}k_{y2}y_2^2 + \frac{1}{2}k_{y12}(y_1 - y_2)^2$$

(5.4.2)

These two equations can be used to write the generalized mass and stiffness matrices [9]. The eigenfrequencies are then calculated with the following determinant:

$$\begin{vmatrix} k_{y1} + k_{y12} - m\omega^2 & -k_{y12} \\ -k_{y12} & k_{y2} + k_{y12} - m\omega^2 \end{vmatrix}$$

(5.4.3)

All of the quantities are known except for the coupling spring term. The separation in modal frequencies is known to vary by approximately 3-5%. This separation in the modal frequencies can be modeled in the coupling stiffness term or a difference in spring terms resulting from mismatched capacitance on the two resonators.

Modeling the separation in the coupling term produces an estimate of its value. The stiffness coefficient k_{y12} was adjusted to 2.5 N/m until the modal frequencies were separated by 4.87%. Next, the temperature control of 0.6°C causes a differential shift of 0.6 mV on each plate. This results in a 80 ppm shift in the stiffness coefficients. This differential shift was applied to the stiffness coefficients and the out-of-phase mode frequency shift was found to be 0.009 ppm. This is a negligible shift in the oscillation frequency.

Next, the initial separation in the model frequencies was modeled directly with a 5% difference in the linear stiffness coefficients and the coupling term was 2.5 N/m. The initial difference in modal frequencies is 5.4%. The shift in frequency for 0.6°C temperature control exceeds the 0.3 ppm requirement. The limit of 0.01°C temperature control produces a frequency shift of 0.016 ppm. The temperature control for the contact potential shift is the limiting factor in thermal control. The current technology provides the necessary temperature control to attain a minimum shift of 0.016 ppm..

5.5 Interrupt Resistance and Radiation Hardness

In addition to the voltage stability and related control measures, the PVR must be interrupt resistant. A micromechanical VCO with a resonant frequency based upon a mechanical standard will be capable of operating through short interrupts. In a linear second order resonator with a quality factor much greater than unity, the time required for the amplitude to fall by a factor of e is approximately Q/π cycles of oscillation [4]. For the resonators, typical quality factors are around 20e3 and a resonant frequency of 25kHz. The number of cycles required for the amplitude to fall by a factor e is approximately 6.4e3 cycles or 0.25 s which is close to the results obtained in the start-up transient simulations in Chapter 4.

A voltage reference based on a mechanical standard should also be radiation hard. The radiation effects on silicon and glass are a separate study and the exact relationship between the radiation and the frequency of oscillation is not known.

5.6 Baseline Design and Optimal Performance of Micromechanical PVR

The baseline design is given in appendix A. The primary changes to the prototype design include reduced probe voltage, reduced Q factor, increased mass, and decreased plate area. The frequency sensitivity to amplitude variations is reduced from 3.07e-3 to 3.57e-5. This improves the frequency sensitivity to probe voltage and pressure changes. With this improvement, the baseline design meets the 0.4 ppm voltage stability without an AGC loop.

In general, the performance of the PVR is increased by decreasing the amplitude of oscillation. This minimizes the nonlinear effects which couple the amplitude to the frequency. Theoretically, the lower limit of resolution is set by the noise at the preamplifier. Several simulations were performed to study the effects of preamplifier noise on frequency noise[15]. The preamplifier noise was 10^{-15} V^2/Hz with a resonant frequency of 20kHz and 10um drive amplitude. The quality factor of the device was 10^4. The change in frequency was found as a function of both oscillation amplitude magnitude and phase. When the preamplifier noise at the fundamental resonance is in phase with the with the position signal at the output of the preamplifier, the

97

magnitude varies. When the signals are in quadrature, the phase varies. The simulation determined the amplitude noise to be $0.001/\sqrt{\tilde{Hz}}$. Multiplying this value by the change in normalized frequency with normalized amplitude yields the rate noise of 1.9e-5 $rad/\tilde{s}/\sqrt{\tilde{Hz}}$ which is close to the value of 1.3e-5 $rad/\tilde{s}/\sqrt{\tilde{Hz}}$ found from the simulated rate noise. The normalized rate noise is $0.0046 rad/s/\sqrt{Hz}$. The frequency sensitivity to magnitude is much larger than the sensitivity to phase so the phase component is negligible. Given a loop bandwidth of 200Hz, the root mean square of the frequency noise is given by 0.065 ppm. This simulation was performed under similar conditions that the PVR operates and provides a rough estimate for theoretical limit of the PVR.

HARDWARE

6. Overview

A classic feedback control analysis is performed to design the PLL loop components values. This completes the prototype design. The prototype PVR device was built at Draper Laboratories. The oscillator loop is fully functioning and self starts with the preamplifier noise. The PLL loop locks onto the desired PVR voltage. The goal of this chapter is to present the classic control design analysis for the PLL loop, explain the device schematic, and discuss the testing of the fully functional PVR prototype.

6.1 Classical Feedback Control Design

The block diagram is shown in its final form for the two proof mass resonator in Figure 6.1. The inverter in the PLL feedback path generates the inverted bias voltage for the second proof mass, resulting in out of phase forcing and differential sensing.
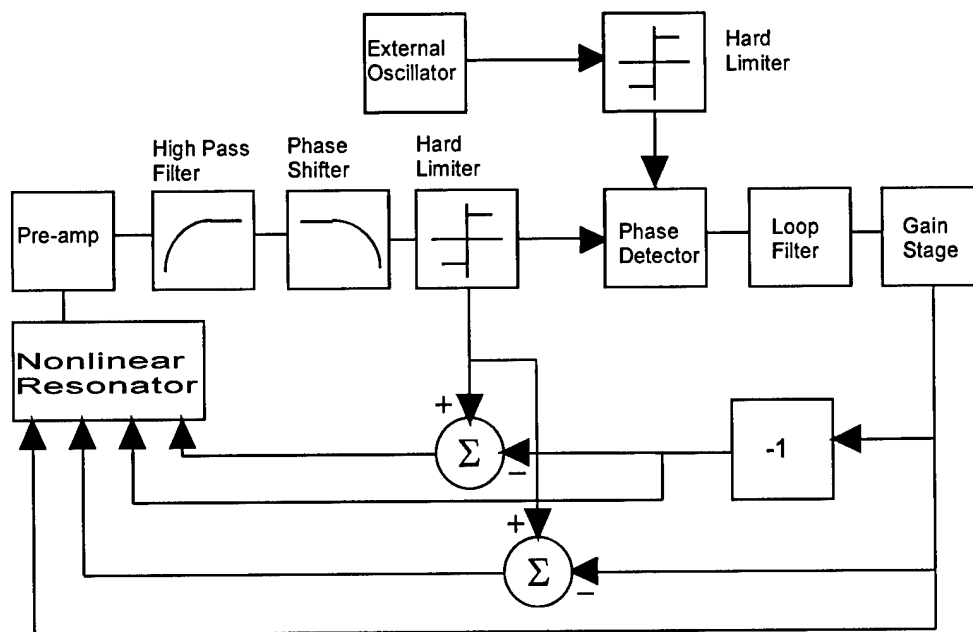
Figure 6.1. Block Diagram of Oscillator and Phase Locked Loops

The design of the electronics for the PLL is simplified if the loop is linearized and redrawn as shown in Figure 6.2. In this form, the input signal is the reference phase which is compared with the phase of the VCO output. The error signal is then passed through a phase detector that produces a voltage proportional to the phase difference with a gain of K_D V/radian. This is sent through a loop filter that eliminates high frequency components. The transfer function for this filter is given by F(s). Finally, the signal is passed to a gain stage, A, that accounts for all the other gain in the loop. The output voltage is the precision voltage reference. This voltage is passed into the voltage controlled oscillator that converts the voltage to a frequency with a constant of proportionality, K_0 radians/s/V. Finally, an integrator is added to account for the transformation from frequency to phase. Figure 6.2 shows the loop in terms of the components transfer functions.
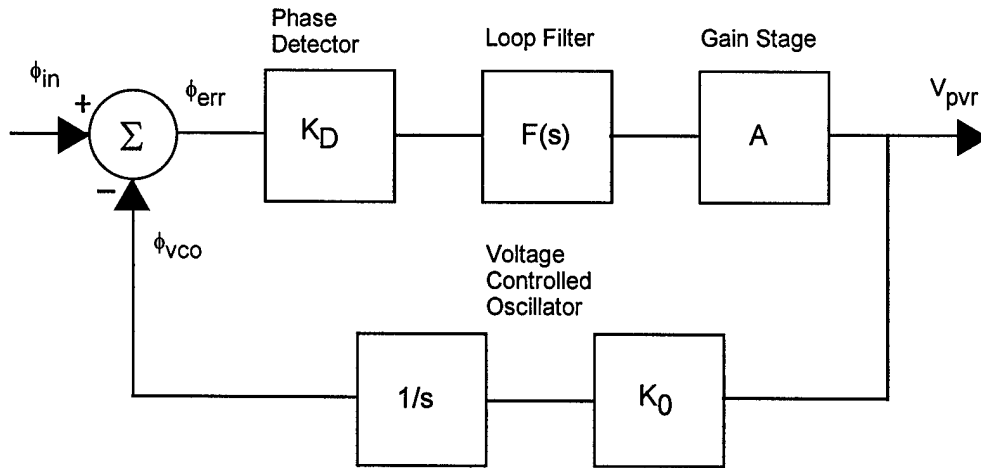
Figure 6.2. Simplified Block Diagram of Phase Locked Loop

In Figure 6.2, all of the complex feedback network has been eliminated. The resonator has been simplified to its incremental gain model. The value of K_0 is given by the slope at the bias point which is essentially the linearized movement up and down the curve at that point during the acquisition and tracking phases of lock.

The basic transfer function from input to output, in Figure 6.2, is given by

$$H_1(s) = \frac{V_{pvr}}{\phi_{ref}}(s) = \frac{sAK_DF(s)}{s + AK_DK_0F(s)}$$

(6.1.1)

In many situations, it is more convenient to examine the response of the PVR voltage in terms of changes in reference frequency. The input frequency can be expressed as the derivative of the phase.

$$\omega_{ref} = s\phi_{ref}$$

(6.1.2)

Substituting this into the above equation gives the following expression for the transfer function:

$$H_2(s) = \frac{V_{pvr}}{\omega_{ref}}(s) = \frac{AK_D F(s)}{s + AK_D K_0 F(s)} \qquad (6.1.3)$$

In this application, the input frequency is not modulated and is essentially constant in time so the bandwidth is not an important performance criteria. However, the bandwidth of the transfer function must be large enough to allow quick acquisition. Again, the acquisition time is not important; the loop must simply lock in a reasonable amount of time.

There are several options for the type of filter to be used. The simplest one is a first order passive RC filter. Unfortunately, the lock range and 3dB bandwidth of the loop cannot be set independently. Adding a zero to the low pass RC filter provides the flexibility of setting both these parameters independently [6]. However, an ideal integrator in the forward path reduces steady state errors and enhances performance by offering higher DC gain [5]. There are a number of other reasons to avoid passive filters that are offered in Gardner [5]. The filter used in the loop is a second order, low pass, active filter and is given by

$$F(s) = -\frac{K_L}{s}\left(\frac{s + \omega_2}{s + \omega_1}\right) \qquad (6.1.4)$$

This filter is known in servo theory as a proportional plus integral controller with recovery.

Substituting the loop filter expression into Equation 6.1.3, the transfer function for the loop can be written in the general second order form as:

$$H(s) = \frac{K_D K_L (s + w_2)}{s^3 + s^2 \omega_1 + s K_0 K_D K_L + K_0 K_D K_L w_2} \qquad (6.1.5)$$

and the loop gain is

$$L(s) = \frac{AK_0 K_D K_L (s + w_2)}{s^2 (s + \omega_1)} \qquad (6.1.6)$$

102

Next, the different values for all the constants in Figure 6.2 were calculated. This required choosing actual components for the loop and choosing an appropriate phase detector. The value of K_0 was found from the electrostatic characteristic in Figure 1.4 at the operating point. The filter chosen is described above. The phase detector consists of two edge-triggered, resettable D flip-flops with their D inputs connected to logic high. The outputs are connected to both resets through a logic AND gate. The constant of proportionality for the detector is $K_D = 5/(2\pi)$ V/rad where 5 volts is utilized as logic high. All remaining gain in the loop was lumped into the parameter A.

In designing this second order loop, general stability requirements on the loop gain were used. The crossover frequency is set two decades below the resonant frequency, $0.01\omega_n$. The lead and lag terms are separated by a factor of 6. Each is placed symmetrically on either side of the crossover frequency to provide for maximum phase at the crossover point. Finally, the loop gain is set to unity at the crossover frequency by adjusting K_L. After designing the controller, the components for each stage are designed to meet the specifications. The simulated bode plot for the closed loop, bode plot for the loop gain, and Nyquist plot are shown in Figure 6.3 through Figure 6.5.
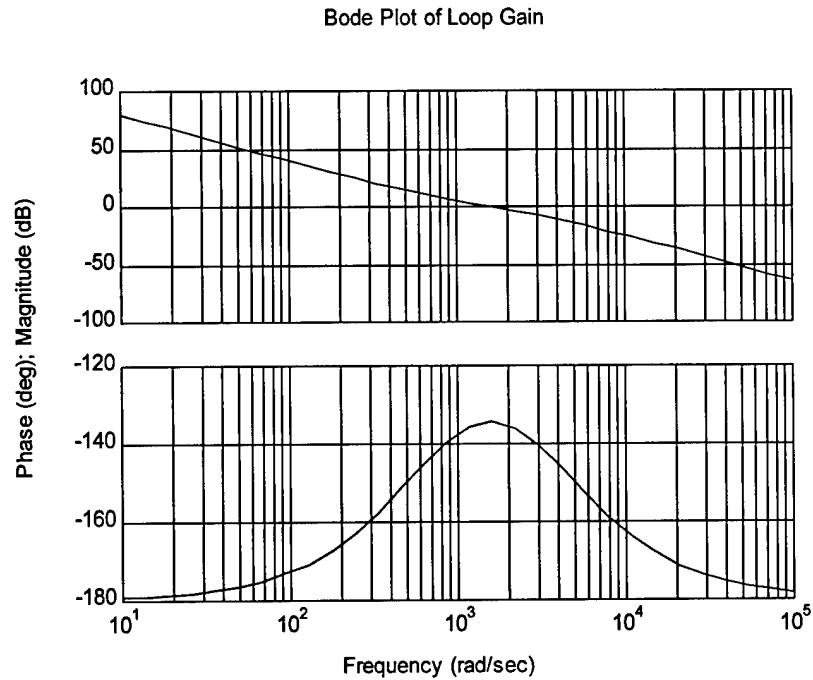
Figure 6.3. Simulated Bode Plot of Loop Gain
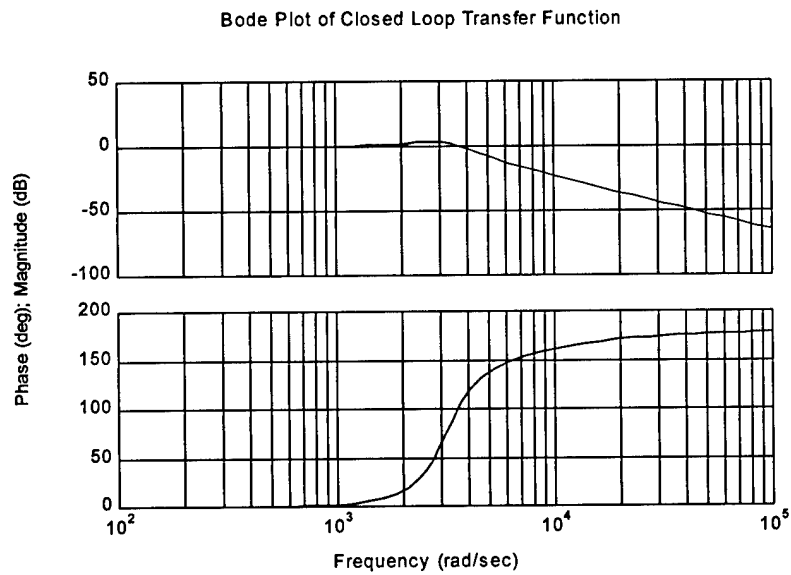
Figure 6.4. Simulated Bode Plot of Closed Loop Transfer Function

104
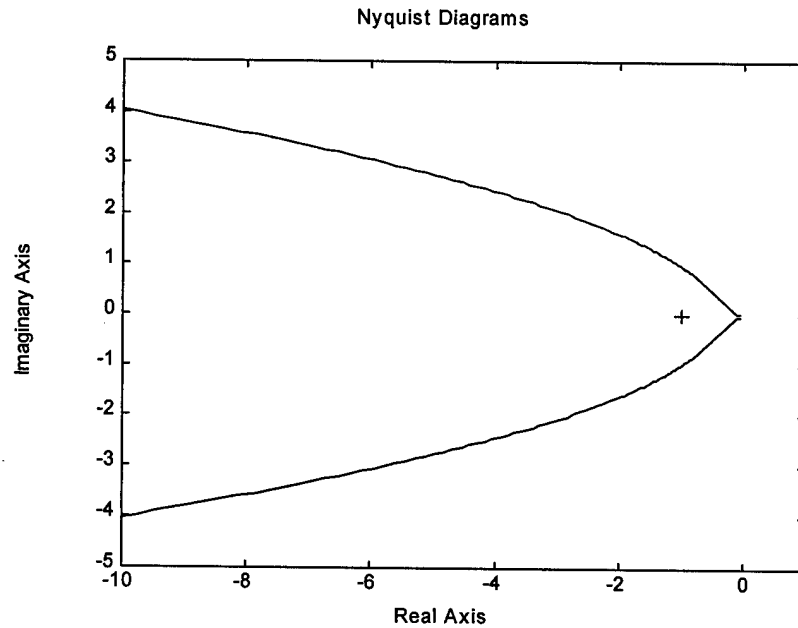
Figure 6.5. Simulated Nyquist Diagrams

The phase margin for the design is approximately 45° and linear stability of the phases locked loop is achieved with the design.

The performance of the PLL loop is relatively unimportant in this application. As long as the loop locks in a reasonable amount of time, the loop functions properly. Several performance characteristics are useful for testing the performance of the device. The velocity-error coefficient or DC loop gain of the PLL is an important parameter that affects the static phase error, hold-in range, and acquisition range. The PLL has a DC loop gain of

$$K_v = AK_0K_DF(0) \qquad\qquad (6.1.7)$$

The active filter has an integrator with an operational amplifier DC gain of A_o (~1e6). The large value for K_v optimizes many static and dynamic characteristics of the PLL. During the acquisition phase, it is important that the loop lock over a large bandwidth. The maximum difference in frequency for which the loop will lock without skipping cycles is given by [5]

$$\Delta\omega_H = \omega_n \qquad\qquad (6.1.8)$$

where

ω_n = loop gain bandwidth = 1500 rad/s

The maximum difference in frequency between the resonator and the reference which the loop will eventually lock itself is the pull-in frequency. For the active filter loop, the pull-in frequency is given by [5]

$$\Delta\omega_P = 2\sqrt{\varsigma\omega_n K_v} \qquad\qquad (6.1.9)$$

Once the loop is locked, it will hold-in lock for any changes in frequency around a bandwidth of [5]

$$\Delta\omega_H = \pm K_v \qquad\qquad (6.1.10)$$

Finally, the static phase error is the error resulting from a step change of frequency $\Delta\omega$ while the loop is locked is given by

$$\theta_v = \frac{\Delta\omega}{K_v} \qquad\qquad (6.1.11)$$

The large DC loop gain insures that any errors will be tracked out. The large value of K_v for the active filter loop minimizes the static phase error and increases the hold-in range and pull-in frequency. The values for the PLL loop agree well with the values seen in the PLL loop simulations.

6.2 Hardware Design and Testing

The hardware design went through an initial breadboard stage to confirm the operation of the electronics. After some minor changes, the final PVR design was built. The component level schematic diagram is shown in Appendix C.

The test station is shown in Figure 6.6 with the PVR device, oscilloscope, function generator, and DC power supplies.
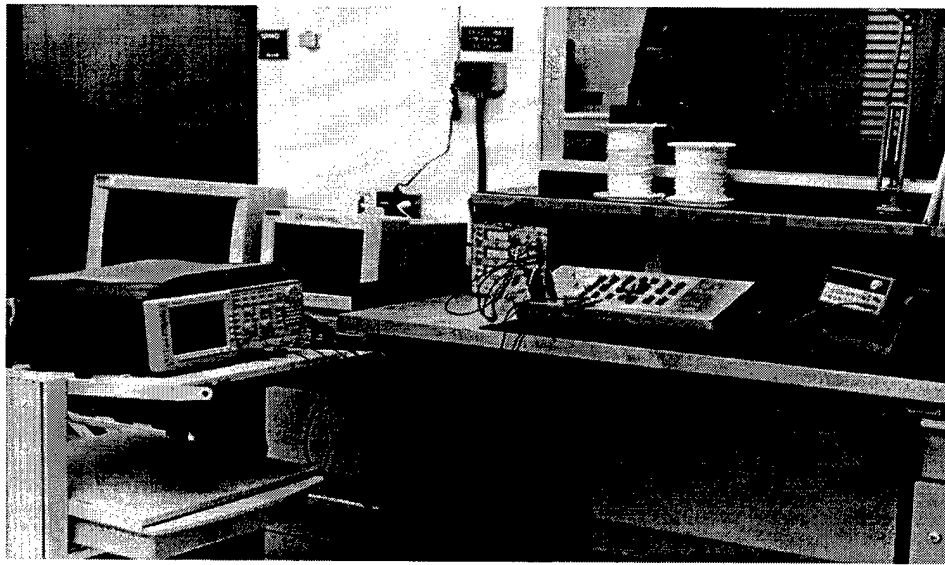
Figure 6.6. Testing Station

The following two figures provide a closer view of the PVR device and the chip carrier containing the sealed micromechanical resonator.
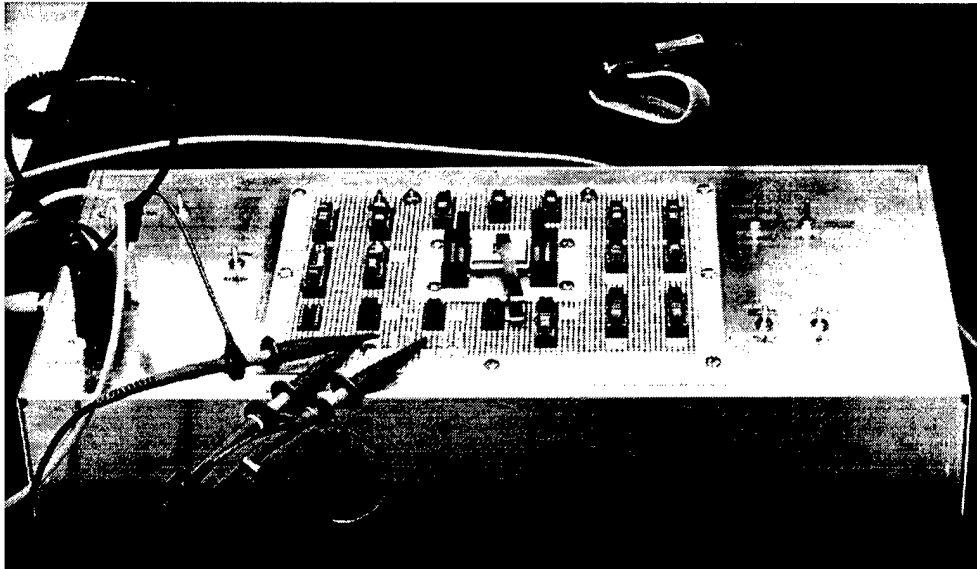
Figure 6.7. PVR Device
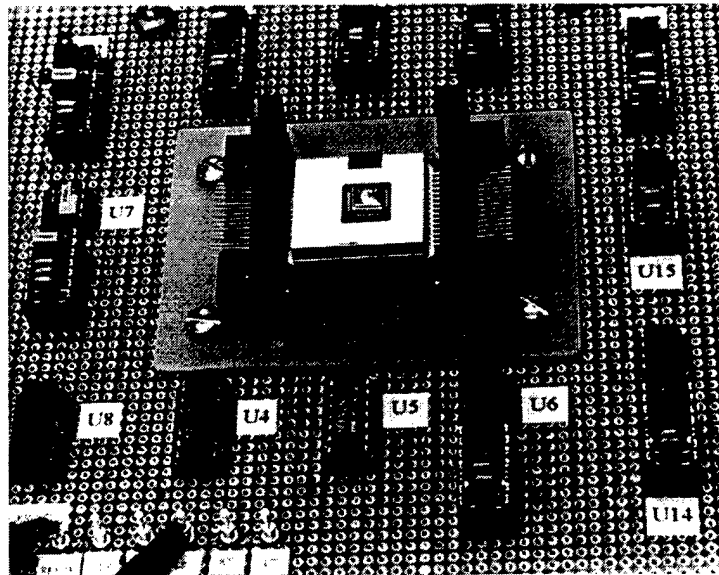
Figure 6.8. Chip Carrier and Packaged Micromechanical Resonators

The testing of the PVR remained at a basic level for this thesis. The oscillator loop was closed first and the self excitation of vertical axis oscillations was confirmed. The PLL loop was also closed and the PVR operation was confirmed.

The functioning prototype contains several minor changes from the prototype design. First, the integral plus proportional controller was removed due to stability problems. The instability was caused by not accounting for an integrator 1/s for the resonator. Secondly, a limiter circuit was added to the control voltage that limits the value from approximately 1V to 10V. The PVR voltage can currently be adjusted to any value within this range. The upper limit is simply extended to realize the prototype PVR voltage of 15V. The limiting was used to prevent the snapdown of additional units. The prototype corresponds exactly to the schematic in appendix C after accounting for these changes.

Chapter 7

CONCLUSION AND RECOMMENDATIONS

In this thesis, a precision voltage reference was analyzed, designed, and tested. After a brief introduction to the theory of micromechanical resonators, the basic dynamics of a parallel plate micromechanical resonator pair were developed along with the electrostatic actuation theory. Several options for biasing the PVR were offered and a simple scheme was chosen with in phase probe voltages. The model was simplified to describe the out-of-phase mode of the resonator pair. Following the dynamics, the model for sensing the resonator motion was presented and the feedthrough was shown to be in quadrature and removed with demodulation at the fundamental resonant frequency.

In chapter 3, the state space model for the closed loop electronics was developed and a small and large oscillation amplitude model was developed. Next, the oscillator loop was linearized using describing functions and the stability criterion was derived. The instability of the oscillator loop was confirmed for a normalized cubic stiffness less than -1.34 N/m^3 compared with a theoretical value of -0.533 N/m^3.

In chapter 4, the simulations of the phase locked loop and oscillator loop were performed and the oscillator loops limit cycle was confirmed. The nonlinear VCO was shown to lock in approximately twice the time needed by the linear VCO. The oscillator loop start-up transient was 0.4 seconds due to the large quality factors (~20e3) associated with the resonator.

In chapter 5, the performance of the PVR was examined using the dynamic model and an error model was constructed. The current prototype design does not meet the desired 0.4 ppm voltage stability due to the changes in the pressure of the sealed resonator. A baseline design was developed that reduces the drive voltage and slightly decreases the quality factor. The baseline

110

design does meet the voltage stability specification. The performance of both of these designs would be improved with a AGC loop to control the probe voltage magnitude.

Finally, in chapter 6, the PLL loop design was completed using a classic control analysis of the linearized loop. The PVR prototype was built and tested at Draper Laboratories. The oscillator loop self-started in agreement with the simulations. The phase locked loop locked properly. The fully functioning prototype confirmed the PVR functionality of the device.

The analytic models developed for the PVR are very accurate in predicting the resonant frequency, output amplitude, electrostatic characteristic, start-up transient, and other device characteristics. The models provide an excellent description for the operation of the PVR. Additionally testing of the PVR is required to determine the long term stability under temperature control, amplitude variations, and pressure variations.

Along with these tests, there are several improvements that can be made to the design. First, the addition of an amplitude control loop would enhance performance of the PVR. Finally, the design of a micromechanical resonator that provides position independent forcing would be an enormous advantage, eliminating the amplitude/frequency coupling. In this device, this effect was minimized by reducing the probe voltage and consequently the amplitude. A parallel plate oscillator is unable to provide this flexibility. Another option for the resonators are the comb drive oscillators in widespread use; however, these are strongly tied to pressure, constraining their performance.

This thesis has demonstrated the feasibility of the micromechanical resonator-based PVR. Initially testing shows the PVR to perform well with a self-starting operation. The analytical models predict that performance can be reduced below 0.4 ppm voltage stability with an AGC loop or reduction in probe voltage.

BIBLIOGRAPHY

[1] Bevington, Philip R. and D. Keith Robinson. *Data Reduction and Error Analysis for the Physical Sciences.* 2nd ed. New York; McGraw-Hill, 1992.

[2] Blom, F.R., S. Bouwstra, M. Elwenspoek, and J.H.J. Fluitman. "Dependence of the Quality Factor of Micromachined Silicon Beam Resonator on Pressure and Geometry." *Journal of Vacuum Science Technology B.* Vol. 10(1). Jan/Feb 1992. pp. 19-26.

[3] Campbell, Jim. Personal communication.

[4] French, A.P. *Vibrations and Waves.* New York; W.W. Norton & Company, 1971.

[5] Gardner Floyd M. *Phaselock Techniques.* 2nd ed. New York; Wiley, 1979.

[6] Gray, Paul R. and Robert G. Meyer. *Analysis and Design of Integrated Circuits.* 3rd ed. New York; Wiley, 1993.

[7] Howe, Roger T. "Applications of Silicon Micromachining and Resonator Fabrication," *Proceeding 1994 IEEE Frequency Control Symposium.* June, 1994.

[8] Kossuth, Jonathan A. "Optimization of a Micromechanical Single Element Oscillator Using Nonlinear Electrostatic Control". Ph.D. Thesis, M.I.T. February 1998.

[9] Marion, Jerry B. and Steven T. Thornton. *Classical Dynamics.* 3rd ed. Fort Worth; Saunders College Publishing, 1988.

[10] Nayfeh, A.H. and Mook, D. T. *Nonlinear Oscillations.* New York; John Wiley & Sons, 1979.

[11] Nguyen, C. and Roger Howe "Design and performance of CMOS Micromechanical Resonator Oscillators." *Proceeding 1994 IEEE Frequency Control Symposium.* June, 1994.

[12] Ogata, K. *Modern Control Engineering.* Prentice Hall, 1970.

[13] Rai-Choudary P. ed. *Microlithography, Mircromachining, and Microfabrication.* Vol. 2. Bellingham; SPIE, 1997.

[14] Weinberg, Marc. "Simulation of a Self Drive Series Oscillator Driven by Amplifier and Resistor Noise." Draper Memo EMD-93-1653. June 7, 1993.

[15] Weinberg, Marc. "Phase Noise in an Oscillating Drive Loop." Draper Memo EMD-96-0418. May 1, 1996.

[16] Weinberg, Marc, Anthony Kourepenis and P. Ward. "Temperature Insensitive Silicon Oscillators and Micromechanical Precision Voltage References." Draper Memo EMD-94-1958. Sep. 12, 1994.

[17] Weinberg, Marc. Personal communication

[18] Weinberg, M, J Bernstein, S. Cho, A. T. King, A. Kourepenis, P. Ward. "Initial Results on Micromachined Comb Drive Gyroscope with EDM2 Electronics." *Proceedings 1994 Joint Service Data Exchange*. November 1994.

APPENDICES

Appendix A. Design Spreadsheet

First Order Calculations
for all SS Y0->YSS & w0->wn

		TFG Baseline Design	Optimal Baseline Design	
*proof mass	m	2.73E-09	3.00E-09	kg
*total plate area	A	1.35E-07	1.60E-07	m^2
torquer plate area	At	1.35E-08	0.000000016	m^2
sense plate area	As	1.215E-07	0.000000144	m^2
*fringing coefficient	alpha	1	1	no units
*permittivity of free space	eps	8.85E-12	8.85E-12	Farads/m
*nominal sense gap	Y0	2.50E-06	2.50E-06	m

Second Order Resonator Char.
Resonant Frequencies

* sense mode freq(#384)	w0	168629.1972	168629.1972	rad/s
operating frequency(SS)	wn	134088.0727	127616.5766	rad/s
	f0	26851.783	26851.783	1/s
	fn	21351.60393	20321.11093	1/s

Damping Calculations

*quality factor (384)	Qs	19190	15000	rad/s/m
damping	by	2.39895E-08	3.37258E-08	kg-m

Electrode Voltages

*torquer bias	Va	15	15	V
*torquer excitation	Vb	1.00E-03	1.00E-04	V
*sense bias	Vc	15	15	V
Area voltage totals	AVT	3.0375E-05	3.6E-05	m-V^2
nominal capacitance(t+s) nom. gap	C0	4.779E-13	5.664E-13	Farads

Sense Axis Performance Parameters

Mechanical Stiffness	kym	77.62975082	85.30741849	kg-m/s^2
Electrical Stiffness	kye	-17.20440001	-20.3904	kg-m/s^2
Electrical Stiffness(SS)	kyess	-28.54541215	-36.44944659	kg-m/s^2
Net Linear Stiffness(SS)	ky	49.08433867	48.8579719	kg-m/s^2
ratio of electrical to mech(SS)	kymkye	-0.367712273	-0.42727171	no units

Solve for Gap using iteration(more accurate)				
Dispacement from bias, both electrodes(SS)		-3.88E+00	-4.40E+00	10e-7 m
polynomial, use goal seek for 0 with C35		2.27314E-05	1.9096E-05	
Dispacement from bias, both electrodes(SS)	yc	-3.88257E-07	-4.40074E-07	m
Solve for Gap from PWards Estimate				
Dispacement from bias, both electrodes(SS)	yc2	-3.55902E-07	-3.92624E-07	m
Nominal sense gap(SS)	Yss	2.11174E-06	2.05993E-06	m
Nominal capacitanc(SS)	C0ss	5.65765E-13	6.87403E-13	Farads
Sense Loop Gains Based On One Mass(SS)				
Q at steady state	Qss	15259.22057	11351.82211	rad/s/m
force/Vb	dFdV	-4.01871E-07	-5.00554E-07	N/V
y/force @ sense resonant	dydF	310.877583	232.3432936	m/N
output voltage/y(two proof masses)	dVoutdy	4018705.105	5005544.084	V/m
amplitude of oscillation(one mass)	dy	-1.24933E-07	-1.163E-08	m
amplitude of output voltage(two masses)	Vout	-0.502067008	-0.058214708	V
ratio of torquer to sense force	ratio	2.22222E-10	2.22222E-12	no units
Snapdown Voltages				
DC value (t&s)	Vsnap	17.34397748	16.70070857	V
DC value (s)	Vsnaps	18.28215751	17.60409254	V
Nonlinear Calculation				
Cubic Spring Term (SS)	ky3e	-1.28022E+13	-1.71798E+13	kg/(m-s)^2
normalized cubic	ky3t	-0.004070917	-4.75604E-05	1/m
frequency shift due to cubic term	dw	-0.001526594	-1.78351E-05	no units
true frequency shift	delw	-204.6980553	-2.276058915	rad/s
amp. stab. given 0.3 ppm ang. freq. stab.		9.79582E-05	0.008410065	no units
ratio of amp stab to desire freq stability		326.5272571	28033.55039	no units
Electrical Components				
*Feedback cap	Cfb	2.00E-12	2.00E-12	Farads
*Feedback res	Rfb	2.00E+08	2.00E+08	Ohms
Frequency Stability given Voltage Stability				
Best Estimates at One Op. Point				
Desired Voltage Stability	thetavov	4.00E-07	4.00E-07	no units
Frequency Stability(Analytical)	thetawowa	2.32623E-07	2.98411E-07	no units
for test case see electrostatic.m				
not valid past 5V				

	TFG Baseline Design	Optimal Baseline Design
m	0.00000000273	0.000000003
A	0.000000135	0.00000016
At	=0.1*A	=0.1*A
As	=0.9*A	=0.9*A
alpha	1	1
eps	0.00000000000885	0.00000000000885
Y0	0.0000025	0.0000025
w0	=26851.783*2*3.14	=26851.783*2*3.14
wn	=w0*SQRT(1+kyess/kym)	=w0*SQRT(1+kyess/kym)
f0	=+C14/2/3.14	=+D14/2/3.14
fn	=+C15/2/3.14	=+D15/3.14/2
Qs	19190	15000
by	=m*w0/Qs	=m*w0/Qs
Va	15	15
Vb	0.001	0.0001
Vc	15	15
AVT	=As*Vc^2+At*(Va^2+Vb^2)	=As*Vc^2+At*(Va^2+Vb^2)
C0	=alpha*eps*A/Y0	=alpha*eps*A/Y0
kym	=m*w0^2	=m*w0^2
kye	=-alpha*eps*AVT/Y0^3	=-alpha*eps*AVT/Y0^3
kyess	=-alpha*eps*AVT/Yss^3	=-alpha*eps*AVT/Yss^3
ky	=kym+kyess	=kym+kyess
kymkye	=kyess/kym	=kyess/kym

	-3.8825691935761	-4.40074039471848
yc	=C37^3+2*Y0/0.0000001*C37^2+Y0^2	=D37^3+2*Y0/0.0000001*D37^2+Y0^2
	=+C37*0.0000001	=+D37*0.0000001
yc2	=-alpha*eps*AVT*Y0/(2*kym*Y0^3-2*a	=-alpha*eps*AVT*Y0/(2*kym*Y0^3-2*a
Yss	=Y0+yc	=Y0+yc
C0ss	=alpha*eps*A/Yss	=alpha*eps*A/Yss
Qss	=Qs*wn/w0	=Qs*wn/w0
dFdV	=-alpha*eps*At*Va/Yss^2	=-alpha*eps*At*Va/Yss^2
dydF	=Qss/ky	=Qss/ky
dVoutdy	=2*alpha*eps*(As*Vc+At*Va)/Yss^2/Cf	=2*alpha*eps*(As*Vc+At*Va)/Yss^2/Cf
dy	=Vb*dFdV*dydF	=Vb*dFdV*dydF
Vout	=dy*dVoutdy	=dy*dVoutdy
ratio	=At/A*Vb^2/2/Va^2	=At/A*Vb^2/2/Va^2
Vsnap	=SQRT(kym*(2/3*Y0)^3/(alpha*eps*A))	=SQRT(kym*(2/3*Y0)^3/(alpha*eps*A))
Vsnaps	=SQRT(kym*(2/3*Y0)^3/(alpha*eps*As	=SQRT(kym*(2/3*Y0)^3/(alpha*eps*As
ky3e	=-alpha*2*eps*AVT/Yss^5	=-alpha*2*eps*AVT/Yss^5
ky3t	=ky3e*dy^2/ky	=ky3e*dy^2/ky
dw	=3/8*ky3e/ky*dy^2	=3/8*ky3e/ky*dy^2
delw	=dw*wn	=dw*wn
	=ABS(0.0000003/(dw*2/(1+dw)^2))	=ABS(0.0000003/(dw*2/(1+dw)^2))
	=+C63/0.0000003	=+D63/0.0000003
Cfb	0.000000000002	0.000000000002
Rfb	200000000	200000000
thetavov	0.0000004	0.0000004
thetawowa	=thetavov*Vc^2/wn^2*eps*A/m/Yss^3	=thetavov*Vc^2/wn^2*eps*A/m/Yss^3

The following files contain the code used to simulate the PLL and oscillation loops. These files were only slightly modified to analyze the effects of specific parameter perturbations.

HLOOPO.M
```
% PVR Analysis Solves the non-linear differential equation associated
% with the oscillation of the parallel plate resonators
clear all
clock

% Define constants for Renormalizations
m=2.73e-9;
epsilon=8.85e-12;
A=1.35e-7;
As=0.9*A;
At=0.1*A;
Y0=2.5e-6;
Va=15;
Vb=1e-3;
Vc=Va;
AVT=At*(Va^2+Vb^2)+As*Vc^2;
alpha=1;
w0=26829*2*pi;
kym=w0^2*m;
Q=19190;
by=m*w0/Q;
% Calculate DC displacement yc
c3=1;
c2=2*Y0;
c1=Y0^2;
c0=alpha*epsilon/2*AVT/kym;
c=[c3 c2 c1 c0];
ydc=roots(c);
yc=max(ydc);
% Approximations for Normalizations
% Time Normalization
kye=-alpha*epsilon*AVT/(Y0+yc)^3;
ky=kym+kye; %Exact first order representation using dc displacement
wn=sqrt(ky/m);
% Length Normalization
Fy=-alpha*epsilon*At*Va*Vb/(Y0+yc)^2;          %This is the periodic force for driving, only one
left after removing dc stuff from equations
```

118

```matlab
y0=abs(Fy/ky/by*m*wn); %Low order estimate(w/ steady state)
yp=y0;
% Alternate Time
ky3e=-2*alpha*epsilon*AVT/(Y0+yc)^5;
ky3et=ky3e*y0^2/ky;
wr=sqrt((kym+kye+3/4*ky3e*yp^2)/m);


% Set the integration time and times that matlab will pass solutions at
% note: it will solve at variable time step depending on tolerance settings
tauf=3000e-4*wn;
taustep=0.5;
numpoints=(tauf/taustep)+1;
tauspan=linspace(0,tauf,floor(numpoints));

%Declare Global Variables(extra monitored elements)
global INDEX VHL;
INDEX = 1;
VHL=-1;

% Perform the ODE45 routine, initial conditions all set to zero
xinitial=[0,0,0,0];
options = odeset('outputfcn','myparamso2');
[tau,x]=ode45('loopo2',tauspan,xinitial,options);

%Plot the time evolution
figure(3)
subplot(1,4,1)
plot(tau/wn,x(:,1)*y0+yc);
title('position');
subplot(1,4,2)
plot(tau/wn,x(:,2)*y0*wn);
title('velocity');
subplot(1,4,3)
plot(tau/wn,x(:,3));
title('x*');
subplot(1,4,4)
plot(tau/wn,x(:,4));
title('Vps');

clock
```

LOOPO.M

```
function xprime=loopo2(tau,x);
% the function loopo(tau,x) returns the state derivatives of the
% equations for oscillation of the pvr

% Declare global variables for calculations
global VHL INDEX;

% Set up constants for defining parameters(these are all constant)
m=2.73e-9;
epsilon=8.85e-12;
A=1.35e-7;
As=0.9*A;
At=0.1*A;
Y0=2.5e-6;
Va=15;
Vb=1e-3;
Vc=Va;
AVT=At*(Va^2+Vb^2)+As*Vc^2;
alpha=1;
w0=26829*2*pi;
kym=w0^2*m;
Q=19190;
by=m*w0/Q;
% Calculate DC displacement yc
c3=1;
c2=2*Y0;
c1=Y0^2;
c0=alpha*epsilon/2*AVT/kym;
c=[c3 c2 c1 c0];
ydc=roots(c);
yc=max(ydc);
% Approximations for Normalizations
% Time Normalization
kye=-alpha*epsilon*AVT/(Y0+yc)^3;
ky=kym+kye; %Exact first order representation using dc displacement
wn=sqrt(ky/m);
% Length Normalization
Fy=-alpha*epsilon*At*Va*Vb/(Y0+yc)^2;        %This is the periodic force for driving, only one
left after removing dc stuff from equations
y0=abs(Fy/ky/by*m*wn); %Low order estimate(w/ steady state)
yp=y0;
% Alternate Time
```

120

```
ky3e=-2*alpha*epsilon*AVT/(Y0+yc)^5;
ky3et=ky3e*y0^2/ky;
%Artificial value insertion for stability test
%ky3et=-0.9;
wr=sqrt((kym+kye+3/4*ky3e*yp^2)/m);


% Electronics Parameters
% Sampling rate, Nyquist
taustep=0.0002; %Estimate since matlab adjusts
fny=1/2/taustep;
% Noise Calculations
phiv=1e-16*wn;    %White noise PSD(single sided in V^2/HZ)
vrmss=sqrt(phiv*fny);
gausdev=randn;
VN(INDEX)=vrmss*gausdev;
% Pre-Amplifier Stage
Cfb=2e-12;
Rfb=200e6;
wfbt=1/wn/Cfb/Rfb;
CN=4e-12;%Stray capacitance
% High Pass Stage
Rhpfb=50;
Rhp=1;
% Phase shifter
wpst=0.01;
% Hard Limiter
delta=0.003;


% Closed loop Drive Frequency(Oscillator only)
Vav=15;
Vcv=15;
Vbv=sign(VHL(INDEX))/1000; %Fixes magnitude
Vt1=Vav+Vbv;
Vs1=Vcv;


% Define State Variables (Start variable parameters here)
% x(1)=proof mass position
% x(2)=proof mass velocity
% x(3)=state variable of pre-amp (x*)
% x(4)=phase shifter voltage


% Oscillator loop begin with the output of the hard limiter
% PLL loop is imaginary and used to calculate the frequency
```

121

```
% Oscillator loop
x1p=x(2);
%x2p=-by/wn/m*x(2)-kym/ky*x(1)-
alpha*epsilon/2/ky/y0*(At*Vt1^2+As*Vs1^2)/(Y0+y0*x(1))^2;
% Use state space respresentation of plate
x2p=-(1+3/4*ky3et*(yp/y0)^2)*x(1)-by/wn/m*x(2)-
alpha*epsilon*At*Vav*Vbv/(Y0+yc)^2/ky/y0;
x3p=-wfbt*(x(3)+VN(INDEX)*CN/Cfb)+y0/Cfb*((VN(INDEX)-Vs1)*(-
alpha)*epsilon*As/(Y0+y0*x(1))^2+(VN(INDEX)-Vt1)*(-
alpha)*epsilon*At/(Y0+y0*x(1))^2)*x(2);
Vpre=-Rhpfb/Rhp*(x(3)+VN(INDEX)*(1+CN/Cfb));
x4p=-Vpre-wpst*x(4);
% Hard Limiter requires memory of previous state
% Performed in output function(After every successful completion
% of ode45 routine)
xprime=[x1p;x2p;x3p;x4p];
```

MYPARAMSO.M

```
function status = myparamso2(tau,x,flag);
% This function is called at the end of each successful
% iteration, calculates the hard limiter voltage
global INDEX VHL;
if nargin < 3 | isempty(flag)        % myparamso(t,y)
    m=2.73e-9;
    epsilon=8.85e-12;
    A=1.35e-7;
    As=0.9*A;
    At=0.1*A;
    Y0=2.5e-6;
    Va=15;
    Vb=1e-3;
    Vc=Va;
    AVT=At*(Va^2+Vb^2)+As*Vc^2;
    alpha=1;
    w0=26829*2*pi;
    kym=w0^2*m;
    Q=19190;
    by=m*w0/Q;
    % Calculate DC displacement yc
    c3=1;
```

```
    c2=2*Y0;
    c1=Y0^2;
    c0=alpha*epsilon/2*AVT/kym;
    c=[c3 c2 c1 c0];
    ydc=roots(c);
    yc=max(ydc);
    % Approximations for Normalizations
    % Time Normalization
    kye=-alpha*epsilon*AVT/(Y0+yc)^3;
    ky=kym+kye; %Exact first order representation using dc displacement
    wn=sqrt(ky/m);
    % Length Normalization
    Fy=-alpha*epsilon*At*Va*Vb/(Y0+yc)^2;       %This is the periodic force for driving, only
one left after removing dc stuff from equations
    y0=abs(Fy/ky/by*m*wn); %Low order estimate(w/ steady state)
    yp=y0;
    % Alternate Time
    ky3e=-2*alpha*epsilon*AVT/(Y0+yc)^5;
    ky3et=ky3e*y0^2/ky;
    wr=sqrt((kym+kye+3/4*ky3e*yp^2)/m);


    % Calculate Vpvr for all time intervals passed during this successful step
    INDEX=INDEX+1;
    % Calculate VHL at the end of the time intervals, used in next interval
        delta=0.003;
    if x(4,length(tau)) > delta
        VHL(INDEX) = 1;
        elseif x(4,length(tau)) < -delta
        VHL(INDEX) = -1;
        else
        VHL(INDEX) = VHL(INDEX-1);
    end

else
 switch(flag)
 case 'init'              % myparamso(tspan,y0,'init')

   tau = tau(1);
   x = x;

 case 'done'             % myparamso([],[],'done')

 end
```

end

status = 0;

HLOOPP.M

```
% PVR Analysis Solves the non-linear differential equations
% associated with the PLL loop of the parallel plate resonators
clear all
clock

% Define constants for Renormalization
m=2.73e-9;
epsilon=8.85e-12;
A=1.35e-7;
As=0.9*A;
At=0.1*A;
Y0=2.5e-6;
Va=5;
Vb=10e-3;
Vc=Va;
AVT=At*(Va^2+Vb^2)+As*Vc^2;
alpha=1;
w0=26829*2*pi;
kym=w0^2*m;
Q=19190;
by=m*w0/Q;
% Approximations
% Time Normalization
kye=-alpha*epsilon*AVT/Y0^3;
ky=kym+kye;
wn=sqrt(ky/m);
% Length Normalizatio
Fy=-alpha*epsilon*At*Va*Vb/Y0^2;
yp=abs(Fy/ky/by*m*wn); %Low order estimate(w/o steady state)
y0=yp;
% Alternate Time
ky3e=-2*alpha*epsilon*AVT/Y0^5;
wr=sqrt((kym+kye+3/4*ky3e*yp^2)/m);

% Set the integration time and time step that matlab will alias
tauf=100e-4*wn;
```

```
taustep=0.02;   %one period of oscillator(wn) = 2pi non-dim seconds
numpoints=tauf/taustep+1;
tauspan=linspace(0,tauf,floor(numpoints));

% Declare extra monitored elements
global K0;
K0=2*pi*(-2.773);
% Perform the ODE45 routine, initial conditions all set to zero
% Define options file for the output function,tolerances, and
% special step sizes
%options                                                             =
odeset('outputfcn','myparamsp','RelTol',1,'AbsTol',1,'MaxStep',taustep,'InitialStep',taustep);
options = odeset('outputfcn','myparamsp');
[tau,x]=ode45('loopp',tauspan,[0 0 0],options);

%Plot the time evolution
figure(1)
subplot(1,4,1)
plot(tau/wn,x(:,1));
title('Internal State');
subplot(1,4,2)
plot(tau/wn,x(:,2));
title('Vpvr');
subplot(1,4,3)
plot(tau/wn,x(:,3));
title('Phase of VCO');
subplot(1,4,4)
plot(tau/wn,K0);
title('K0');

clock
```

LOOPP.M

```
function xprime=loopp(tau,x);
% The function loop(t,x) returns the state derivatives of the
% equations for the phase locked loop of the pvr

% Define global constants to allow calculation of additional variables in ode45
global K0;

% Set up constants for defining temporal and spatial normalizations
```

125

```
% and for use in state space equations
m=2.73e-9;
epsilon=8.85e-12;
A=1.35e-7;
As=0.9*A;
At=0.1*A;
Y0=2.5e-6;
Va=5;
Vb=10e-3;
Vc=Va;
AVT=At*(Va^2+Vb^2)+As*Vc^2;
alpha=1;
w0=26829*2*pi;
kym=w0^2*m;
Q=19190;
by=m*w0/Q;
% Approximations for Normalizations
% Time Normalization
kye=-alpha*epsilon*AVT/Y0^3;
ky=kym+kye;
wn=sqrt(ky/m);
% Length Normalization
Fy=-alpha*epsilon*At*Va*Vb/Y0^2;
yp=abs(Fy/ky/by*m*wn); %Low order estimate(w/o steady state)
y0=yp;
% Alternate Time
ky3e=-2*alpha*epsilon*AVT/Y0^5;
wr=sqrt((ky+3/4*ky3e*yp^2)/m);

% Electronics Parameters
% Phase Detector
% Sinusoidal
V1=1;V2=1;
KD=V1*V2/2;
% Square
Vlim=1;
%KD=Vlim/2/pi;
% VCO , use measured characteristic, K0 needed in loop
%K0(INDEX)=2*pi*(-16.269*Vpvr(length(Vpvr))-2.773); %K0 for linearized small signal model
dvpvr=5;            %Sets the desired PVR voltage
K0f=2*pi*(-16.269*dvpvr-2.773);
% Loop Filter
% Non-dimensional
wc=0.01;
```

```
rtal=sqrt(6);
w2=wc/rtal;
w1=wc*rtal;
kc=-wc*wc*rtal/K0f/KD*wn;
% Dimensional
dw2=wc*wn/rtal;
dw1=wc*wn*rtal;
%dkc=wc^2*wn^2*rtal/KD/K0(INDEX);
% State space equations for the pll loop
apll=[0 0 0;1 -wc*rtal 0; 0 1 0];
bpll=[kc*wc/rtal kc 0]';
cpll=[0 0 1];
dpll=[0];

% Define State Variables (Start variable parameters here)
% x(1)=state variable of loop filter
% x(2)=Vpvr, previous(derivative of VCO phase, aV^2+bV)
% x(3)=phase of VCO to be added to phase due to center frequency

% Calculate the reference phase; Choose the frequency to lock to
% Set voltage desired above
wreft=2*pi*(-16.269*dvpvr^2-2.773*dvpvr+26851.783)/wn;
wreftm=mod(wreft*tau,2*pi);
Vref=cos(wreftm); %/abs(cos(wreftm));
% Model VCO,calculate Voltage at the output of VCO
wcen=2*pi*26851.783/wn;                    %wcen measured
phaseVCO=mod(wcen*tau+x(3),2*pi);
vcoout=sin(phaseVCO);
%if phaseVCO == 0
%   vcoout=1;
%else
%   vcoout=sin(phaseVCO)/abs(sin(phaseVCO));
%end
% Model the phase detector, KD is contained within multiplication
pherr=Vref*vcoout;

dx1=bpll(1,1)*pherr;
dx2=x(1)+apll(2,2)*x(2)+bpll(2,1)*pherr;
dx3=x(2)*K0(length(K0))/wn;
xprime=[dx1;dx2;dx3];
```

MYPARAMSP.M

```matlab
function status = myparamsp(tau,x,flag);
% At each step, this is called and sent the initial and final
% values for that step
global K0;
if nargin < 3 | isempty(flag)      % myparams(t,y)
    % Define constants for Renormalization
    m=2.73e-9;
    epsilon=8.85e-12;
    A=1.35e-7;
    As=0.9*A;
    At=0.1*A;
    Y0=2.5e-6;
    Va=5;
    Vb=10e-3;
    Vc=Va;
    AVT=At*(Va^2+Vb^2)+As*Vc^2;
    alpha=1;
    w0=26829*2*pi;
    kym=w0^2*m;
    Q=19190;
    by=m*w0/Q;
    % Approximations
    % Time Normalization
    kye=-alpha*epsilon*AVT/Y0^3;
    ky=kym+kye;
    wn=sqrt(ky/m);
    % Length Normalizatio
    Fy=-alpha*epsilon*At*Va*Vb/Y0^2;
    yp=abs(Fy/ky/by*m*wn); %Low order estimate(w/o steady state)
    y0=yp;
    % Alternate Time
    ky3e=-2*alpha*epsilon*AVT/Y0^5;
    wr=sqrt((kym+kye+3/4*ky3e*yp^2)/m);
% Calculate K0 at every time step
K0=[K0,2*pi*(-16.269*x(2,:)-2.773)];
% Calculate Vpvr for all time intervals passed during this successful step
%INDEX=INDEX+1;
%Vpvr=[Vpvr,x(2,:)];%*wn/K0(INDEX-1)];    %Constant K0 over the interval

else
  switch(flag)
  case 'init'           % myparams(tspan,y0,'init')
```

128

```
    tau = tau(1);
    x = x;

  case 'done'          % myparams([],[],'done')

  end
end

status = 0;
```

The prototype schematic is presented here. The many switches incorporated into the design allow two important functions. First, they were used to test several different modulators(phase detectors) and other blocks for optimal switching performance. Secondly, they allowed the external supply of signals for open loop testing of the device.

PVR CIRCUIT

DRAWING NO.

REV 12

V_PHASE_DETECTOR

VB_EXCITATION_VOLTAGE

VD_EXCITATION_VOLTAGE

OPEN_LOOP_VOLTAGE

FREQ_REF

P5V

N15V

P15V

OP27